

LEVEL
12
S DTIC
ELECTED
NOV 9 1981
H

ADA107147



IGNITION OF COMPOSITE PROPELLANTS
UNDER RAPID PRESSURE LOADING

SUMMARY REPORT

Sponsored by
Office of Naval Research
Power Program
Arlington, Virginia
Contract No. N00014-79-C-0762

Prepared by
M. Kumar, K. K. Kuo,
A. K. Kulkarni, and J. E. Wills

September 1981

DISTRIBUTION STATEMENT A
Approved for public release;
Distribution Unlimited

THE PENNSYLVANIA STATE UNIVERSITY
College of Engineering
Department of Mechanical Engineering
University Park, Pennsylvania

81 11 06 108

Unclassified

SECURITY CLASSIFICATION OF THIS PAGE (When Data Entered)

REPORT DOCUMENTATION PAGE			READ INSTRUCTIONS BEFORE COMPLETING FORM
1. REPORT NUMBER <i>(6)</i>	2. GOVT ACCESSION NO. <i>AD-A107147</i>	3. RECIPIENT'S CATALOG NUMBER	
4. TITLE (and Subtitle) <i>Ignition of Composite Propellants under Rapid Pressure Loading.</i>	5. DATE OF REPORT & PERIOD COVERED Summary kept August 1, 1980-July 31, 1987	6. PERFORMING ORG. REPORT NUMBER <i>1 Huq 80-31 Jul 87</i>	
7. AUTHOR(s) M. Kumar, K. K. Kuo, A. K. Kulkarni, and J. E. Wills	8. CONTRACT OR GRANT NUMBER <i>(15) N00014-79-C-0762</i>	9. PROGRAM ELEMENT, PROJECT, TASK AREA & WORK UNIT NUMBERS	
9. PERFORMING ORGANIZATION NAME AND ADDRESS Department of Mechanical Engineering The Pennsylvania State University University Park, PA 16802	10. REPORT DATE <i>(11) September 1981</i>	11. NUMBER OF PAGES <i>169</i>	
11. CONTROLLING OFFICE NAME AND ADDRESS Office of Naval Research Power Program Arlington, Va. 22217	12. SECURITY CLASS. (of this report) <i>(12) Unclassified</i>	13. DECLASSIFICATION/DOWNGRADING SCHEDULE	
14. MONITORING AGENCY NAME & ADDRESS (if different from Controlling Office)			
15. DISTRIBUTION STATEMENT (of this Report) Approved for public release; distribution unlimited			
16. DISTRIBUTION STATEMENT (of the abstract entered in Block 20, if different from Report) <i>(10) Mridul /Kumar Kenneth K. /Kuo Anil K. /Kulkarni John E. /Willis</i>			
17. SUPPLEMENTARY NOTES			
18. KEY WORDS (Continue on reverse side if necessary and identify by block number) Ignition, Solid Propellants, Wave Reflection, Ignition Delay, Deflagration-to-Detonation Transition, Propellant Cracks			
19. ABSTRACT (Continue on reverse side if necessary and identify by block number) See next page			

Unclassified

SECURITY CLASSIFICATION OF THIS PAGE(When Data Entered)

ABSTRACT

A comprehensive theoretical model for ignition of composite solid propellants was proposed as a framework for formulating ignition models for different propellants under a wide range of operating conditions.

Detailed chemical kinetics information for the AP/PBAA propellants was incorporated into the proposed theoretical model for ignition of composite solid propellants, enabling a more complete description of source terms in the gas-phase energy and species equations. Solid-phase energy equations were coded and implemented on a computer. Numerical solutions of the solid-phase subprogram were successfully checked against analytic solutions for some limiting cases. Using actual measured heat flux near the propellant surface as an input to the solid-phase equations, predictions for the ignition delay time were made.

Effects of pressurization rate, crack-gap width, and igniter-flame temperature on the ignition of AP-based composite solid propellants located at the tip of an inert crack were studied. The ignition process was observed by using a high-speed camera (~40,000 pictures/s) and a fast-response photodiode system. Heat flux to the propellant surface was measured with a thin-film heat-flux gage.

A bright luminous zone behind the reflected compression wave was observed at high pressurization rates. It is believed that this luminous zone is caused by the combustion of unreacted species or particles from the igniter system. Experimental results indicate that the ignition delay time decreases and the heat flux to the propellant surface increases as the pressurization rate is increased. No distinguishable effect of the crack-gap width on the ignition process was evident. Limited results obtained by using an aluminized propellant as the igniter show that the ignition delay time is somewhat lower for higher flame temperature igniter gases. Theoretical predictions employing the solid-phase equations are in reasonable agreement with experimental data.

The decrease in ignition delay with increasing pressurization is caused by enhanced heat feedback to the propellant surface at higher pressurization rates. This augmentation in heat feedback to the propellant at higher pressurization is a result of a combination of the following mechanisms: heating due to compression-wave reflection at the closed end; heat transfer due to recirculating hot gas near the tip; heat release due to combustion of unreacted igniter species (or particles) near the tip, behind the compression wave; and increase in temperature of the gas adjacent to the propellant surface due to continued pressurization of the crack cavity.

Unclassified

SECURITY CLASSIFICATION OF THIS PAGE(When Data Entered)

**IGNITION OF COMPOSITE PROPELLANTS
UNDER RAPID PRESSURE LOADING**

SUMMARY REPORT

Sponsored by

**Office of Naval Research
Power Program
Arlington, Virginia**

Contract No. N00014-79-C-0762

Prepared by

**Mridul Kumar, Telephone (814) 863-0359
Kenneth K. Kuo, Telephone (814) 865-6741
Anil K. Kulkarni, Telephone (814) 865-7073
John E. Wills, Telephone (814) 863-2699**

**Department of Mechanical Engineering
The Pennsylvania State University
University Park, PA 16802**

**Reproduction in whole or in part is permitted for
any purpose of the United States Government.**

Approved for public release; distribution unlimited.

ACKNOWLEDGEMENTS

This research has been sponsored by the Power Program of the Office of Naval Research, Arlington, Virginia, under the Contract No. N00014-79-C-0762. Dr. Richard S. Miller served as the technical monitor and program manager for this contract. His support of this research investigation is greatly appreciated.

The assistance of Mr. Manfred Hund, visiting research associate from Fraunhofer-Institut für Trieb- und Explosivstoffe, Federal Republic of Germany, in the experimental part of this study is acknowledged. We would also like to thank Mrs. Mary Jane Coleman for typing this report.

Accession For	
NTIS GRA&I	<input checked="" type="checkbox"/>
DTIC TAB	<input type="checkbox"/>
Unannounced	<input type="checkbox"/>
Justification	
By _____	
Distribution/	
Availability Codes	
Dist	Avail and/or Special
A	

TABLE OF CONTENTS

ABSTRACT	ii
ACKNOWLEDGEMENTS	iv
LIST OF FIGURES	vii
LIST OF TABLES	ix
I. INTRODUCTION	1
II. THEORETICAL WORK	3
2.1 Ignition Model for AP/PBAA Propellant	3
2.2 Reaction Kinetics of AP/PBAA Propellants	7
2.3 Numerical Solution of a Simplified Case	8
2.3.1 Numerical Scheme	10
2.3.2 Procedures Used in Checking Numerical Solution	13
2.4 Solution of the Complete Model	13
2.4.1 Coordinate Transformation	13
2.4.2 Modeling of Source Terms	17
III. EXPERIMENTAL WORK	21
3.1 Test Apparatus	21
3.2 Data Acquisition System	27
3.3 Determination of Surface Heat Flux	32
IV. RESULTS AND DISCUSSION	35
V. SUMMARY AND CONCLUSIONS	60
VI. NOMENCLATURE	62
VII. REFERENCES	65
APPENDIX A: Combustion-Structural Interaction in a Viscoelastic Material	68
APPENDIX B: Effect of Propellant Deformation on Ignition and Combustion Processes in Solid Propellant Cracks	92
APPENDIX C: Improved Prediction of Flame Spreading during Convective Burning in Solid Propellant Cracks	128
APPENDIX D: Flame Propagation and Combustion Processes in Solid Propellant Cracks	139

APPENDIX E: A Comprehensive Ignition Model for Composite Solid Propellants	148
APPENDIX F: Investigation of Composite Propellant Ignition under Rapid Pressurization	151

LIST OF FIGURES

Fig. 1 Cross-sectional View of a Statistically Averaged Element Considered in the Model	4
Fig. 2 Finite Difference Grid for Solid Phase	11
Fig. 3 Stencil Diagram for a Node	12
Fig. 4a Analytical and Numerical Temperature Distribution in an Inert Solid with a Constant Heat Flux	14
Fig. 4b Comparison of Analytical and Numerical Surface Temperature-Time History	15
Fig. 5 General Layout of Computation Procedure	19
Fig. 6 Schematic Diagram of Igniter System	22
Fig. 7 Exploded View of Igniter System	25
Fig. 8 Schematic Diagram of Test Section	24
Fig. 9 Exploded View of Test Section	25
Fig. 10 Partially Assembled Test Section in the Chamber	26
Fig. 11 Assembled Test Chamber and Igniter System	28
Fig. 12 Block Diagram of Data Acquisition System	29
Fig. 13 Assembled Test Chamber, Igniter System, Hycam Camera, and Photo-diode System	31
Fig. 14 Properties of Mullite (Adopted from Ref. 19)	34
Fig. 15 Burned Plexiglass Window	37
Fig. 16 Time Correlated Pressure Traces (Test No. DNI 3-42)	38
Fig. 17 Time Correlated Pressure Traces for Extremely High Initial Pressurization Rate (Test No. DNI 3-49)	40
Fig. 18 Time Correlated Pressure, Light Intensity, and Thermocouple Signals (Test No. DNI 3-42)	41
Fig. 19 Streak Photograph of Test at Low Pressurization Rate	42
Fig. 20 Streak Photograph of Test at High Pressurization Rate	43
Fig. 21 Photograph for a Typical Test with Air in the Chamber	45
Fig. 22 Photograph for a Typical Test with Nitrogen Purged Chamber	46

Fig. 23 Photograph for a Typical Test with Additional Powdered Propellant in Igniter Chamber	47
Fig. 24 Measured Temperature Time-Traces from Heat Flux Gage	48
Fig. 25 Deduced Heat Flux-Time Traces	49
Fig. 26 Measured Ignition Delay versus Local Pressurization Rate for Various Gap Widths	51
Fig. 27 Comparison Between Predicted and Measured Ignition Delays	55
Fig. 28 Calculated Radial Variation of Propellant Surface Temperature	56
Fig. 29 Calculated Axial Variation of Oxidizer-Fuel Interface Temperature	57
Fig. 30 Calculated Variations of Propellant Surface Temperature at the Oxidizer Fuel Interface with Time	58

LIST OF TABLES

Table 1 Reaction Steps for AP/PBAA Propellant	7
Table 2 Typical Values of Chemical Kinetic Constants	9
Table 3 Physical Properties and Input Parameters	53

I. INTRODUCTION

This report summarizes progress made during the period August 1, 1980 to July 31, 1981, under the project entitled "Transient Ignition Mechanisms of Confined Solid Propellants under Rapid Pressurization" (Contract No. N00014-79-C-0762).

The overall objective of this investigation is to achieve a better understanding of ignition and flame-spreading processes of a solid propellant under rapidly varying pressure conditions. These fundamental studies are expected to help in the design of solid rocket motors and in the reduction of hazards caused by convective burning and deflagration-to-detonation transition (DDT) processes. The research includes both experimental and theoretical studies of solid propellant ignition. Specific objectives of this project are:

1. To formulate a comprehensive ignition model for composite solid propellants;
2. To observe the detailed ignition phenomenon and to measure the ignition delay and instantaneous heat flux to the propellant sample surface;
3. To study the effect of pressurization rate (dP/dt), igniter gas temperature (T_f), and propellant type on ignition delay; and
4. To predict the ignition delay, using measured values of heat flux to the propellant sample surface, and to compare calculated and measured values.

Prior to formulating the ignition model, an extensive literature survey was conducted. Details of this survey were included in our last annual report,¹ and were also presented at the AIAA 16th Joint Propulsion Conference.² Theoretical and experimental work performed, and major results obtained during this reporting period, appear in Sections II to IV.

The following is a list of papers³⁻⁸ published during the past year under the support of this contract. Copies of these publications are included in the Appendices.

1. "Combustion - Structural Interaction in a Viscoelastic Material," Proceedings of the Symposium on Computational Methods in Nonlinear Structural and Solid Mechanics, Washington, D.C., NASA CP-2147, Oct. 1980, pp. 67-90 (by T. Y. Chang, J. P. Chang, M. Kumar, and K. K. Kuo).
2. "Effect of Propellant Deformation on Ignition and Combustion Processes in Solid Propellant Cracks," Proceedings of the 1980 JANNAF Propulsion Systems Hazards Subcommittee Meeting, Monterey, CA, CPIA Publication 330, Dec. 1980, pp. 203-238 (by M. Kumar and K. K. Kuo).
3. "Improved Prediction of Flame Spreading During Convective Burning in Solid Propellant Cracks," Seventh Symposium (International) on Detonation, Annapolis, MD, Preprint Vol. 1, June 1981, pp. 104-114 (by S. M. Kovacic, M. Kumar, and K. K. Kuo).
4. "Flame Propagation and Combustion Processes in Solid Propellant Cracks," AIAA Journal, Vol. 19, May 1981, pp. 610-618 (by M. Kumar, S. M. Kovacic, and K. K. Kuo).
5. "A Comprehensive Ignition Model for Composite Solid Propellants," to be presented at the 18th JANNAF Combustion Meeting, Pasadena, CA, Oct. 19-23, 1981 (by A. K. Kulkarni, M. Kumar, and K. K. Kuo).
6. "Investigation of Composite Propellant Ignition under Rapid Pressurization," to be presented at the 18th JANNAF Combustion Meeting, Pasadena, CA, Oct. 19-23, 1981 (by J. E. Wills, M. Kumar, A. K. Kulkarni, M. Hund, and K. K. Kuo).

II. THEORETICAL WORK

2.1 Ignition Model for AP/PBAA Propellant

A comprehensive model was formulated in order to study ignition of the composite AP/PBAA propellant under rapid pressurization conditions. The detailed mathematical description of this model was reported in the last annual report.¹ A brief summary of the formulation of the model is given below to facilitate discernment of further developments and solution procedures.

The model describes the ignition process for an AP-based composite propellant. To make the problem mathematically tractable, a typical oxidizer crystal is considered to be embedded in a fuel binder in the configuration shown in Fig. 1. Dimensions of the fuel and oxidizer are determined by statistical averaging of the bulk of composite AP/PBAA propellant. The model considers two-dimensional axisymmetric geometry, includes the effect of sudden pressurization in the surrounding region, and makes no *a priori* assumption concerning the site of ignition. The model allows ignition to occur in any region (gas phase, solid phase, or interface) by considering surface, subsurface, and gas-phase chemical reactions. Governing heat equations for the oxidizer and the fuel binder in the solid phase are

$$\text{Oxidizer: } \rho_{\text{Ox},s} c_{\text{Ox},s} \frac{\partial T}{\partial t} = [k_{\text{Ox},s} \frac{\partial^2 T}{\partial z^2} + k_{\text{Ox},s} \frac{\partial^2 T}{\partial r^2} + \frac{k_{\text{Ox},s}}{r} \frac{\partial T}{\partial r}] + \dot{q}_{\text{Ox},s}''' \quad (1)$$

$$\text{Fuel: } \rho_{\text{F},s} c_{\text{F},s} \frac{\partial T}{\partial t} = [k_{\text{F},s} \frac{\partial^2 T}{\partial z^2} + k_{\text{F},s} \frac{\partial^2 T}{\partial r^2} + \frac{k_{\text{F},s}}{r} \frac{\partial T}{\partial r}] + \dot{q}_{\text{F},s}''' \quad (2)$$

$$\text{where } \dot{q}_{\text{Ox},s}''' = \dot{q}_{\text{Ox,radiation}}''' + \dot{q}_{\text{Ox,photochemical}}''' + \dot{q}_{\text{Ox,pyrolysis}}''' \quad (3)$$

$$\dot{q}_{\text{Ox,radiation}}''' = \tau_{\text{Ox}} G \beta_{\text{Ox}} e^{-\beta_{\text{Ox}} z} = \beta_{\text{Ox}} I_z \quad (4)$$

$$\dot{q}_{\text{Ox, photochemical}}''' = \int_0^\infty \tau_{\text{Ox}} I_z q_{\text{Ox,pc}} \eta_{\text{Ox},\lambda} d\lambda \quad (\text{see Ref. 9}) \quad (5)$$

$$\text{and } \dot{q}_{\text{Ox,pyrolysis}}''' = -z_{\text{Ox,py}} q_{\text{Ox,py}} \exp(-E_{\text{Ox,py}}/R_u T) \quad (\text{see Ref. 9}) \quad (6)$$

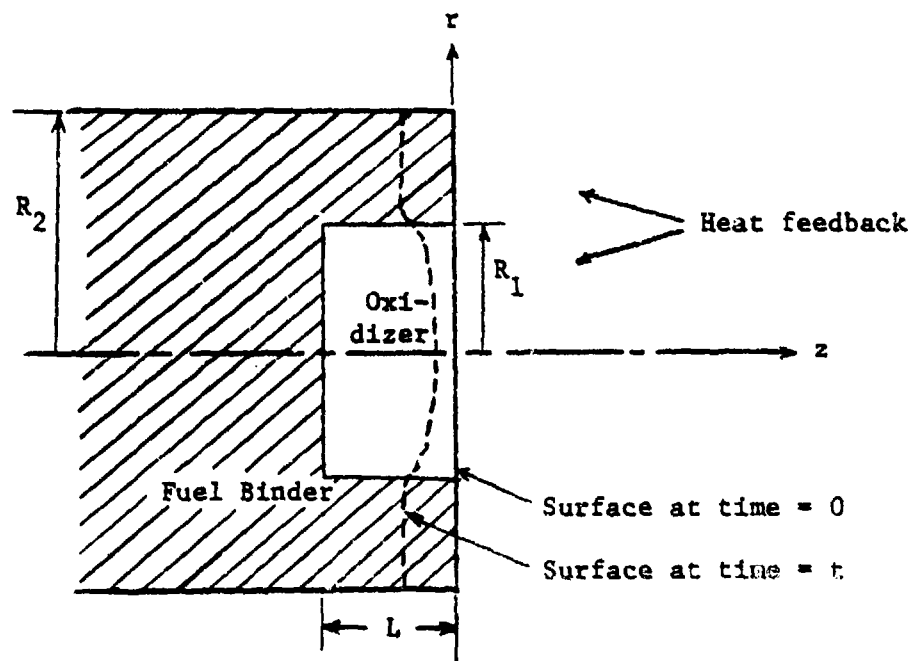


Fig. 1 Cross-sectional View of a Statistically
Averaged Element Considered in the Model

Initial and boundary conditions for the solid phase (fuel and oxidizer) are

$$\text{at } t = 0 : T(0, r, z) = T_i \quad (7)$$

$$\text{on } r = 0 : \frac{\partial T}{\partial r} = 0 \quad (8)$$

$$\text{on } r = R_2 : \frac{\partial T}{\partial r} = 0 \quad (9)$$

at the solid-gas interface, $z = z_{s-g}$:

$$\begin{aligned} k_s \frac{\partial T}{\partial z} \Big|_{z_{s-g}^+} &= k_g \frac{\partial T}{\partial z} \Big|_{z_{s-g}^-} + \alpha_{s-g} G - \epsilon_s E_b s \\ &+ r_b s \rho_s T(c_{p,s} - c_{p,g}) + \dot{q}_{s-g}'' \end{aligned} \quad (10)$$

at $z = -L$:

$$-k_{F,s} \frac{\partial T}{\partial z} \Big|_{-L^-} = -k_{Ox,s} \frac{\partial T}{\partial z} \Big|_{-L^+} + \dot{q}_{Ox-F}'' + \alpha_{Ox-F} T_{Ox} G e^{-\beta_{Ox} L} \quad (11)$$

$$T \Big|_{z = -L^-} = T \Big|_{z = -L^+} \quad (12)$$

at $r = R_1$:

$$-k_{F,s} \frac{\partial T}{\partial r} \Big|_{R_1^+} = -k_{Ox,s} \frac{\partial T}{\partial r} \Big|_{R_1^-} + \dot{q}_{Ox-F}'' \quad (13)$$

$$T \Big|_{r = R_1^+} = T \Big|_{r = R_1^-} \quad (14)$$

$$\text{at } z \rightarrow -\infty : T = T_i \quad (15)$$

Governing equations for the gas phase are

Continuity Eq:

$$\frac{\partial \rho_g}{\partial t} + \frac{\partial (\rho_g v_z)}{\partial z} = 0 \quad (16)$$

Energy Eq:

$$c_p \rho_g \frac{\partial T}{\partial t} + \rho_g c_p v_z \frac{\partial T}{\partial z} - \frac{\partial P}{\partial t} = \frac{1}{r} \frac{\partial}{\partial r} (k_g r \frac{\partial T}{\partial r}) + \frac{\partial}{\partial z} (k_g \frac{\partial T}{\partial z}) + \dot{q}_g''' \quad (17)$$

Species Eq:

$$\rho_g \frac{\partial Y_j}{\partial t} + \rho_g v_z \frac{\partial Y_j}{\partial z} = \frac{1}{r} \frac{\partial}{\partial r} (r D \rho_g \frac{\partial Y_j}{\partial r}) + \dot{\omega}_j''' \quad (18)$$

where $j = 1, 2, 3, \text{ or } 4$ (for the gas phase species: Oxidizer, NH_3 , HClO_4 , and Fuel)

Equation of State:

$$\rho_g = \rho_g(P, T) \quad (19)$$

The momentum equation is replaced by a measured pressure-time trace near the propellant surface.

Initial and boundary conditions for the gas phase are

$$\text{at } t = 0 : v_z = v_{z,i} \quad (20)$$

$$\text{at } t = 0 : T(0, r, z) = T_{g,i} \quad (21)$$

$$\text{at } t = 0 : Y_j = Y_{j,i} \quad (22)$$

$$\text{on } r = 0 : \frac{\partial T}{\partial r} = 0 \quad (23)$$

$$\text{on } r = 0 : \frac{\partial Y_j}{\partial r} = 0 \quad (24)$$

$$\text{on } r = R_2 : \frac{\partial T}{\partial r} = 0 \quad (25)$$

$$\text{on } r = R_2 : \frac{\partial Y_j}{\partial r} = 0 \quad (26)$$

$$\text{on } z = z_{s-g} : \rho_g v_z = \rho_s r_{b_s} \quad (27)$$

$$\text{on } z = z_{s-g} : T|_{z_{s-g}^+} = T|_{z_{s-g}^-} \quad (28)$$

$$\text{on } z = z_{s-g} : \rho_g v_z Y_j|_{z_{s-g}^-} = \rho_g v_z Y_j|_{z_{s-g}^+} - \rho_g D \frac{\partial Y_j}{\partial z} - \dot{\omega}_j'' \quad (29)$$

$$\text{on } z \rightarrow \infty : T = T_\infty(t) \quad (30)$$

2.2 Reaction Kinetics of AP/PBAA Propellants

Five chemical reactions are considered for this family of propellants, viz., exothermic degradation of solid AP particle into oxidizer gases; dissociative sublimation of AP into NH₃ and HClO₄; reaction between premixed NH₃ and HClO₄ gases; fuel pyrolysis; and diffusion flame resulting from chemical reaction between oxidizer and fuel gases to form products. Detailed reaction steps for the AP/PBAA propellants are given in Table 1. The sixth reaction shown at the bottom of Table 1 represents the heterogeneous reaction between the fuel vapor and solid oxidizer. However, this reaction is not considered in the current model because no data is presently available.

Table 1 Reaction Steps for AP/PBAA Propellant

Chemical Reactions Considered in Mathematical Model		Reaction Appears in
1.	AP _(s) $\xrightarrow[k_1]{\text{Exothermic}} \text{Ox(g)}$ Degradation	B.C.
2.	AP _(s) $\xrightarrow[k_2]{\text{Dissociative}} \text{NH}_3\text{(g)} + \text{HClO}_4\text{(g)}$ Sublimation	B.C.
3.	NH ₃ _(g) + HClO ₄ _(g) $\xrightarrow[k_3]{\text{Premixed}} \text{Ox(g)}$ A/PA Reaction	Gas Phase Eq.
4.	PBAA _(s) $\xrightarrow[k_4]{\text{Pyrolysis}} \text{Fuel(g)}$	B.C.
5.	Ox _(g) + Fuel _(g) $\xrightarrow[k_5]{\text{Diffusion}} \text{Products(g)}$ Flame	Gas Phase Eq.
6.	Fuel _(g) + AP _(s) $\xrightarrow[k_6]{\text{Heterogeneous}} \text{Products}$ Reaction	B.C.

A specific reaction rate k is given by the Arrhenius expression

$$k = Z T^{\frac{m}{n}} e^{-E/RT} \quad (51)$$

Typical values for the above chemical kinetic constants, together with the sources, are presented in Table 2.

2.3 Numerical Solution of a Simplified Case

A simplified case of the generalized model described above was solved initially. Instead of using calculated heat feedback from the gas-phase equations, measured heat flux to the propellant surface was used as an input to the solid-phase heat equation.

There are several advantages in obtaining a partial solution to the generalized model. Since the heat flux is measured at a location adjacent to the propellant surface, it provides realistic values of heat feedback to the propellant surface, even for such a complex physical situation. The simplified model, that considers only solid-phase equations and employs measured heat feedback to the propellant surface, will yield reasonably accurate values of ignition delays. Because solutions to several limiting cases of the solid phase equations are well documented, results obtained from the simplified model will make it simpler to independently check the numerical solution procedure for the solid-phase portion of the complete model. The detailed solution method for the solid-phase governing equations, and comparisons with some analytic results to limiting cases, are given in the following subsections. It should be noted that even though the major advantage of the partial solution is its simplicity, results thus obtained depend upon experimental determination of the heat flux, which is expensive and not always feasible. Therefore, solution of the complete model (both solid- and gas-phase equations) is essential for detailed prediction of the ignition process.

Table 2 Typical Values of Chemical Kinetic Constants

Reaction	Order n	Heat of Reaction ΔH_f (cal/g)	Pre-exponential Constant Z	Activation Energy E (kcal/mol)	Remarks	Reference
1 AP(s) $\xrightarrow{k_1} \text{Ox}(g)$	0	-385			70% of Total AP gasification	Lengelle et al. (1976) ¹⁰
		-260				Waeschke (1969) ¹¹
		-277				Kishore et al. (1975) ¹²
		-325				Manelis et al. (1971) ¹³
2 AP(s) $\xrightarrow{k_2} \text{NH}_3(g) + \text{HClO}_4(g)$	0	+494	$2.267 \times 10^7 \frac{\text{s}}{\text{cm}^2 \cdot \text{s}}$	29	30% of Total AP gasification	Guirao and Williams (1971) ¹⁴
		+480	$3 \times 10^5 \frac{\text{s}}{\text{cm}^2 \cdot \text{s}}$	22		Beckstead et al. (1970) ¹⁵
3 $\text{NH}_3(g) + \text{HClO}_4(g) \xrightarrow{k_3} \text{Ox}(g)$	2	-772	$2.03 \times 10^{11} \frac{\text{cm}^3}{\text{mole} \cdot \text{s} \cdot \text{K}}$	15.47		Guirao and Williams (1971) ¹⁴
	1.8	-810	$1.55 \times 10^{13} \frac{\text{cm}^2.4}{\text{s} \cdot \text{mole}^{1.8}}$	30		Beckstead et al. (1970)* ¹⁵
4 PBAA(s) $\xrightarrow{k_4} \text{Fuel}(g)$	1	+1950	$2 \times 10^7 \text{s}^{-1}$	34		Varney and Strahle (1971) ¹⁶
5 Ox(g) + Fuel(g) $\xrightarrow{k_5} \text{Products}$	2	$\Delta H \times 2 = 1.2 \times 10^{11} \frac{\text{cal}}{\text{cm}^2 \cdot \text{s}}$		18		Kashiwagi et al. (1970) ¹⁷

* Quoted by Boddini and Varma (1979)¹⁸

† (+) for endothermic reaction

(-) for exothermic reaction

2.3.1 Numerical Scheme

A finite difference scheme was used for the numerical solution of solid-phase equations. A schematic of the grid system in r and ξ coordinates is shown in Fig. 2. The following features have been incorporated into the numerical solution procedure for improved accuracy, faster convergence, and reduced computation costs.

- i) Variable mesh size
- ii) Central difference scheme to approximate the spatial derivatives
- iii) Generalized Crank-Nicolson representation of the finite-difference equations
- iv) Quasilinearization of the inhomogeneous or source terms.

A successive overrelaxation iterative scheme was used to solve the resulting set of simultaneous algebraic equations.

Figure 3 shows a stencil diagram for a general node (I, J, K) . As indicated by the arrows, calculation of variables at the new time step, i.e., at $(I, J, K+1)$, is influenced by all nodes surrounding the node $(I, J, K+1)$, as well as those surrounding the node (I, J, K) . Finite difference expressions for various derivatives are given below. Here, θ is the Crank-Nicolson parameter.

$$\frac{\partial T}{\partial t} = \frac{\partial T}{\partial t} \Bigg|_{I,J}^{K+1} = \frac{T_{I,J}^{K+1} - T_{I,J}^K}{\Delta t} \quad (32)$$

$$\frac{\partial^2 T}{\partial \xi^2} = \frac{\partial^2 T}{\partial \xi^2} \Bigg|_{I,J}^{K+1} = \theta \frac{T_{I+1,J}^{K+1} - 2T_{I,J}^{K+1} + T_{I-1,J}^{K+1}}{(\Delta \xi_I)^2} + (1 - \theta) \frac{T_{I+1,J}^K - 2T_{I,J}^K + T_{I-1,J}^K}{(\Delta \xi_I)^2} \quad (33)$$

$$\frac{\partial^2 T}{\partial r^2} = \frac{\partial^2 T}{\partial r^2} \Bigg|_{I,J}^{K+1} = \theta \frac{T_{I,J+1}^{K+1} - 2T_{I,J}^{K+1} + T_{I,J-1}^{K+1}}{(\Delta r_J)^2} + (1 - \theta) \frac{T_{I,J+1}^K - 2T_{I,J}^K + T_{I,J-1}^K}{(\Delta r_J)^2} \quad (34)$$

$$\frac{1}{r} \frac{\partial T}{\partial r} = \frac{1}{r} \frac{\partial T}{\partial r} \Bigg|_{I,J}^{K+1} = \frac{1}{r_J} \left[\theta \frac{T_{I,J+1}^{K+1} - T_{I,J-1}^{K+1}}{2\Delta r_J} + (1 - \theta) \frac{T_{I,J+1}^K - T_{I,J-1}^K}{2\Delta r_J} \right] \quad (35)$$

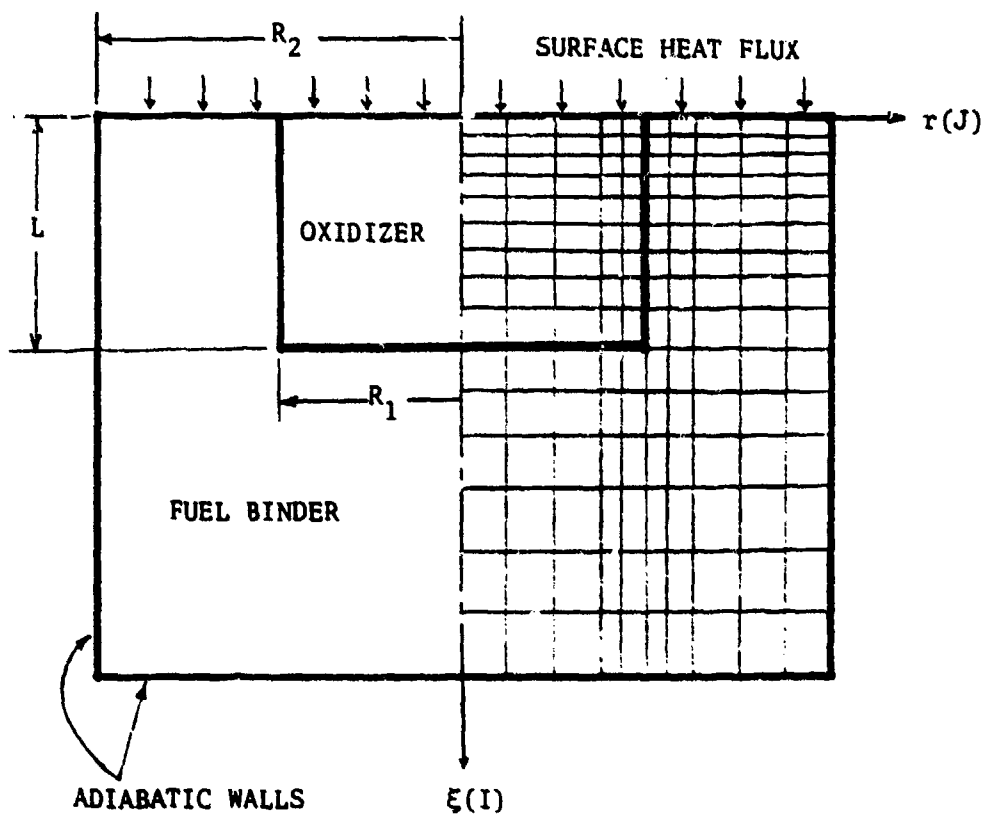


Fig. 2 Finite Difference Grid for Solid Phase

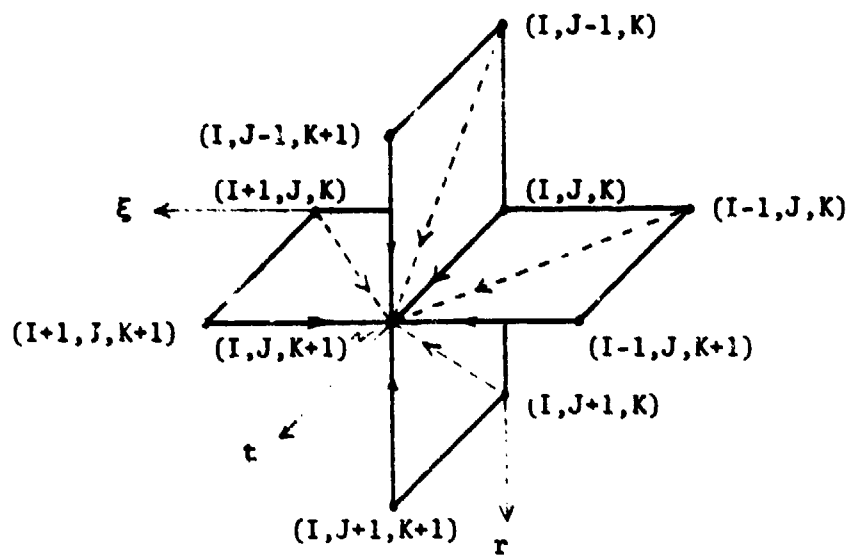


Fig. 3 Stencil Diagram for a Node

2.3.2 Procedures Used in Checking Numerical Solution

Three major checks were made on computed solutions. First, numerical results were compared with the analytic solution for the simple case of a semi-infinite homogeneous solid at uniform initial temperature, with constant external heat flux starting at $t = 0$. Comparison of calculated and analytic distribution of temperature within the solid at various times was excellent (see Fig. 4a). Surface temperature-time history values were also very close (see Fig. 4b). In the second check, a global-energy balance was made. The total energy input from outside at various time steps was within the acceptable error limits of the net increase of internal energy obtained from computed temperature distributions. The third check involved energy balance in elemental volumes around some arbitrarily chosen nodes. The local energy balance also showed excellent agreement.

2.4 Solution of the Complete Model

Governing equations, as outlined in section 2.1, represent a set of transient, second-order, coupled, inhomogeneous, nonlinear partial differential equations. An exact analytic solution of this set of equations is not possible, and approximate solution methods employing asymptotic expansion or similarity do not appear to be very useful. For a complete solution, therefore, the numerical method is used. Several key steps of the solution procedure are briefly described in the following subsections.

2.4.1 Coordinate Transformation

Since the mathematical domain in z -direction is infinite, it was transformed into a finite region using the transformation given below. This transformation also makes possible a finer grid size near the propellant surface in the real spatial coordinate, where large temperature gradients exist, while using a uniform grid in the transformed coordinate. This transformation alleviates the instability

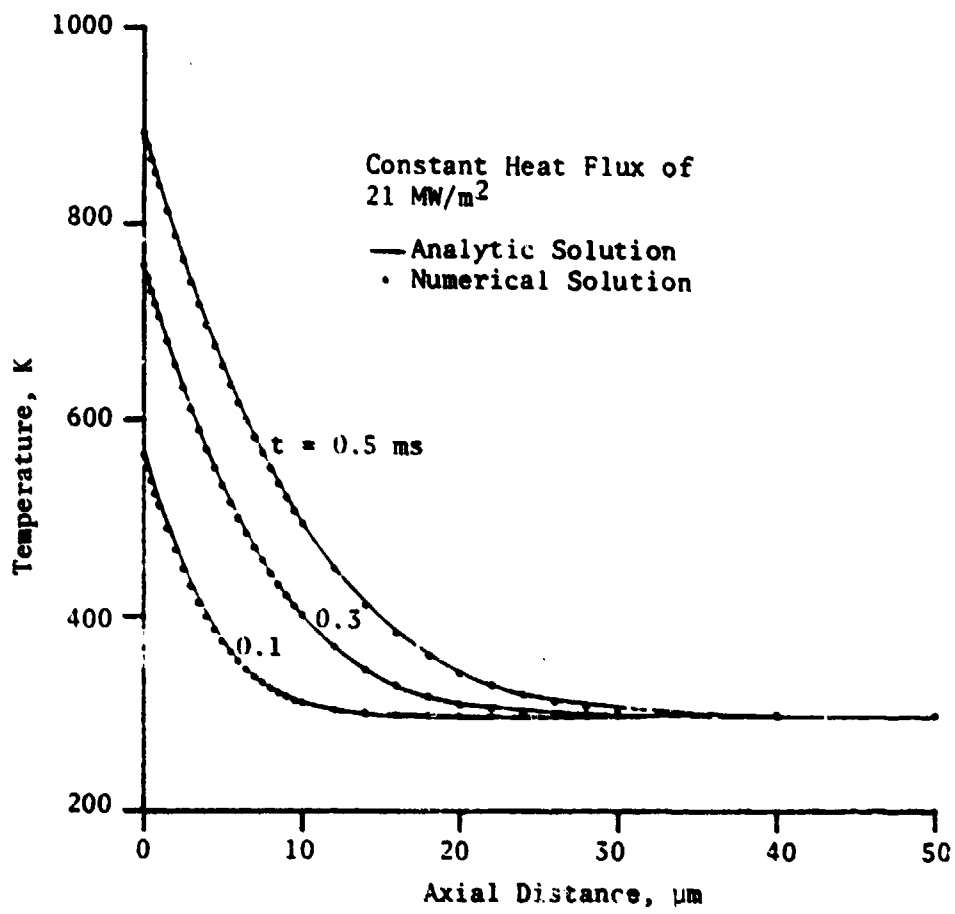


Fig. 4a Analytical and Numerical Temperature Distribution in an Inert Solid with a Constant Heat Flux

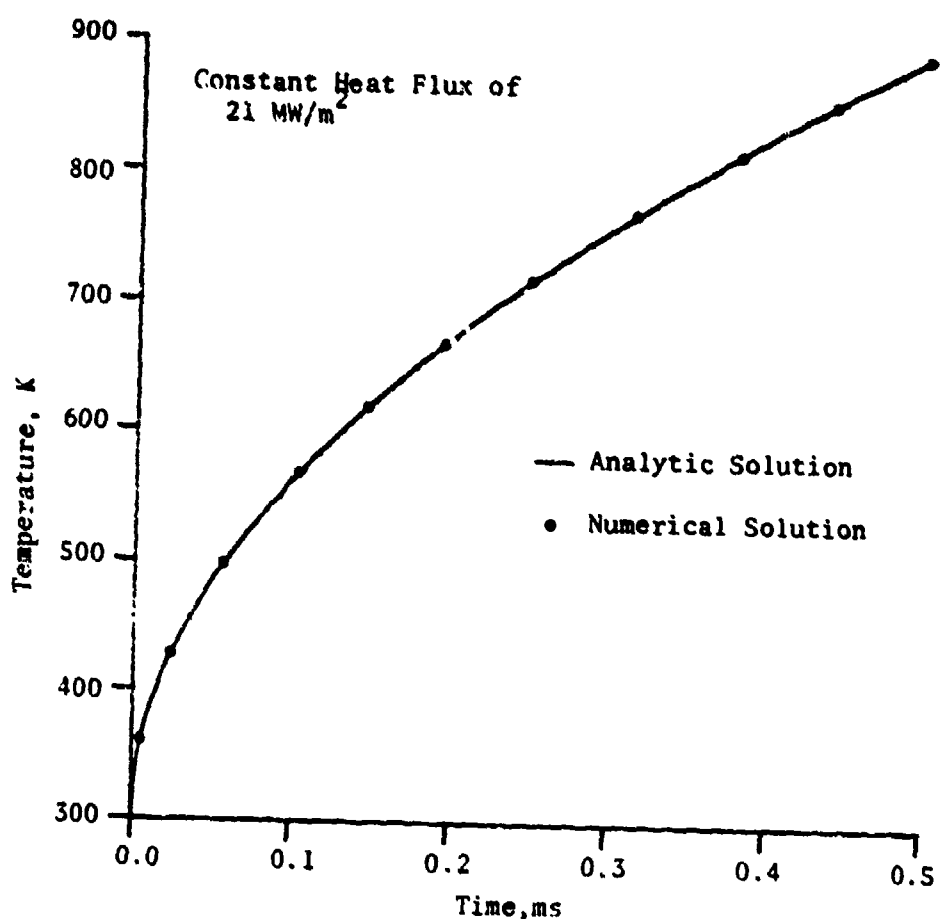


Fig. 4b Comparison of Analytical and Numerical Surface Temperature-Time History

associated with nonuniform grid spacing, which would have been necessary for the z coordinate. The following exponential coordinate transformation is employed in the gas phase.

$$\begin{aligned} s &= 1 - \exp(-Az) \\ \text{or, } z &= -\frac{1}{A} \ln(1-s) \end{aligned} \quad (36)$$

This gives

$$z = \infty \implies s = 1 \quad (37)$$

$$z = 0 \implies s = 0 \quad (38)$$

$$\frac{\partial}{\partial z} = A(1-s) \frac{\partial}{\partial s} \quad (39)$$

$$\frac{\partial^2}{\partial z^2} = A^2(1-s)^2 \frac{\partial^2}{\partial s^2} \quad (40)$$

Note: The r axis remains unchanged.

The transformed, gas-phase, governing equations are:

Continuity Eq.

$$\frac{\partial \rho_g}{\partial t} + A(1-s) \frac{\partial(\rho_g v_z)}{\partial s} = 0 \quad (41)$$

Energy Eq.

$$\begin{aligned} c_p \rho_g \frac{\partial T}{\partial t} + \rho_g c_p v_z A(1-s) \frac{\partial T}{\partial s} - \frac{\partial P}{\partial t} \\ = \frac{1}{r} \frac{\partial}{\partial r} (k_g r \frac{\partial T}{\partial r}) + A(1-s) \frac{\partial}{\partial s} [k_g A(1-s) \frac{\partial T}{\partial s}] + \dot{q}_g'' \quad (42) \end{aligned}$$

Species Eq. ($j = 1, 2, 3, 4$)

$$\rho_g \frac{\partial Y_j}{\partial t} + \rho_g v_z A(1-s) \frac{\partial Y_j}{\partial s} = \frac{1}{r} \frac{\partial}{\partial r} (r D \rho_g \frac{\partial Y_j}{\partial r}) + \dot{\omega}_j''' \quad (43)$$

All boundary conditions remain unchanged except the mass balance of individual species at the interface eq. (29):

$$\text{on } s = s_{s-g}^- : \rho_g v_z Y_j \Big|_{s_{s-g}^-} = \rho_g v_z Y_j \Big|_{s_{s-g}^+} - \rho_g D A(1-s) \frac{\partial Y_j}{\partial s} \Big|_{s_{s-g}^+} - \dot{\omega}_j''' \quad (44)$$

2.4.2 Modeling of Source Terms

In order to solve the governing equations, source terms (\dot{q}_g^m , \dot{q}_j^m , $\dot{\omega}_j^m$, and $\dot{\omega}_j^{mm}$) must be expressed as functions of other variables and known parameters. In modeling the source terms, it is implicitly assumed that the rate-controlling reactions are single-step and irreversible. It is further assumed that the reaction rate constant has Arrhenius dependence on local temperature.

If the gas-phase mass fractions, Y_1 , Y_2 , Y_3 , Y_4 , Y_5 , represent the oxidizer, ammonia, perchloric acid, fuel, and products, respectively, the source terms can be expressed as follows.

$$\begin{aligned}\dot{\omega}_1^{mm} &= Z_3 \frac{W_1}{W_2 W_3} \rho_g^2 Y_2 Y_3 \frac{1}{T} \exp(-E_3/R_u T) \\ &\quad - Z_5 \frac{1}{W_4} \rho_g^2 Y_1 Y_4 \exp(-E_5/R_u T)\end{aligned}\quad (45)$$

$$\dot{\omega}_2^{mm} = -Z_3 \frac{1}{W_3} \rho_g^2 Y_2 Y_3 \frac{1}{T} \exp(-E_3/R_u T) \quad (46)$$

$$\dot{\omega}_3^{mm} = \dot{\omega}_2^{mm} \frac{W_3}{W_2} \quad (47)$$

$$\dot{\omega}_4^{mm} = -Z_5 \frac{1}{W_1} \rho_g^2 Y_1 Y_4 \exp(-E_5/R_u T) \quad (48)$$

$$\dot{q}_g^m = -(\dot{\omega}_2^{mm} \Delta H_3 + \dot{\omega}_4^{mm} \Delta H_5) \quad (49)$$

where ΔH_3 is the heat of reaction per unit mass of ammonia for reaction 3, and ΔH_5 is the heat of reaction per unit mass of fuel for reaction 5. Other source terms are evaluated in a similar fashion. It should be noted that the reaction rate expression for reaction 3 is taken from Guirao and Williams.¹⁴

A quasilinearization technique was used to linearize the inhomogeneous (or source) terms of the governing equations. To illustrate the quasilinearization procedure, $F(T, Y_j)$ represents an inhomogeneous term of the governing equations. Using the Taylor series expansion technique, F at any time $k + \theta$ is evaluated in

the following manner:

$$F^{k+\theta} = F^k + (T^{k+\theta} - T^k) \left. \frac{\partial F}{\partial T} \right|_j^k + (Y_j^{k+\theta} - Y_j^k) \left. \frac{\partial F}{\partial Y_j} \right|_j^k \quad (50)$$

where for any variable U , $U^{k+\theta} = \theta U^{k+1} + (1-\theta) U^k$. The partial derivatives of F are obtained analytically.

It should be noted that for the five species considered in the model, only three species equations have to be solved independently. This is the case since species 2 and 3, i.e., ammonia and perchloric acid, can be shown to have identical governing equation and boundary conditions. Mass fraction of products Y_5 is obtained from the following algebraic relation.

$$Y_5 = 1 - \sum_{j=1}^4 Y_j \quad (51)$$

The finite difference representation of the gas-phase equations is very similar to that of the solid-phase equations. As noted earlier, the coordinate transformation in the gas phase allows one to use uniform grid size in the transformed coordinates, thereby bypassing some of the instabilities associated with nonuniform grid spacing. A general layout of the computation procedure is given in Fig. 5. First, a temperature and species mass-fraction distribution is assumed in the entire region for the new time step. Since the pressure is known, the density is easily computed from equation of state using the assumed temperatures. The continuity equation is then integrated to obtain v_z at each node point. The gas-phase energy equation is then solved using an iterative procedure. Because the species equation for Y_2 is independent of the mass fractions of other species, it is integrated first to obtain the new value of Y_2 . Species equations for Y_1 and Y_4 are then solved iteratively to obtain mass fractions of fuel and oxidizer. Using the new values of mass fractions, the energy equation is solved again to obtain gas-phase temperature, until both temperature and mass fractions converge.

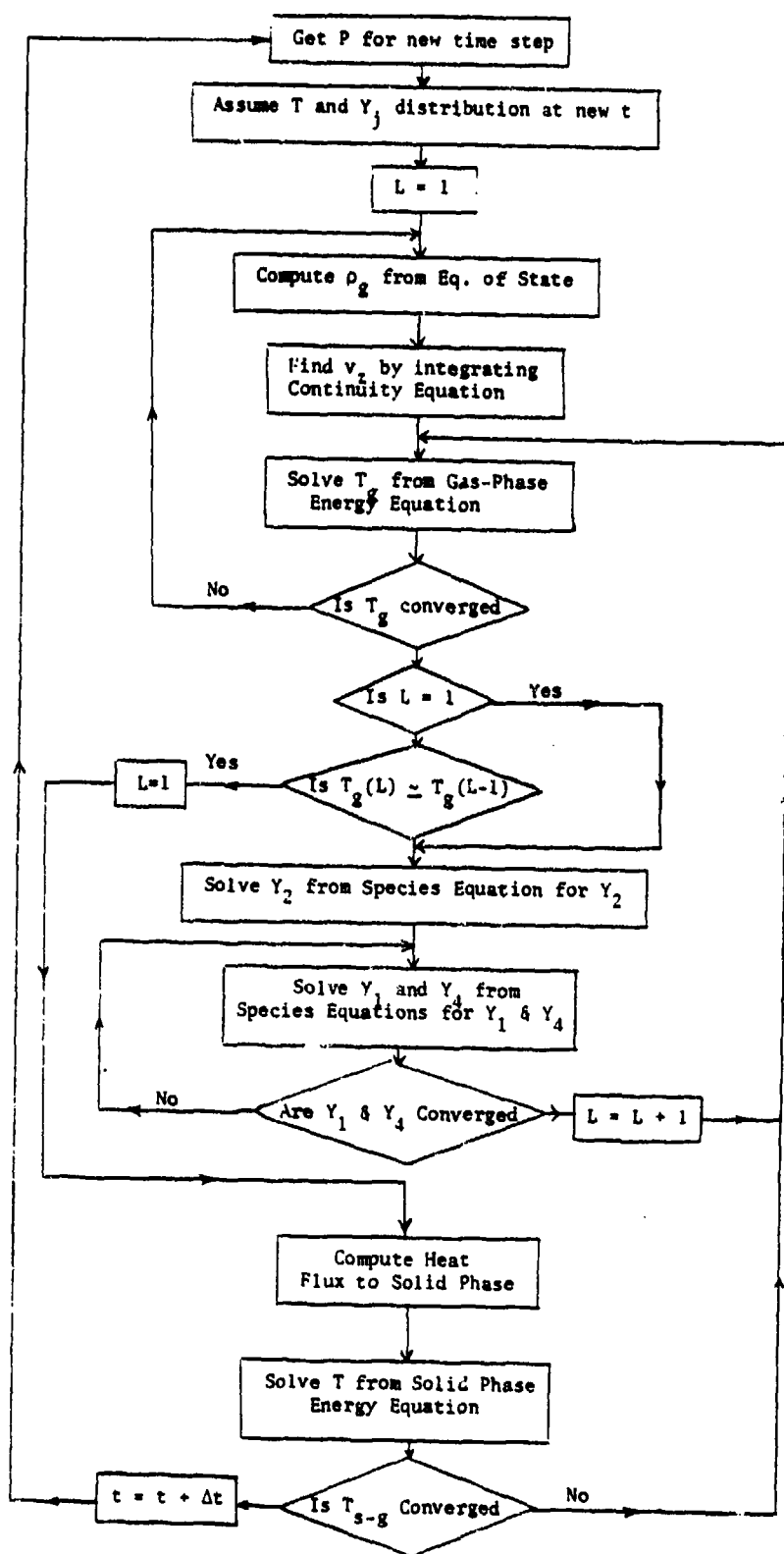


Fig. 5 General Layout of Computation Procedure

From the gas-phase temperature distribution, heat flux to the propellant surface is computed, and the solid-phase heat equations are solved. The solid-gas interface temperatures thus calculated are used as the new boundary conditions to solve the gas-phase equations again. This procedure is repeated until the solid-gas interface temperatures at a given time step converge.

III. EXPERIMENTAL WORK

3.1 Test Apparatus

The test apparatus was designed to obtain high-temperature, high-pressure gases, which closely simulate conditions in an actual rocket motor. Pressurization rates obtained in this setup are close to those encountered before the onset of transition to detonation. A solid-propellant igniter system was used to obtain the hot-gas composition similar to that in actual rocket motors. Using this apparatus, it is possible to obtain pressures up to 50 MPa (~7,000 psi), and pressurization rates in the order of 100 GPa/s ($\sim 10^6$ atm/s).

Figure 6 shows a schematic of the igniter system, consisting of electric primer (FA 874) and its housing unit; booster propellant and booster nozzle; solid propellant igniter charge and igniter chamber; and multiperforated exit nozzle. Exploded view of the igniter chamber is shown in Fig. 7. When voltage is applied to the electric primer, it produces hot gases which flow over the propellant strip and ignite it. The product gases flow through a multiperforated nozzle into the main chamber.

A schematic of the test section is shown in Fig. 8. A crack-like cavity, formed between a transite slab and a plexiglass window, is situated normal to the flow direction of gases in the main chamber. Thickness of the interchangeable metal spacers determines the crack-gap width. In the present study, the gap width was varied between 1.17 mm and 3.18 mm. The length of the cavity is 145 mm. As shown in Fig. 8, propellant test sample is situated at the tip of this cavity. A heat-flux gage is symmetrically placed adjacent to the propellant sample at the tip. Two pressure ports are provided in the crack cavity: one near the test sample, and the other at the crack entrance. Exploded view of the test section is presented in Fig. 9. Figure 10 shows the partially assembled test section in the chamber.

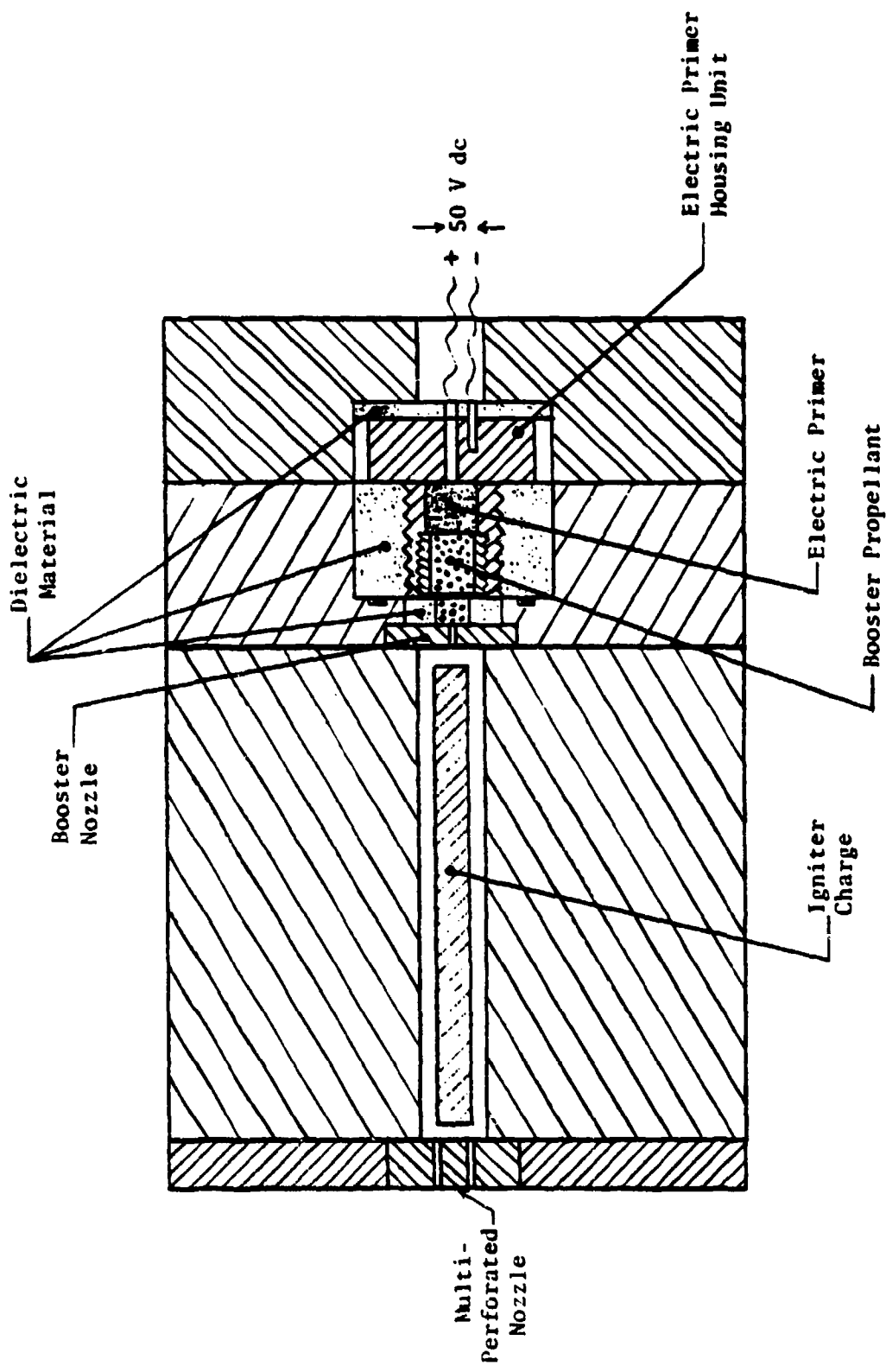
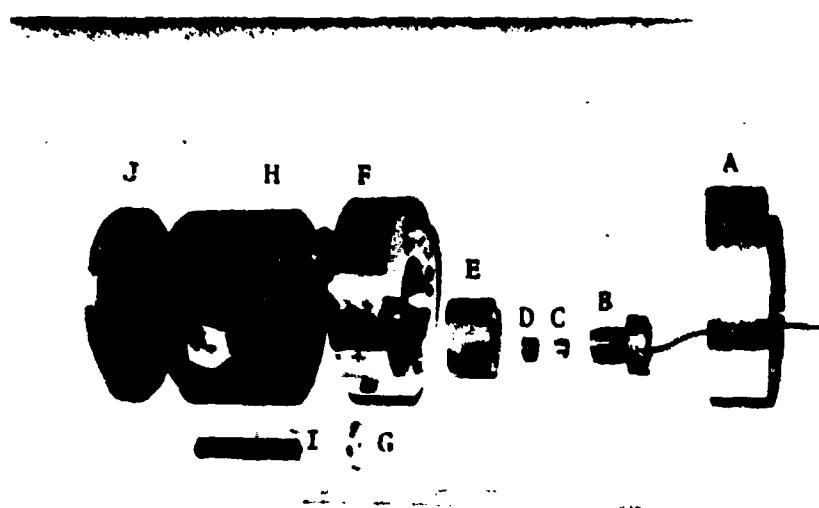


Fig. 6 Schematic Diagram of Igniter System



- | | |
|-----------------------|--------------------------------|
| A Retainer Block | F Booster Chamber |
| B Primer Housing Unit | G Booster Nozzle |
| C Electric Primer | H Igniter Chamber |
| D Primer Retainer | I Igniter Propellant |
| E Dielectric Material | J Multiperforated Nozzle Plate |

Fig. 7 Exploded View of Igniter System

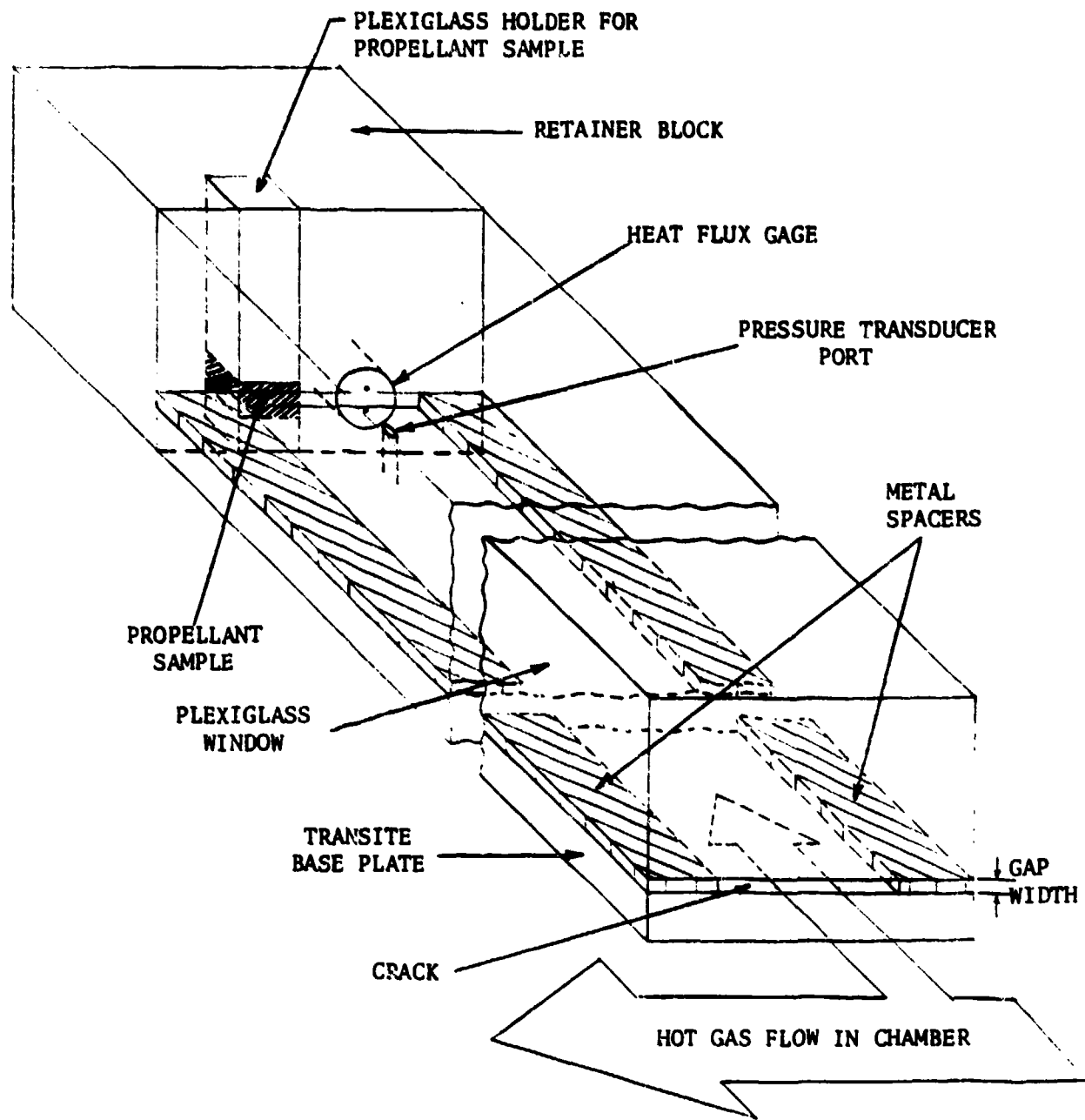
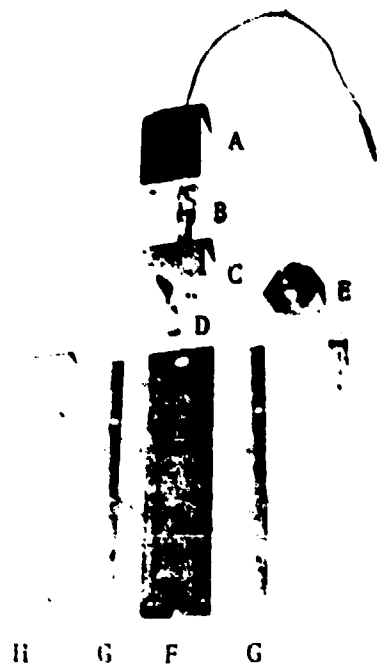


Fig. 8 Schematic Diagram of Test Section



- | | |
|---|------------------------------------|
| A Retainer Block | E Pressure Transducer Housing Unit |
| B Heat Flux Gage | F Transite Plate |
| C Propellant Sample and Heat-Flux
Gage Housing Block | G Metal Spacers |
| D Propellant Sample and its Holder | H Plexiglass Window |

Fig. 9 Exploded View of Test Section

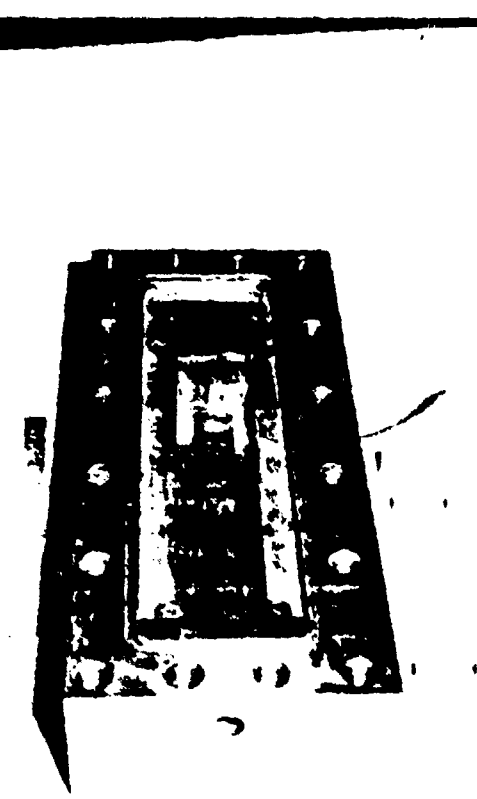


Fig. 10 Partially Assembled Test Section in the Chamber

The ignition event is observed through a set of transparent plexiglass windows. The window assembly is held in place by the window retainer, which forms the top half of the chamber. With the exception of the exit nozzle through which gases are discharged into the atmosphere, the chamber is completely sealed during tests. For safe operation, the chamber is also equipped with a port for the burst diaphragm; the diaphragm ruptures at a pressure of about 70 MPa (~10,000 psi). Figure 11 shows the assembled test chamber, along with the igniter system.

Several parameters can be varied to alter chamber pressurization and igniter-gas temperature. The rate of chamber pressurization is varied by altering any one or more of the following: a) mass of the propellant igniter charge, b) mass of the booster propellant, c) chamber volume, d) insertion of a bursting diaphragm between the igniter chamber and the test chamber, and e) diameters of exit, booster, and multiperforated igniter nozzles. In order to change the igniter gas temperature, igniter propellants with different flame temperatures were used.

3.2 Data Acquisition System

A block diagram of the data acquisition system used in the present study is shown in Fig. 12. This system is comprised of 1) pressure measuring system, 2) heat-flux measuring system, 3) photodiode setup, 4) high-speed photography system, and 5) transient wave-form recording system. The ignition event was remotely controlled, using a relay circuit connected to the footage-controlled event switch on the camera.

Pressure measurements were made at three locations in the chamber: one each near the propellant sample, at the entrance of the crack cavity, and in the main chamber. Piezoelectric quartz transducers with a rise time of 1.5 μ s and natural frequency of 300 kHz were used to measure the pressure. Signals from the transducers were amplified through a charge amplifier before recording. Heat-flux measurements were made with thin-film heat-flux gages. The heat-flux gage is

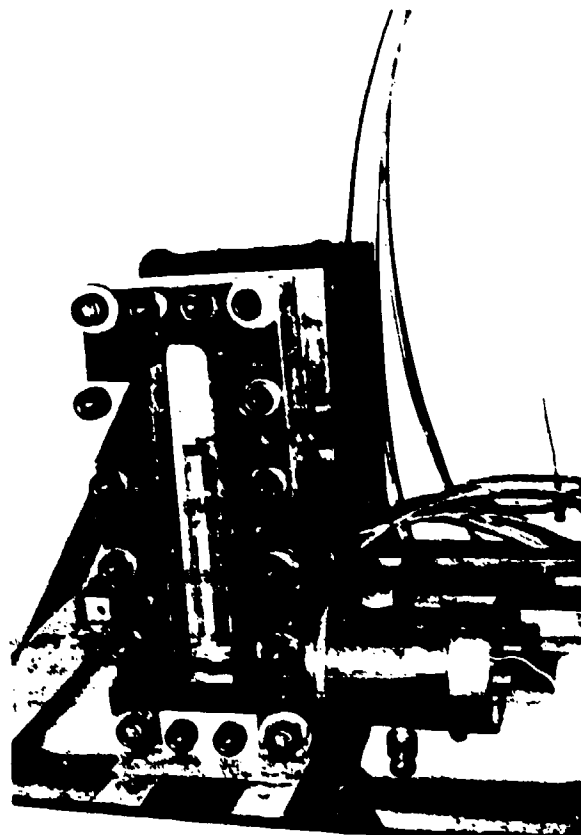


Fig. 11 Assembled Test Chamber and Igniter System

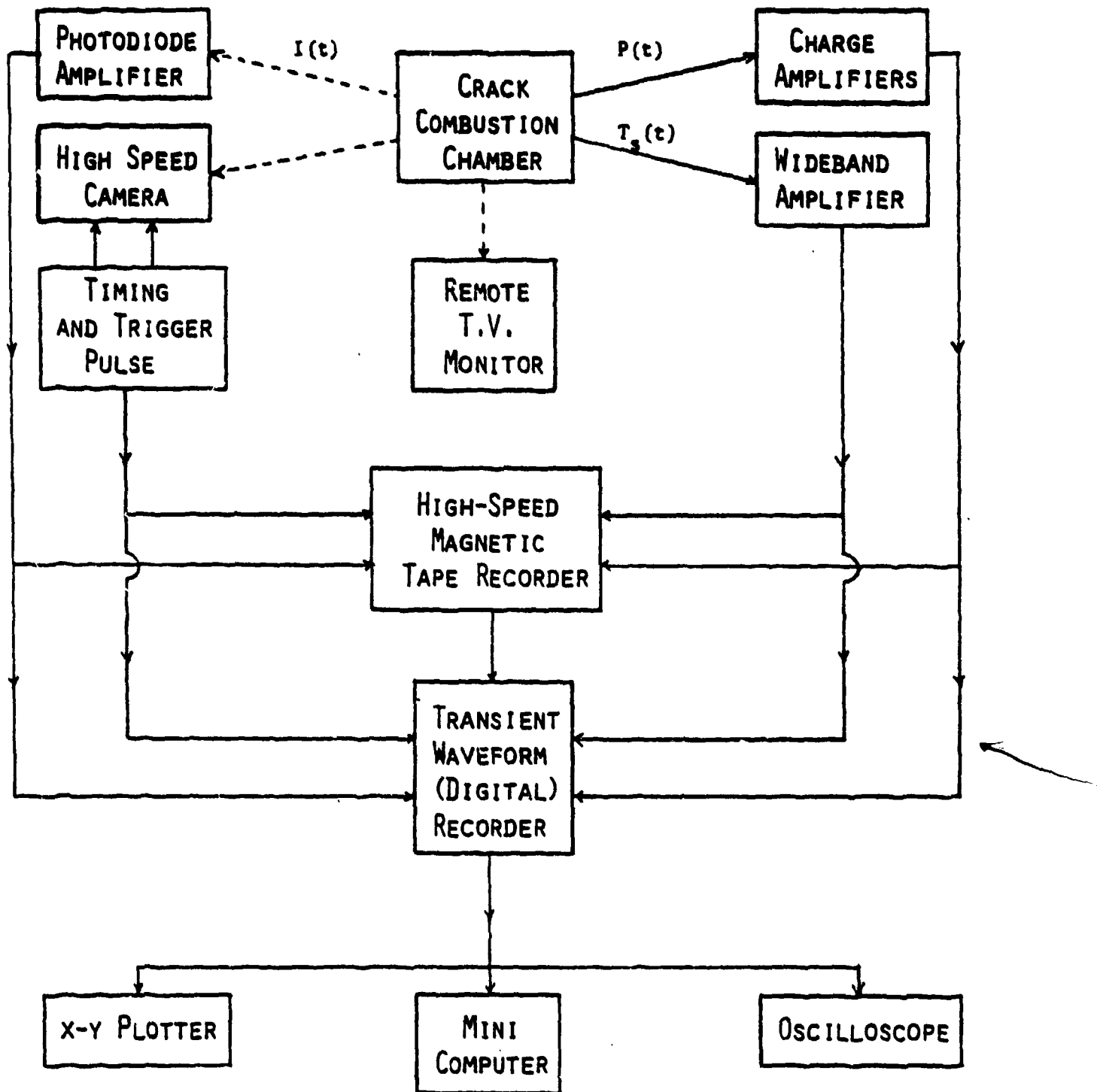


Fig. 12 Block Diagram of Data Acquisition System

essentially a thermocouple in which 0.5-1.0 μm thick films of thermoelements are deposited on a ceramic base (mullite). The response time of these thin-film thermocouples is in microseconds.¹⁹ In the present study, platinum and rhodium were used as thermoelements. Output of the thermocouple is amplified by a wide-band amplifier. The procedure for obtaining the heat flux from temperature measurements is outlined in a later subsection.

The photodiode and high-speed camera systems were used simultaneously to monitor the ignition event. A 16-mm Hycam movie camera recorded the complete ignition event in the chamber. With a quarter-frame optical head, the camera was capable of filming at about 40,000 pictures/s. The photodiode system consists of a photography lens mounted on an optical bed, a fast-response photodiode, and an amplifier. In order to observe ignition of the propellant surface, a small region around the propellant surface is focused onto the photodiode by the lens. Output of the photodiode can be amplified before recording. Use of these two independent systems for the observation of the ignition event reduces the possibility of error. Figure 13 shows the assembled test chamber and igniter system, the Hycam camera, and the photodiode system.

All transient signals are recorded on a digital transient wave-form recorder (Physical Data Model 515), as well as on a high-frequency FM tape recorder. The transient wave-form recorder has a sampling rate up to 2×10^6 samples/s, a maximum amplitude resolution of 0.1%, and a 4k word memory per channel. A light-emitting diode (LED) driver unit is used to generate a trigger or common-time pulse, which is simultaneously recorded on the film and on the transient recorders. This common-time pulse is used for time correlation between data on the film and on the transient recording devices. Digitized output of the transient recorder can be displayed on an oscilloscope or an x-y plotter, or can be transferred to the minicomputer (PDP 11/23) for data storage and processing.



Fig. 13 Assembled Test Chamber, Igniter System,
Hycam Camera, and Photo-diode System

3.3 Determination of Surface Heat Flux

The procedure for determining heat flux from the thin-film-gage temperature data is similar to that outlined by Vidal et al.^{20,21} Since the thickness of the thermoelements is less than $1 \mu\text{m}$, temperature measured by the thermocouple is assumed to be the surface temperature of the insulating ceramic base. Because the duration of the event is in the order of 1 ms, the ceramic base is treated as a semi-infinite solid for heat-flux computations. The expression for heat flux for a semi-infinite solid with known surface temperature-time history²² is

$$\dot{q}''(t) = \sqrt{\frac{k\rho c}{\pi}} \left[\frac{T(t)}{\sqrt{t}} + \frac{1}{2} \int_0^t \frac{T(t) - T(\tau)}{(t-\tau)^{3/2}} d\tau \right] \quad (52)$$

where $T(t)$ is the measured surface temperature.

The integral appearing in Eq. (52) must be evaluated numerically. A simple trapezoidal rule or Simpson's rule techniques do not provide accurate answers, since the integrand becomes infinite at the upper limit. A method proposed by Cook and Felderman²³ was employed to alleviate this problem. $T(\tau)$ is approximated by a piecewise linear function. The final expression for heat flux is given by

$$\begin{aligned} \dot{q}''(t_n) = & \sqrt{\frac{k\rho c}{\pi}} \left[\frac{T(t_n)}{t_n^{1/2}} + \sum_{i=1}^{n-1} \left\{ \frac{T(t_n) - T(t_i)}{(t_n - t_i)^{1/2}} - \frac{T(t_n) - T(t_{i-1})}{(t_n - t_{i-1})^{1/2}} \right. \right. \\ & \left. \left. + 2 \frac{T(t_i) - T(t_{i-1})}{(t_n - t_i)^{1/2} + (t_n - t_{i-1})^{1/2}} \right\} + \frac{T(t_n) - T(t_{n-1})}{(\Delta t)^{1/2}} \right] \quad (53) \end{aligned}$$

where $\Delta t = t_n/n$.

The steps involved in computing heat flux from voltage-time data is as follows. Voltage-time data is converted into temperature-time data using tabulated temperature-EMF values for platinum-rhodium thermocouples. The temperature-time curve is then smoothed, using a cubic spline fit²⁴ through the data. This smoothed temperature

time information is used in Eq. (53) to compute the surface heat flux as a function of time. Properties of mullite, which are a function of temperature as shown in Fig. 14, are averaged over the temperature range.

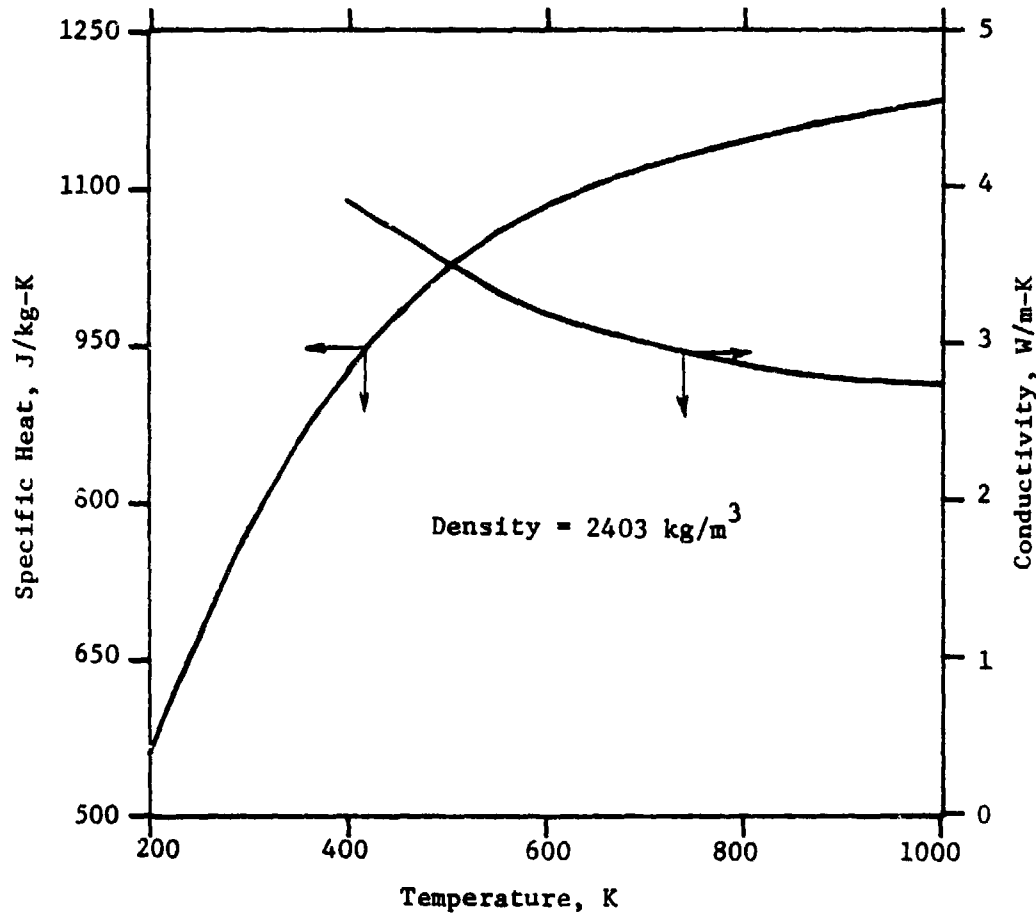


Fig. 14 Properties of Mullite (Adopted from Ref. 19)

IV. RESULTS AND DISCUSSION

The ignition of an AP-based composite solid propellant with PBAA-EPON binder was a subject of this investigation. The weight percent of oxidizer in the propellant was 75%, and the average oxidizer particle size was 76 μm . The flame temperature of this propellant is 1920 K. In most of the experiments, the same propellant was also used as the igniter. In all tests, initial pressure in the chamber was 0.1 MPa and initial temperature was about 298 K.

The sequence of events that occur during the test can be described generally as follows. Hot, combustion product gases from the igniter flow into the main chamber and pressurize it. The pressure gradient causes a part of the gases to penetrate the crack-like cavity. Hot gases and the pressure front propagate along the crack, reach the tip, and are reflected from the closed end. As the process continues, additional hot gases are driven into the crack because of the continually rising chamber pressure. As the hot gases reach the propellant surface, energy is transferred from hot gases to propellant. Heat feedback from the gases can be extremely high because of compression wave reflection from the tip; flow recirculation near the closed end; heat release from the unreacted igniter species (or particles) behind the reflected compression wave; and increased enthalpy of the hot gases because of continued pressurization of the cavity. This heating eventually causes the propellant to ignite.

In the experimental portion of this study, ignition is defined as the onset of emission of luminous light from the propellant surface. A go/no-go type of ignition criterion cannot be applied to the test configuration of this study since it was impossible to remove the energy stimulus following onset of ignition. Although the criterion of onset of luminous light is usually associated with onset of surface ablation, especially for nitramine propellants where considerable time lag exists between surface ablation and ignition, the ignition criterion employed in

this study is quite suitable for AP-based composite propellants, and it has been widely used in the past. In all but one of approximately sixty tests conducted in this study, the propellant sample burned completely. Figure 15 is a photograph taken following testing of the burned plexiglass window next to the propellant sample.

As mentioned in the previous section, pressure measurements were made at two locations in the cavity, one near the propellant sample at the tip and another near the crack entrance. Heat flux from the gases to the propellant was deduced from a heat-flux gage situated adjacent to the test sample. The ignition event was simultaneously recorded on film and a photodiode focused on the propellant surface. High-speed photography was conducted by using either a streak attachment or a quarter-frame optical head. Maximum filming speed during the tests was about 40,000 pictures/s. It was noted that light intensity obtained through streak recording near the tip was a replica of the photodiode signal. Therefore, in order to achieve a more complete understanding of the ignition event, the quarter-frame head was used in most of the tests. Even though the time interval between each picture is about 25-30 μ s, ignition delay can be accurately determined by first locating the ignition event on the film and then obtaining its more precise location from the photodiode signal.

A typical set of time-correlated pressure traces at the crack entrance and at the tip is presented in Fig. 16. The curves shown pertain only to the uprising part of the P-t trace because that is the region of interest. Figure 16 shows that the first discernible pressure rise at the tip occurs some time later than the corresponding pressure rise at the entrance, due to the finite time required by the pressure front to propagate from crack entrance to tip. Also, except for a short period immediately following arrival of the pressure front at the tip, the average pressurization rate is generally lower near the tip, perhaps as a result of frictional losses in the channel as gases travel to the closed end. The pressurization part of this curve is quite linear. Ignition was observed to occur during the uprising part of P-t traces.

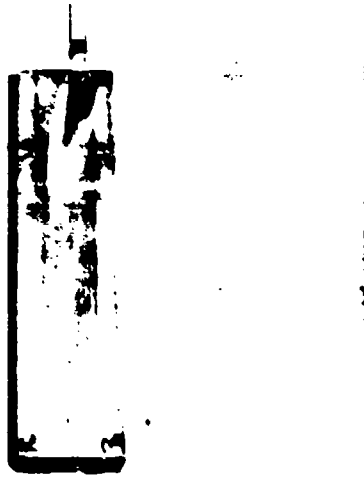


Fig. 15 Burned Plexiglass Window

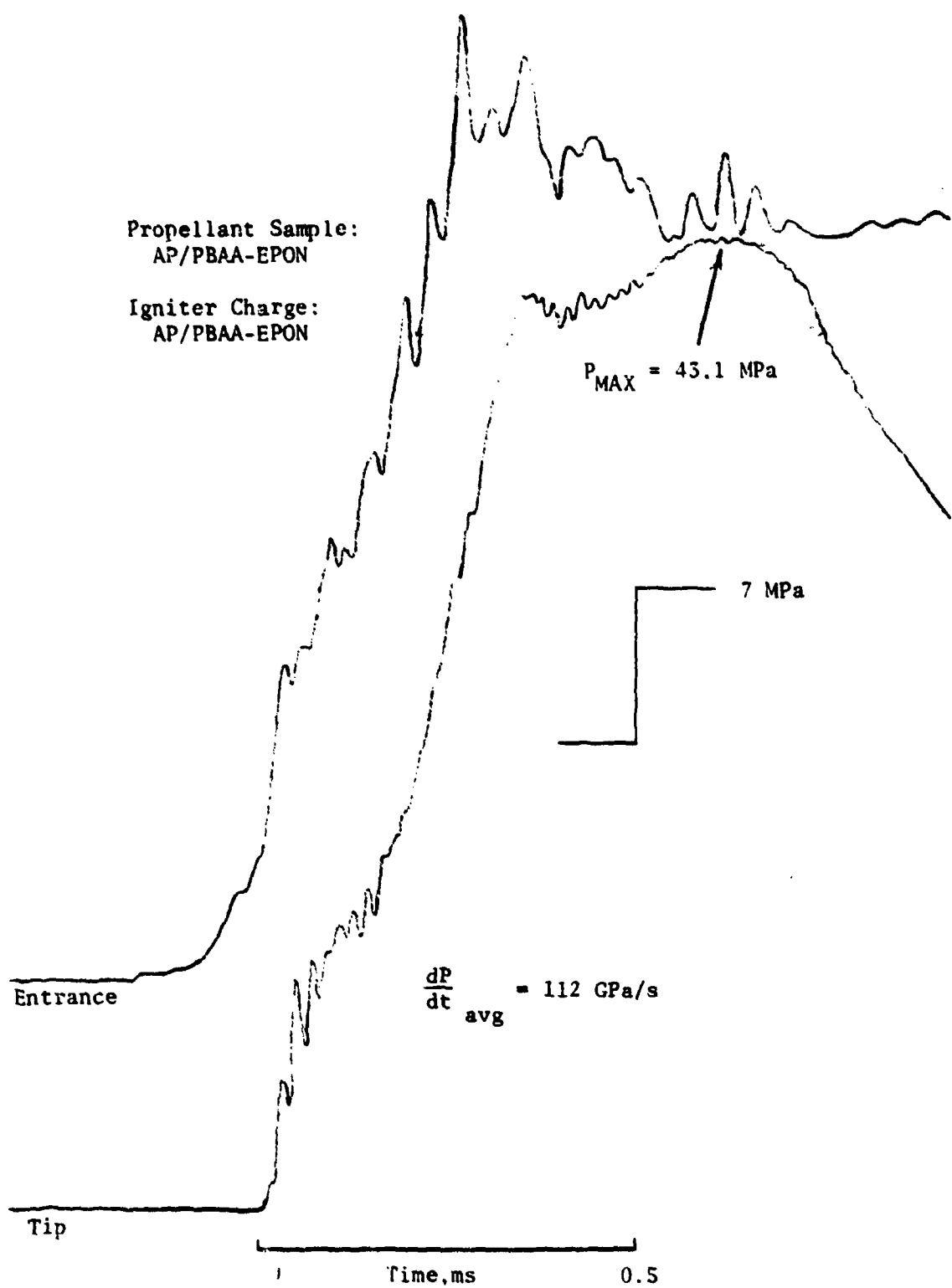


Fig. 16 Time Correlated Pressure Traces
(Test No. DNI 3-42)

Another time-correlated pressure trace, for which the initial pressurization rate was extremely high $(dP/dt)_{init} = 1260 \text{ GPa/s}$, is shown in Fig. 17. From the P-t trace at the tip in Fig. 17, a very steep shock-like compression wave is clearly evident at the instant at which compression waves arrive there.

Typical time-correlated pressure at the tip, light intensity at the propellant surface, and temperature signals from the heat flux gage are shown in Fig. 18. The temperature trace shown is the amplified signal through a wide band amplifier at a gain setting of 50 db. The ignition event is also shown in the figure. As mentioned earlier, the time for ignition is first obtained from the film. A more accurate location of ignition is obtained from the photodiode trace, where a trough followed by an uprising of the curve exists in the neighborhood of the point obtained from the film. In this study, ignition delay is defined as the time lag between arrival of the pressure front at the crack tip and subsequent ignition (i.e., emission of luminous light from the propellant surface).

Figures 19 and 20 show two streak photographs of tests conducted at low pressurization rate (17 GPa/s) and high pressurization rate (55 GPa/s), respectively. One startling difference between the two photographs is evident. At a higher pressurization rate (Fig. 20), immediately after the hot gases reach the crack tip, a luminous region appears there. As time progresses, this luminous region moves downstream toward the crack entrance. Depending upon test conditions, the luminous region may or may not travel all the way to the crack entrance. This bright region may be caused by heat released from combustion behind the reflected compression waves of unreacted species or particles from the igniter system which are carried to the crack tip by strong pressure gradients. At higher pressurization rates, the pressure gradient is steeper, and the igniter species have less time to burn or react completely before entering the combustion chamber. Both of these processes would contribute to the appearance of the bright luminous region at the tip.

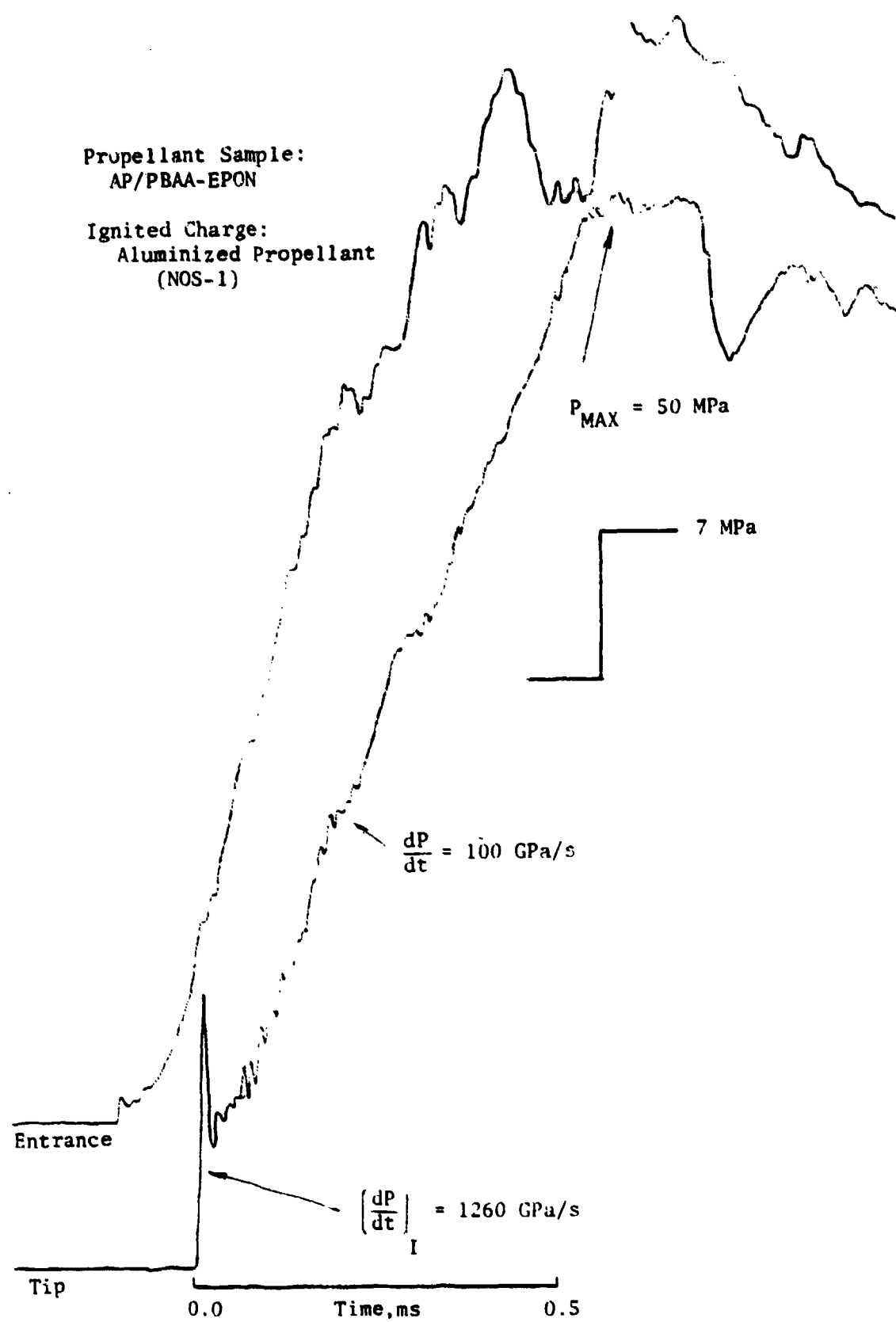


Fig. 17 Time Correlated Pressure Traces for Extremely High Initial Pressurization Rate (Test No DNI 3-49)

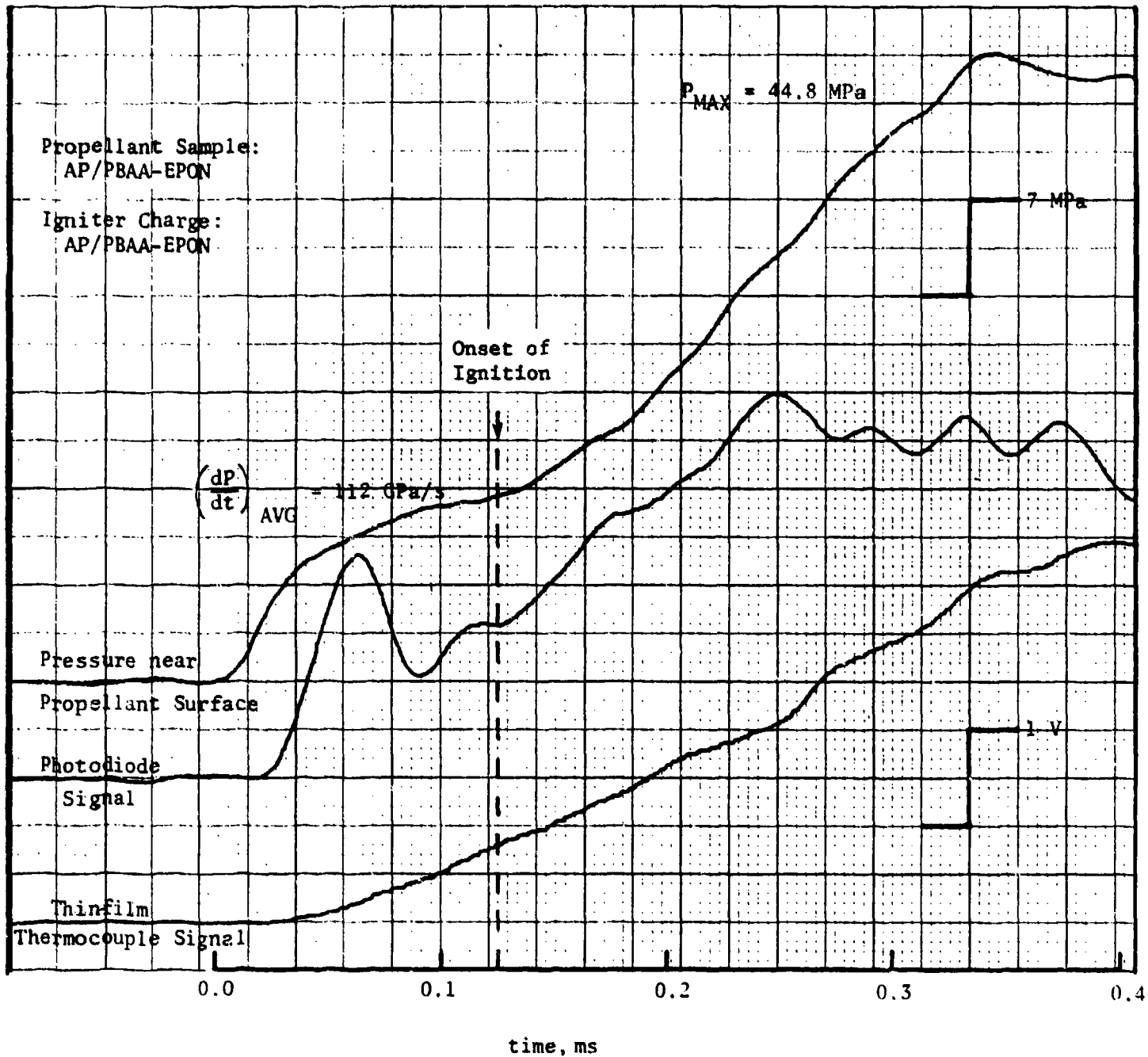


Fig. 18 Time Correlated Pressure, Light Intensity, and Thermocouple Signals
(Test No. DNI 3-42)

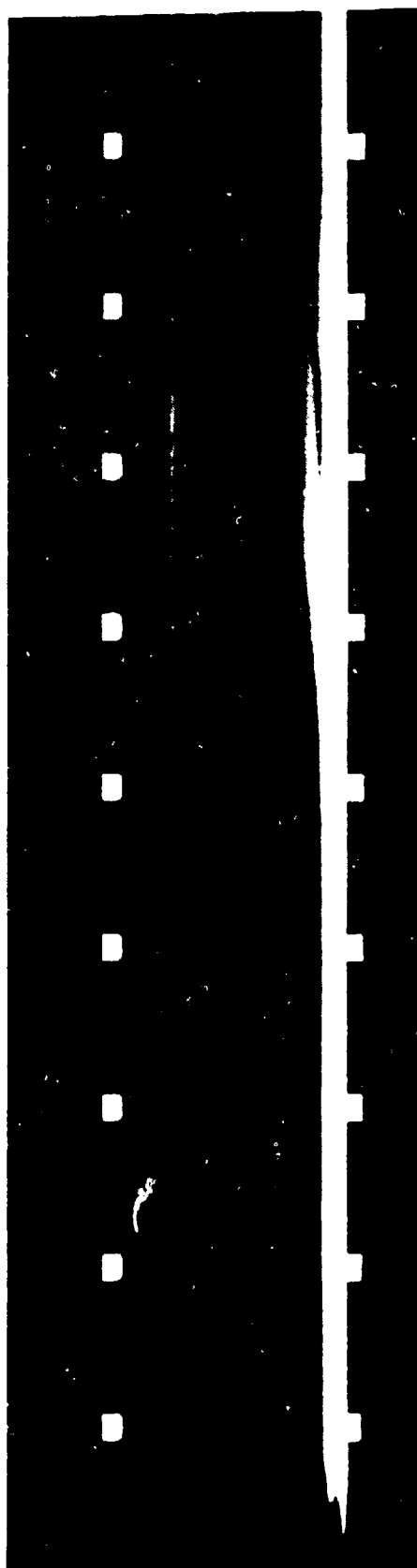


Fig. 19 Strzak Photograph of Test at Low Pressurization Rate

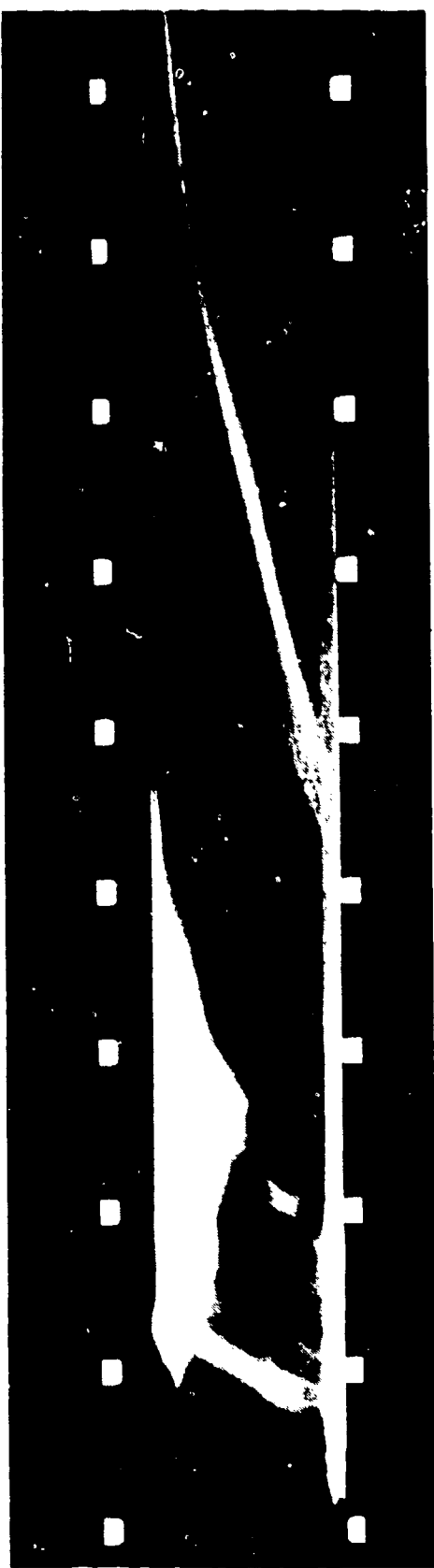


Fig. 20 Streak Photograph of Test at High Pressurization Rate

The observed luminous (reaction) region could also be caused by reaction of igniter species with oxygen present in the chamber. Because of rapid pressurization of the crack cavity, the air present in the cavity could be adiabatically compressed causing a flash reaction between the oxygen in the air and some of the igniter species. To eliminate the possibility that this reaction may have been caused only by the presence of oxygen, tests were also conducted in the chamber purged with nitrogen. Figure 21 shows photographs for a test in which air was present in the chamber, whereas the photograph in Fig. 22 is for a test in which the chamber was purged with nitrogen. It is evident in both cases that the luminous region is present, even though the luminosity is somewhat lower when oxygen is not present. Therefore, oxygen present in the chamber enhances luminosity but is not the only cause of it.

Tests, in which both the igniter grain and a sufficient quantity of powdered propellant were placed in the igniter chamber, were conducted to further investigate the effect of igniter species or particles in causing the luminous zone. Figure 23 presents a set of pictures for this case. The chamber was purged with nitrogen. A comparison of Figs. 22 and 23 shows that the luminosity of this zone is higher for the case shown in Fig. 23. If more particles that can be entrained in the flow are present, the probability that the particles may be carried to the tip with the gas flow and burn there increases. This is especially true at higher pressurization rates because the particles may not have sufficient time to react completely in the igniter chamber or the main chamber.

Figure 24 shows smoothed temperature-time traces measured by using the thin film heat-flux gage for three different pressurization rates. It can be seen from the figure that the rate of increase of surface temperature increases as the pressurization rate is increased. Deduced heat flux as a function of time for the conditions corresponding to Fig. 24 is given in Fig. 25. The shapes of the heat flux-time traces are dictated by their respective temperature-time plots. It should be noted that the heat flux to the propellant surface is extremely high under these

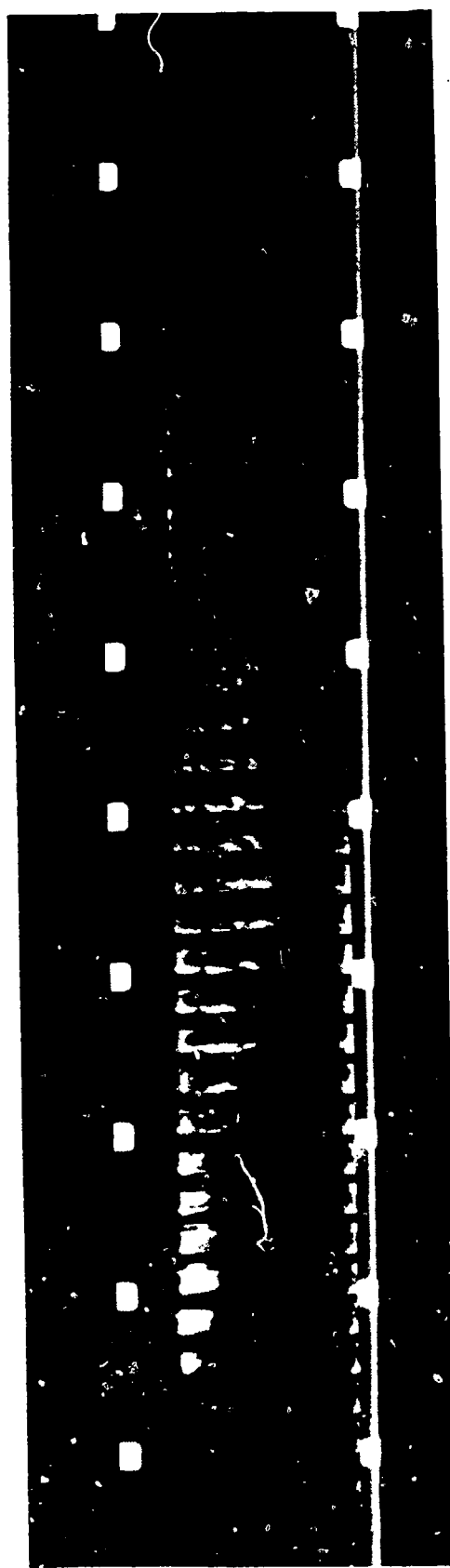


Fig. 21 Photograph for a Typical Test with Air in the Chamber

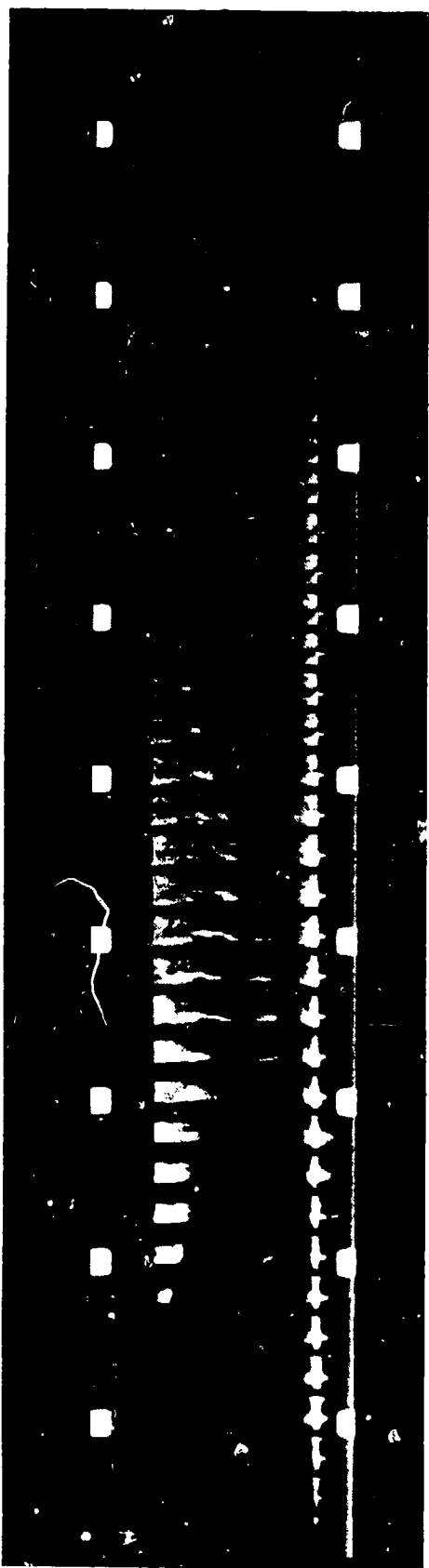


Fig. 22 Photograph for a typical test with Nitrogen Purged Chamber

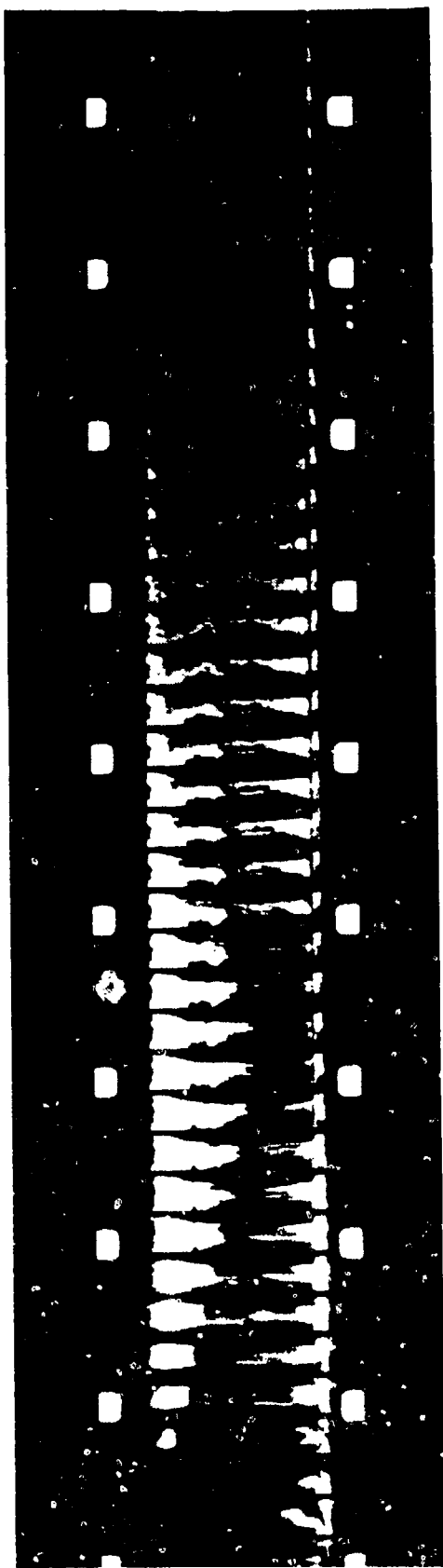


Fig. 25 Photograph for a Typical Test with Additional Powdered Propellant in Igniter Chamber

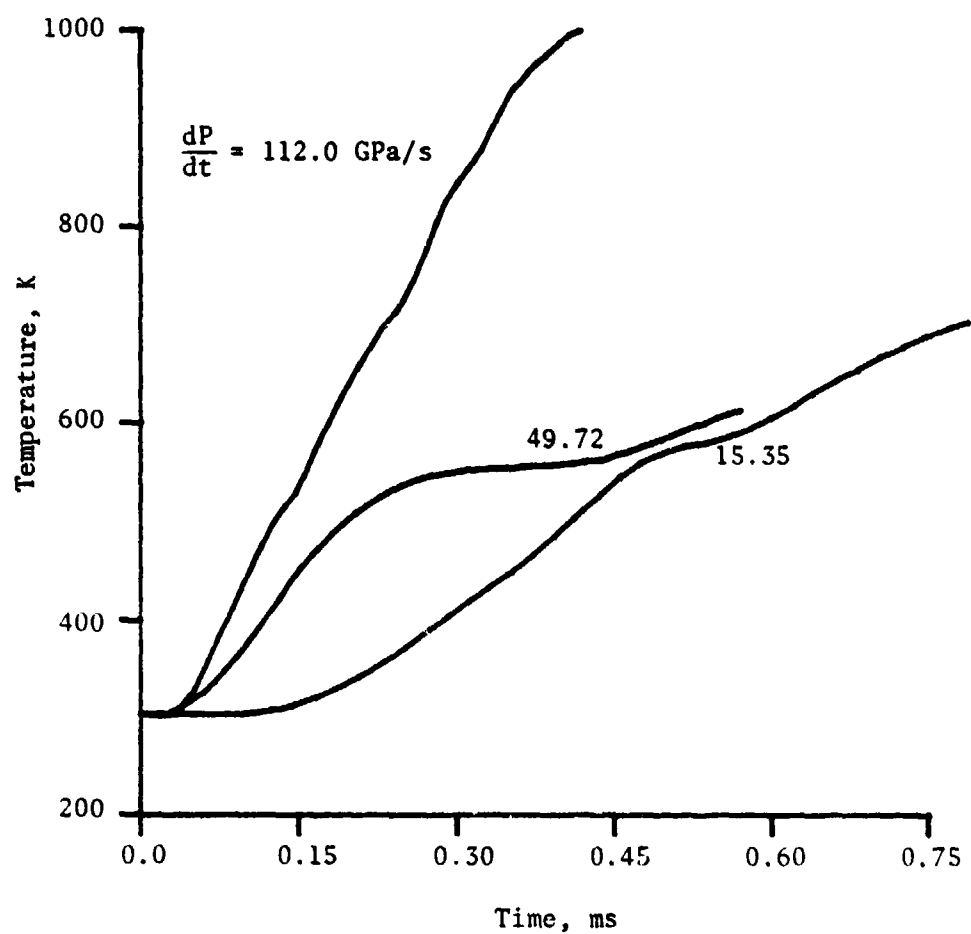


Fig. 24 Measured Temperature-Time Traces from Heat Flux Gage

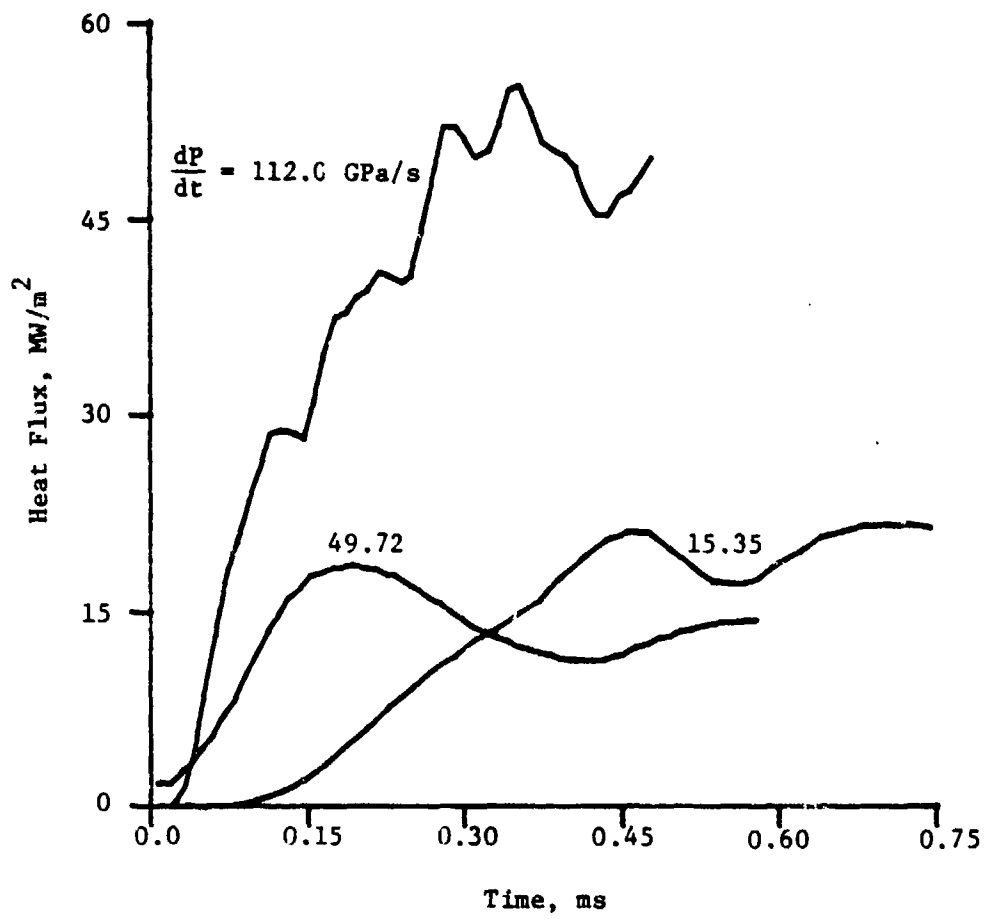


Fig. 25 Deduced Heat Flux-Time Traces

operating conditions (in the order of 10 MW/m^2 or $250 \text{ cal/cm}^2\text{-s}$), and that the heat flux to the propellant surface increases with the increased rate of pressurization. For the time period specified in Figs. 24 and 25, measured temperature continually increases and heat flux to the propellant surface is always positive because the hot igniter gases continue to flow into the crack cavity during this short period of time.

The increase in heat flux to the propellant surface at an increasing rate of pressurization can be attributed to a combination of the following. At higher pressurization, heat transfer to the propellant, from both the reflected compression wave and the hot recirculating gases near the tip, will be higher.²⁵ Photographs of the ignition event presented in Figs. 20-23 show that at higher pressurization some of the unreacted species or particles from the igniter grain or booster propellant, which did not have sufficient time to burn completely, may become entrained and carried by the hot gases to the tip and burn there. Because of continued pressurization of the crack cavity, the enthalpy of gases adjacent to the propellant surface will increase, which in turn increases the rate of heat transfer to the propellant surface.

The effect of pressurization rate at the tip on measured ignition delay time is shown in Fig. 26. It can be seen that the ignition delay decreases as the pressurization rate increases because the rate of heat transfer to the propellant surface increases as the pressurization rate is increased. It is interesting to note that the ignition delay is in the submillisecond range for pressurization rates of the order of 10 GPa/s or higher. Scatter in the experimental data appears to be more pronounced at lower pressurization rates; this may be attributed to the lower rate of heat transfer to the propellant under these conditions. Figure 26 also shows that crack-gap width has no distinguishable effect on the ignition process. Data for the smallest gap width ($\delta = 1.17 \text{ mm}$) appear to be concentrated at lower pressurization rates; because no diaphragm was

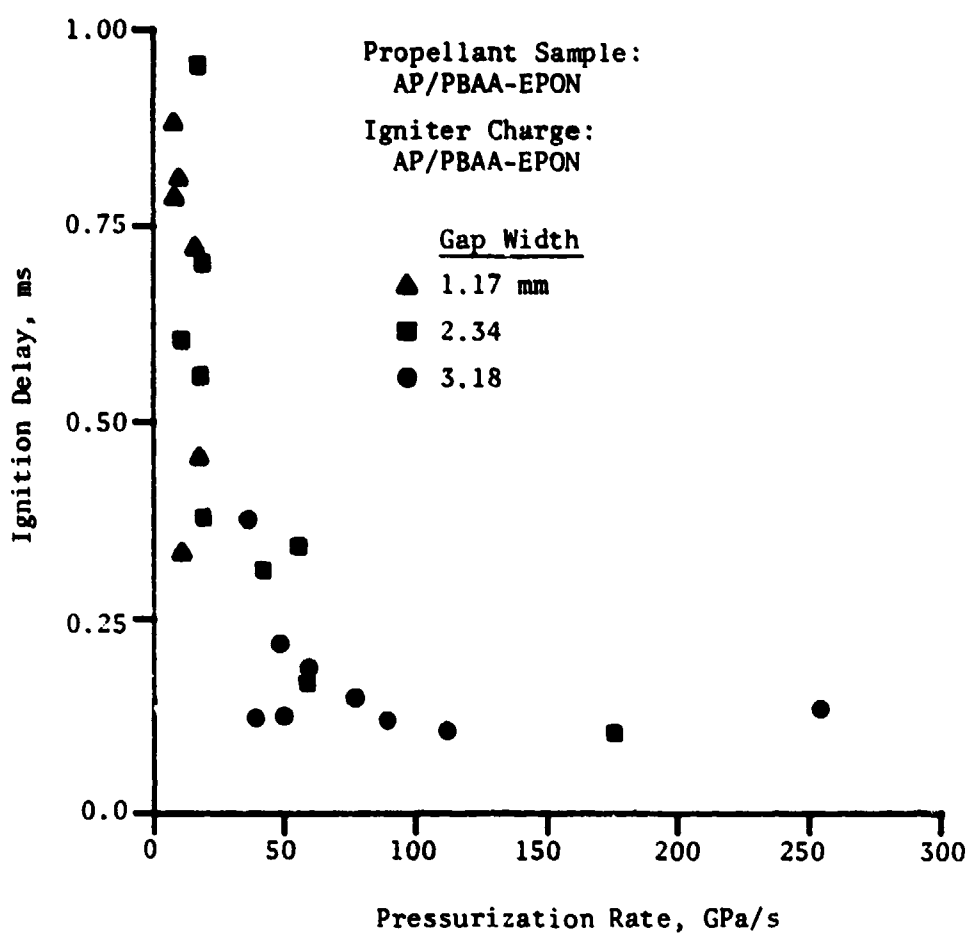


Fig. 26 Measured Ignition Delay versus Local Pressurization Rate for Various Gap Widths

inserted between the igniter and combustion chambers for tests with the smallest gap width, lower pressurization rates were obtained.

Experiments were also conducted to evaluate the effect of igniter gas temperature on the ignition process. An aluminized AP-based composite propellant was used as the igniter for these studies. The flame temperature of this propellant is 3600 K. Because of the very high luminosity of the product gases from this propellant, it was difficult to accurately measure the ignition delay. Limited results obtained from these tests indicate that the ignition-delay time is somewhat lower for high-flame temperature igniter gases. This is to be expected, since the rate of heat transfer to the propellant will increase with higher gas temperatures.

Table 3 lists the values and sources of physical properties and input parameters used in the calculations. Thermal properties of AP were taken from Ref. 26. Thermal properties of PBAA are approximate, and are identical to those used by Varney and Strahle.¹⁶ Density of the fuel binder in the table is weighted average density of PBAA and EPON. Conductivity of PBAA was deduced from this average density and the value of thermal diffusivity used in Ref. 16 for fuel binders. The values of in-depth radiation absorption coefficient β are considered to be equal for both oxidizer and fuel, and are identical to those used in Refs. 29-31. Separate values of β for AP and PBAA were not found in propellant literature. In the present study, radiation is less than 2.5% of the total heat flux to the propellant; in-depth radiation absorption, therefore, does not play a significant role in the overall ignition process.

The ignition criterion for the theoretical analysis was based upon attainment of a critical temperature at the oxidizer fuel-binder interface on the propellant surface. This temperature was denoted as 623 K (350°C), which is the accepted decomposition temperature of AP.^{14,34} Because of the heterogeneous nature of the propellant, the AP and the fuel binder have different temperatures at any axial location; therefore, the ignition criterion was based upon the temperature at the AP-fuel interface. Photochemical reactions were not considered in the computations.

Table 3 Physical Properties and Input Parameters

<u>Property</u>	<u>Units</u>	<u>AP</u>	<u>PBAA</u>
c	J/kg-K	1305.4 ^{26,27}	1255.2 ¹⁶
E _{py}	kJ/gmol	134 ²⁸	142 ¹⁶
k	W/m-K	0.46 ²⁶	0.12 ¹⁶
L	μm	50	--
Q _{py}	kJ/kg	-502 ^{10,15}	8159 ¹⁶
R ₁	μm	30.62	--
R ₂	μm	--	39.76
Z _{py}	s ⁻¹	1.0 x 10 ⁹ (Ref. 28)	2.0 x 10 ⁷ (Ref. 16)
β	m ⁻¹	1.0 x 10 ⁴ (Ref. 29-31)	1.0 x 10 ⁴ (Refs. 29-31)
ρ	kg/m ³	1950 ³²	947 ³³

Figure 27 shows the comparison between measured and predicted ignition delays. Theoretical values appear to predict accurately the functional dependence of ignition delay on the pressurization rate. The variation in the predicted ignition delay when there is a ± 25 K change in the ignition temperature is also shown in the figure. At low pressurization rate, the variation is large because of lower heat flux to the propellant. It should be noted that only representative values of predicted ignition delays are shown in Fig. 27; there is also some scatter in the predicted results because actual measured heat flux is an input to the theoretical model.

Figure 28 presents a plot of the calculated radial variation of propellant surface temperature at three different times. The temperature profiles at these specified times are quite similar. Temperature in the fuel binder is higher than that in the oxidizer crystal because the thermal diffusivity of fuel is lower. Even though the pyrolysis reaction for the fuel is endothermic, it has little effect on the temperature profiles since appreciable pyrolysis reaction does not occur in the temperature range shown in Fig. 28. It is also evident that except near the oxidizer-fuel interface, the radial temperature gradients are very small as a result of adiabatic radial boundaries.

Figure 29 shows the predicted axial variation of the oxidizer-fuel interface temperature at various times for conditions corresponding to Fig. 28. The thermal wave penetration depth is extremely small ($< 20 \mu\text{m}$) because the heat flux to the propellant surface is very large (in the order of 10 MW/m^2) and the time duration is very short (submilliseconds). If a significant portion of the incident heat flux is radiative, the thermal wave will penetrate deeper than that shown in the figure. In the present study, as noted earlier, a very small portion ($< 2.5\%$) of the incident heat flux is radiative.

Figure 30 is a plot of the calculated propellant surface temperature at the oxidizer-fuel interface as a function of time for pressurization rates of 15.35,

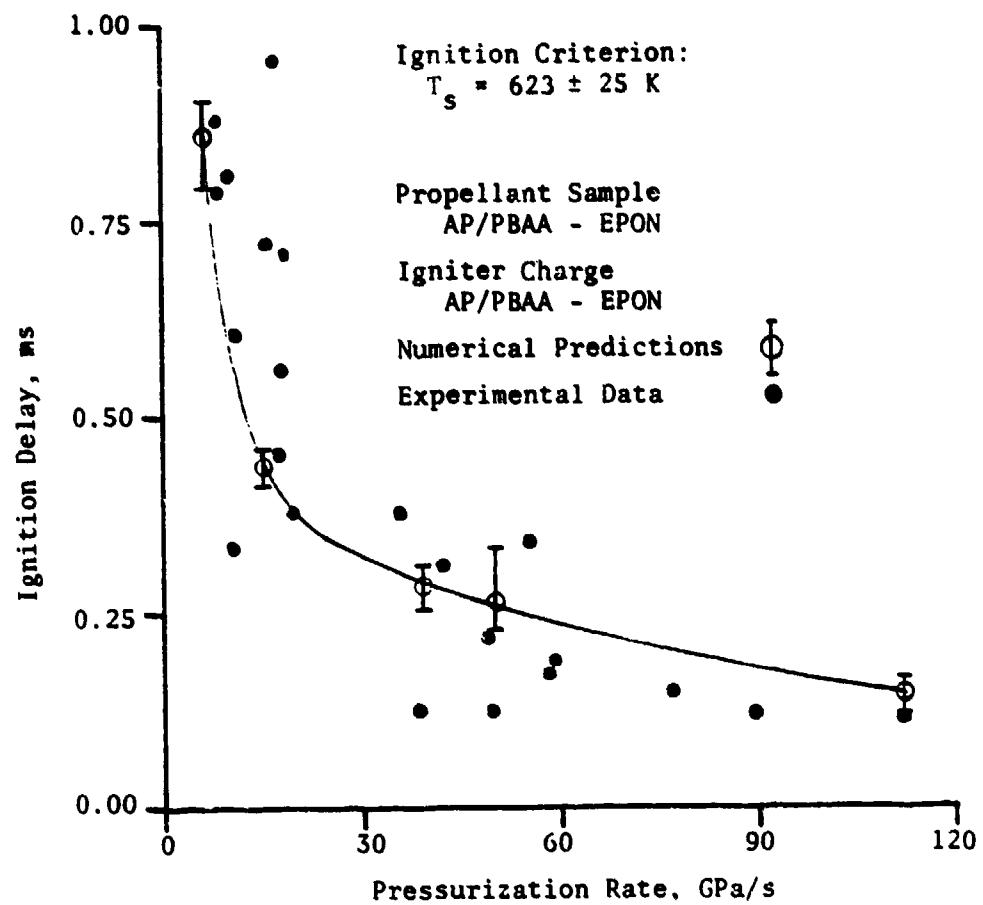


Fig. 27 Comparison Between Predicted and Measured Ignition Delays

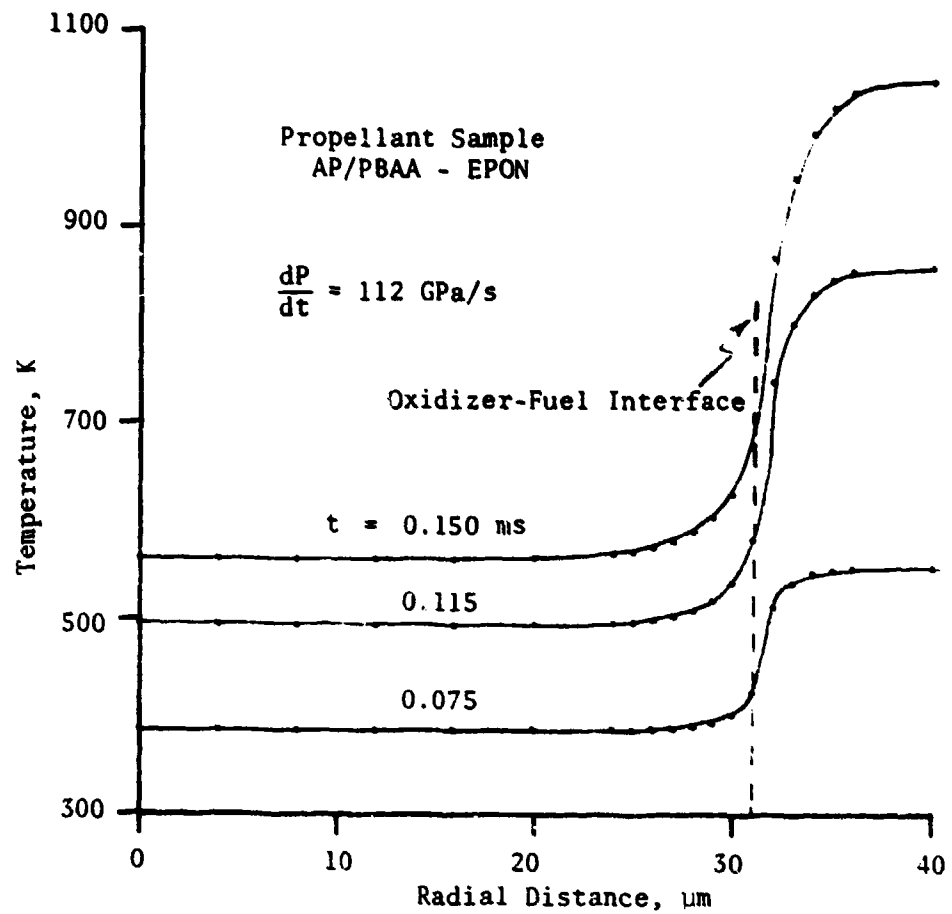


Fig. 28 Calculated Radial Variation of Propellant Surface Temperature

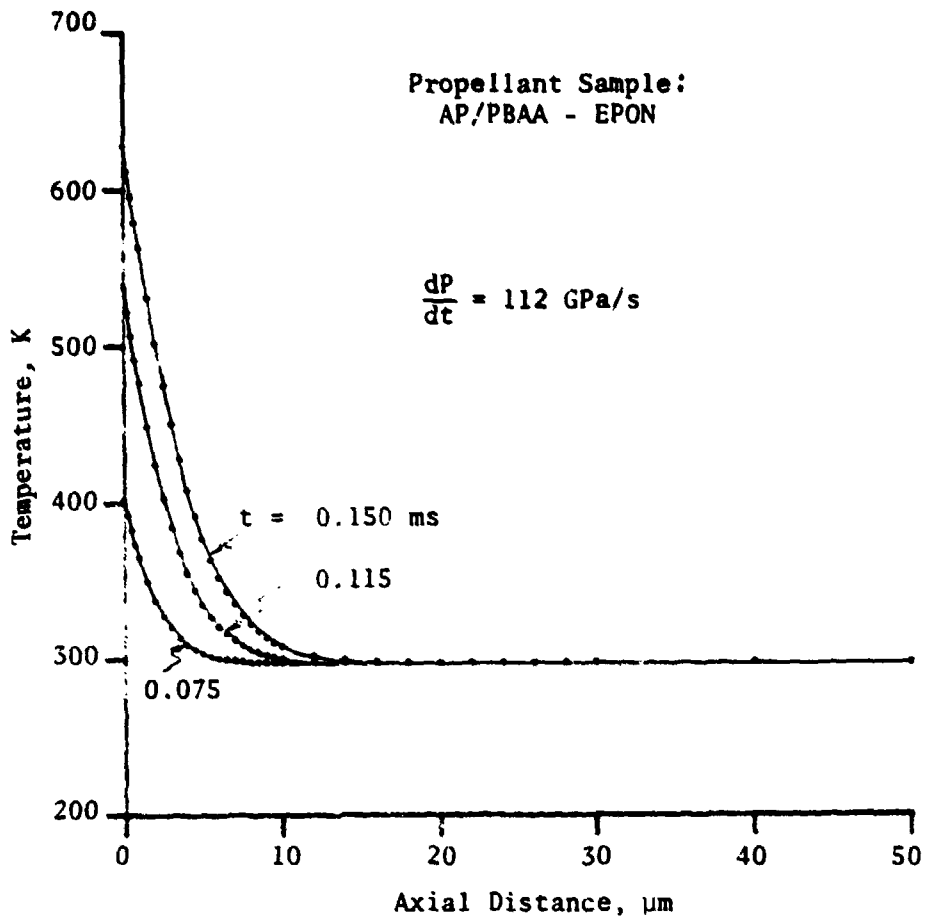


Fig. 29 Calculated Axial Variation of Oxidizer-Fuel Interface Temperature

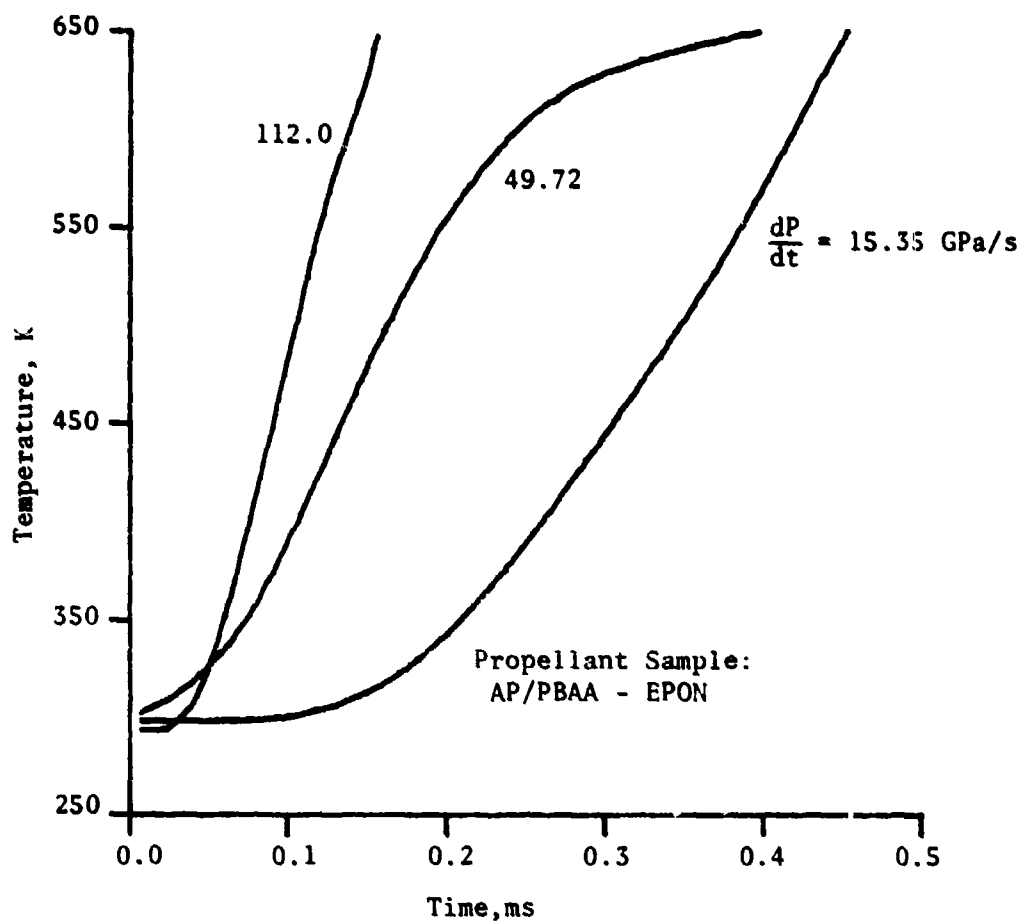


Fig. 30 Calculated Variations of Propellant Surface Temperature at the Oxidizer Fuel Interface with Time

49.72, and 112 GPa/s. The input heat flux for these cases is presented in Fig. 25. Since the heat flux to the propellant surface increases with higher pressurization, the average slopes of the curves in Fig. 30 also increase with higher pressurization. The time variation of surface temperature for a given pressurization rate depends strongly on the corresponding heat-flux time data.

V. SUMMARY OF PROGRESS AND CONCLUSIONS

Progress made during the past year and the results obtained can be summarized as follows:

1. Detailed chemical kinetics information for the AP/PBAA propellants was incorporated into the proposed theoretical model for ignition of composite solid propellants. This enables a more complete description of source terms in the gas-phase energy and species equations.
2. Solid-phase energy equations were coded and implemented on a computer. The numerical scheme employs a stable, implicit scheme for solution of the governing equations. Numerical solutions of the solid-phase subprogram were successfully checked against analytic solutions for some limiting cases. Using actual, measured heat flux near the propellant surface as an input to the solid-phase equations, predictions for the ignition delay time can be made.
3. Numerical solution of the complete model is in progress. An overall solution scheme was established, and a portion of the gas-phase finite difference equations was coded.
4. The test chamber was modified to house the heat flux gage, pressure transducer, etc., near the propellant sample. A new igniter system, which uses electric primers, was designed and fabricated. With the present setup, pressurization rates in the order of 100 GPa/s ($\sim 10^6$ atm/s) were obtained.
5. The data acquisition system was updated by acquiring and installing a 2 MHz transient waveform recorder and digitizer; by interfacing the digitizer with a minicomputer; and by upgrading the movie camera system to reach 40,000 pictures per second. A photodiode system was installed to detect onset of ignition.
6. Test firings were conducted to investigate effects of pressurization rate dP/dt , crack-gap width δ , and igniter flame temperature on the ignition process. The ignition delay time was simultaneously recorded, using the Hycam camera and the fast-response photodiode system.

7. Heat flux to the propellant surface was deduced from the temperature-time profile measured by a fast-response (5-10 μ s) thin film thermocouple, using a numerical integration procedure.

8. Experimental results indicate that the ignition delay time decreases and the heat flux to the propellant surface increases as the pressurization rate is increased. No distinguishable effect of the crack-gap width on the ignition process was evident. Limited results obtained by using an aluminized propellant as the igniter show that the ignition delay time is somewhat lower for high-flame temperature igniter gases.

9. Theoretical predictions made using the solid-phase equations show reasonable comparison with experimental data. Theoretical results also indicate that the ignition delay time decreases as the pressurization rate is increased.

10. The decrease in ignition delay with increasing pressurization is caused by enhanced heat feedback to the propellant surface at higher pressurization rates. This augmentation in heat feedback to the propellant at higher pressurization is a result of a combination of the following mechanisms: heating due to compression wave reflection at the closed end; heat transfer due to recirculating hot gas near the tip; heat release by burning of unreacted igniter species (or particles) near the tip, behind the compression wave; and increase in enthalpy of the gas adjacent to the propellant surface due to continued pressurization of the crack cavity.

VI. NOMENCLATURE

<u>Symbol</u>	<u>Description</u>
A	axial transformation constant for the gaseous region
c, c_p	specific heat
D	binary mass diffusion coefficient
E	activation energy
E_b	black body radiation intensity
G	external radiation heat flux
I_z	local radiation flux at z
k	thermal conductivity
k_i	rate constants for reaction i
L	thickness of the oxidizer pellet
m	constant defined in Eq. (31)
P	pressure
\dot{q}''	heat flux (energy per unit time per unit area)
\dot{q}'''	heat generation rate (energy per unit time per unit volume)
$Q_{pc\lambda}$	rate of heat generation due to photochemical process per unit wavelength/local radiation flux at z
Q_{py}	heat of pyrolysis per unit mass
r	radial distance from the center of the statistically averaged element
r_b	burning rate
R_u	universal gas constant
R_1, R_2	radii of outer surfaces of oxidizer particle and fuel binder, respectively
s	transformed nondimensional axial coordinate in gas phase
t	time
T	temperature
v_z	gas phase velocity in z direction
\bar{w}	average molecular weight
Y_j	mass fraction of species j in the gas phase

<u>Symbol</u>	<u>Description</u>
z	distance from the initial ($t=0$) position of the interface; positive in the gas phase
Z	pre-exponential factor
α	radiation absorptivity of the interface
β	in-depth radiation absorption coefficient
ϵ	emissivity of the interface
η_λ	efficiency for photochemical process at wavelength λ
λ	wavelength of external radiation
ρ	density
τ	transmissivity of the solid phase
$\dot{\omega}''$	mass production rate per unit area
$\dot{\omega}'''$	mass production rate per unit volume
ξ	axial coordinate in solid phase ($\Xi - z$)

Subscripts

1,2,3,4,5 various reactions or species

F fuel

F-g fuel-gas interface

g gas phase

i initial value

j Species j

Ox oxidizer

Ox-F oxidizer-fuel interface

Ox-g oxidizer-gas interface

pc photochemical

py pyrolysis

s solid phase

s-g solid-gas interface

z

in z direction (perpendicular to the initial position of
the interface)

∞

far away from the interface in z direction

λ

wavelength

VII. REFERENCES

1. Kuo, K. K., Kumar, M., and Kulkarni, A. K., "Transient Ignition Mechanism of Confined Solid Propellants under Rapid Pressurization," Summary Report to ONR, Aug. 1980.
2. Kulkarni, A. K., Kumar, M., and Kuo, K. K., "Review of Solid Propellant Ignition Studies," AIAA Paper 80-1210, presented at the AIAA/SAE/ASME 16th Joint Propulsion Conference, Hartford, Conn., July 1980.
3. Chang, T. Y., Chang, J. P., Kumar, M., and Kuo, K. K., "Combustion - Structural Interaction in a Viscoelastic Material," Proceedings of the Symposium on Computational Methods in Nonlinear Structural and Solid Mechanics, Washington, D.C., NASA CP-2147, Oct. 1980, pp. 67-90.
4. Kumar, M. and Kuo, K. K., "Effect of Propellant Deformation on Ignition and Combustion Processes in Solid Propellant Cracks," Proceedings of the 1980 JANNAF Propulsion Systems Hazards Subcommittee Meeting, Monterey, CA, CPIA Publication 330, Dec. 1980, pp. 203-238.
5. Kovacic, S. M., Kumar, M., and Kuo, K. K., "Improved Prediction of Flame Spreading During Convective Burning in Solid Propellant Cracks," Seventh Symposium (International) on Detonation, Annapolis, MD., Preprint Vol. 1, June 1981, pp. 104-114.
6. Kumar, M., Kovacic, S. M., and Kuo, K. K., "Flame Propagation and Combustion Processes in Solid Propellant Cracks," AIAA Journal, Vol. 19, May 1981, pp. 610-618.
7. Kulkarni, A. K., Kumar, M., and Kuo, K. K., "A Comprehensive Ignition Model for Composite Solid Propellants," to be presented at the 18th JANNAF Combustion Meeting, Pasadena, CA, Oct. 19-23, 1981.
8. Wills, J. E., Kumar, M., Kulkarni, A. K., Hund, M., and Kuo, K. K., "Investigation of Composite Propellant Ignition under Rapid Pressurization," to be presented at the 18th JANNAF Combustion Meeting, Pasadena, CA, Oct. 19-23, 1981.
9. Ohlemiller, T. J. and Summerfield, M., "A Critical Analysis of Arc Image Ignition of Solid Propellants," AIAA Journal, Vol. 6, May 1968, pp. 878-886.
10. Lengelle, G., Brulard, J., and Moutet, H., "Combustion Mechanisms of Composite Solid Propellants," Sixteenth Symposium (International) on Combustion, Combustion Institute, Pittsburgh, PA, 1976, pp. 1257-1269.
11. Waesche, R. H. W., "Research Investigation of the Decomposition of Composite Solid Propellants," United Aircraft Corporation Research Laboratories, East Hartford, Conn., Report No. H910476-36, Sept. 1969.
12. Kishore, K., Pai Verneker, V. R., and Mohan, V. K., "Differential Scanning Calorimetric Studies on AP," Thermochimica Acta, Vol. 13, 1975, pp. 277-292.
13. Manelis, G. B. and Strunim, V. A., "The Mechanism of AP Burning," Combustion and Flame, Vol. 17, 1971, pp. 69-77.

14. Guirao, C. and Williams, F. A., "A Model for Ammonium Perchlorate Deflagration Between 20 to 100 atm," AIAA Journal, Vol. 9, July 1971, pp. 1345-1356.
15. Beckstead, M. W., Derr, R. L., and Price, C. F., "A Model of Composite Solid-Propellant Combustion Based on Multiple Flames," AIAA Journal, Vol. 8, Dec. 1970, pp. 2200-2207.
16. Varney, A. M. and Strahle, W. C., "Thermal Decomposition Studies of Some Solid Propellant Binders," Combustion and Flame, Vol. 16, 1971, pp. 1-7.
17. Kashiwagi, T., Macdonald, B. W., Isoda, H., and Summerfield, M., "Ignition of a Solid Polymeric Fuel in a Hot Oxidizing Gas Stream," Thirteenth Symposium (International) on Combustion, The Combustion Institute, Pittsburgh, PA, 1970, pp. 1073-1086.
18. Beddini, R. A. and Varma, A. K., "Analysis of Ammonium Perchlorate Combustion in a Turbulent Flow," Proceedings of the 16th JANNAF Combustion Meeting, Monterey, CA, CPIA Publication 308, Vol. II, Sept. 1979, pp. 193-210.
19. Annon, "Film Thermocouples for Transient Heat Transfer and Surface Temperature Measurements," Bulletin 600, Medtherm Corporation, Huntsville, Alabama.
20. Vidal, R. J., "Transient Surface Temperature Measurements," Symposium on Measurements in Unsteady Flow, ASME, New York, 1962, pp. 90-99.
21. Vidal, R. J., "Model Instrumentation Techniques for Heat Transfer and Force Measurements," Cornell Aeronautical Laboratory Report AD-917-A-1, 1956.
22. Carslaw, H. S. and Jaeger, J. C., Conduction of Heat in Solids, 2nd Ed., Oxford University Press, London, 1959.
23. Cook, W. J. and Felderman, E. J., "Reduction of Data from Thin-Film, Heat-Transfer Gages: A Concise Numerical Technique," AIAA Journal, Vol. 4, March 1966, pp. 561-562.
24. Reinsch, C. H., "Smoothing by Spline Functions," Numerische Mathematik, Vol. 10, 1967, pp. 177-183.
25. Kumar, M. and Kuo, K. K., "Ignition of Solid Propellant Crack Tip Under Rapid Pressurization," AIAA Journal, Vol. 18, July 1980, pp. 825-833.
26. Rosser, W. A., Jr., Inami, S. H., and Wise, H., "Thermal Diffusivity of Ammonium Perchlorate," AIAA Journal, Vol. 4, April 1966, pp. 663-666.
27. Stull, D. R. and Prophet, H., JANAF Thermochemical Tables, 2nd Edition, NSRDS-NBS 37, June 1971.
28. Manelis, G. B., Proschin, A. V., Kubtsov, Yu. I., Strunin, V. A., and Shtenberg, A. S., "Thermal Decomposition Kinetics of Ammonium Perchlorate at High Temperatures," Combustion, Explosion, and Shock Waves, Vol. 4, 1968, pp. 169-175.

29. Kashiwagi, T., "A Radiative Ignition Model of a Solid Fuel," Combustion Science and Technology, Vol. 8, 1974, pp. 225-236.
30. Kumar, R. K., and Hermance, C. E., "Role of Gas-Phase Reactions During Radiant Ignition of Solid Propellants," Combustion Science and Technology, Vol. 14, 1976, pp. 169-175.
31. Mindelan, M., and Williams, F. A., "Gas-Phase Ignition of a Solid with In-Depth Absorption of Radiation," Combustion Science and Technology, Vol. 16, 1977, pp. 47-58.
32. Sarner, S. F., Propellant Chemistry, Reinhold Publishing Corp., New York, 1966.
33. Steinz, J. A., Stang, P. L., and Summerfield, M., "The Burning Mechanism of Ammonium Perchlorate-Based Composite Solid Propellants," Aerospace and Mechanical Sciences Report 830, Princeton University, Feb. 1969.
34. Kishore, K. and Prasad, G., "A Review on Decomposition (Deflagration of Oxidizer and Binder in Composite Solid Propellants)," Defence Science Journal, Vol. 29, 1979, pp. 39-54.

APPENDIX A
(Ref. No. 3)

COMBUSTION - STRUCTURAL INTERACTION IN
A VISCOELASTIC MATERIAL*

T. Y. Chang and J. P. Chang
Department of Civil Engineering
The University of Akron, Akron, Ohio

M. Kumar and K. K. Kuo
Department of Mechanical Engineering
The Pennsylvania State University
University Park, Pennsylvania

SUMMARY

The effect of interaction between combustion processes and structural deformation of solid propellant was considered. The combustion analysis was performed on the basis of deformed crack geometry, which was determined from the structural analysis. On the other hand, input data for the structural analysis, such as pressure distribution along the crack boundary and ablation velocity of the crack, were determined from the combustion analysis. The interaction analysis was conducted by combining two computer codes, a combustion analysis code and a general purpose finite element structural analysis code.

INTRODUCTION

In recent years, much attention has been focused on the investigation of the coupling effect between combustion phenomenon and mechanical behavior of solid propellant. The solution of problems of this type can further better understanding of the transient combustion processes inside solid propellant cracks, which may significantly affect the performance of a rocket motor. The combustion phenomenon inside the crack of solid propellant is strongly influenced by the crack geometry as the material is being deformed and burned away. Generally, there are two major reasons for alteration of the crack geometry: 1) mass loss due to gasification of propellant surface along the crack during the combustion process, and 2) mechanical deformation of the propellant due to pressure.

On one hand, both the burning rate and mechanical deformation are governed by pressure acting on the crack surface. On the other hand, a change in crack size will cause the pressure distribution to vary. The pressure distribution will strongly influence the deformation and stress concentration at the crack

*Research sponsored by the Power Program of the Office of Naval Research Arlington, Va., under Contract No. N00014-79-C-0762. The support of Dr. R. S. Miller is gratefully acknowledged. A part of this work was performed under a previous contract sponsored by Dr. R. L. Derr of NWC. His support is also appreciated.

tip, which in turn will affect the manner of the crack propagation. It is, therefore, apparent that the pressure distribution and the change in crack geometry are strongly interdependent.

In the past, combustion and structural analyses of solid propellant were conducted independently, with the result that interaction effects were completely ignored. As noted above, such interaction effects can be quite important, especially when the deformation is large as compared to the original crack-gap width. The deformation response of the material is categorized as linearly viscoelastic. It is, therefore, the intent of this paper to present a method of analysis for the combustion-structural interaction in a linear viscoelastic medium. To this end, three major tasks are involved: 1) combustion analysis to model the transient combustion process, 2) viscoelastic analysis in conjunction with moving boundary, and 3) linkage of the two analyses.

For the combustion analysis, investigations of certain aspects of combustion processes have been made. Taylor [1] conducted experimental tests to study the convective burning of porous propellants with closed- and open-end boundary conditions. Belyaev et al. [2] showed that the burning of propellant inside a narrow pore may lead to an excess pressure buildup. In a later study, Belyaev et al. [3] made a series of experimental tests to determine the dependence of flame-spreading rate on crack geometry, propellant properties, boundary conditions, and combustion chamber pressures. Cherepanov [4] stated that as a result of the impeded gas flow in a sufficiently narrow and long cavity, the pressure reaches such high values that the system becomes unstable. From his work, Godai [5] indicated that there is a threshold diameter or critical width of a uniform cavity below which flame will not propagate into the crack. Krasnov et al. [6] investigated the rate of penetration of combustion into the pores of an explosive charge. Jacobs et al. [7,8] studied the pressure distribution in burning cracks that simulate the debonding of solid propellant from the motor casing.

Although results of previous experiments were of interest, no sound theoretical model was developed. In this study, a theoretical model was established for predicting rate of flame propagation, pressure distribution, and pressurization rate inside the crack. Two sets of coupled partial differential equations were obtained: one from mass, momentum, and energy conservation of the gas phase of the propellant product in the void region adjacent to the crack surface; the other from consideration of solid-phase heat conduction. Due to the mathematical complexity of governing equations and boundary conditions involved, the finite difference method was used to obtain the solution for the combustion analysis. In the numerical solution, the boundary conditions, which vary with time, are specified in terms of the changing crack geometry, which in turn is found from the structural analysis. In addition, the pressure distribution along the crack surface, varying as a function of time, was obtained from the analysis and was used as input for the structural analysis.

For structural analysis, different approaches have been taken previously in solving (analytically or numerically) several moving boundary problems in linear viscoelasticity. Lee et al. [9] obtained a solution for the pressurization of an annihilating viscoelastic cylinder contained by an elastic casing in which the material was assumed to be a Kelvin model in shear and incompressible in bulk. Arenz et al. [10] performed a similar analysis for a sphere. Corneliusen et

al. [11,12] presented solutions for a spinning, annihilating, viscoelastic cylinder with free outer boundary. Since the constraining case was not included in their analyses, the stress distribution was independent of the material properties. With the assumption of a standard linear solid model, Shinozuka [13] presented the analytical solution for a case-bonded pressurized viscoelastic cylinder. More generalized solutions were obtained by Rogers et al. [14] for a class of linear viscoelastic problems by using the numerical integration scheme. Schapery [15] also developed a general method for solving moving boundary problems. In his approach, the moving boundary condition was replaced by a fictitious non-moving boundary subjected to a time-dependent pressure. Later, Christensen et al. [16] obtained a series solution for the stresses of the same problem. As noted above, most of the analytical solutions were available for viscoelastic problems of simple geometry. For complex geometry, the finite element method has proven to be most useful.

Application of the finite element method for solving viscoelastic problems is not new; reports of such work can be found, for instance, in references [17-20]. However, most of the previous work did not consider the effect of moving boundary, an important feature for the structural analysis of solid propellant. Sankaran and Jana [21] presented a technique for the solving of axisymmetric viscoelastic solids with moving boundary. In their approach, the finite element mesh corresponding to the new boundary was re-generated, while the stress-strain histories and material properties were assumed to be carried over from those of the previous time increment. This assumption is valid only if the time increment is very small. An algorithm for automatically tracking ablating boundaries was given by Weeks and Cost [22]. All previous work dealing with moving boundary viscoelastic problems lacks both the appropriate treatment of material properties, and stress-strain histories for the newly generated mesh. It is the purpose of this paper to present such a treatment.

Three major features must be included in the structural analysis for a solid propellant: 1) proper modeling of viscoelastic behavior, 2) tracking of ablating boundary in order to generate new finite element meshes, and 3) treatment of the material responses (i.e., stress-strain histories and material properties) for the new mesh. All of these features have been incorporated into a nonlinear finite element program called NFAP [23]. Combustion and structural programs were combined in order to make possible an interaction analysis. Numerical results are presented to demonstrate the effect of interaction between combustion and structural responses of the material.

COMBUSTION ANALYSIS

The theoretical model was developed to simulate the combustion phenomenon inside a propellant crack, which is located in a transverse direction to the main flow of the rock chamber. During the course of derivation, the following assumptions are made:

- 1) All chemical reactions occur near the propellant crack surface, and the combustion zone is so thin that it is considered a plane.
- 2) Rate processes at the propellant surface are quasi-steady in the sense that characteristic times associated with the gaseous flame and preheated propellant are short in comparison to that of pressure transient variation.

- 3) Gases flowing in the propellant crack obey the Clausius or Noble-Abel equation of state.
- 4) Bulk flow in the pore is one-dimensional [24].

To describe gas-phase behavior inside a solid propellant crack, mass, momentum, and energy equations in unsteady, quasi-one-dimensional forms have been developed, based upon the balance of fluxes in a control volume within the propellant crack.

The mass conservation equation is

$$\frac{\partial(\rho A_p)}{\partial t} + \frac{\partial(\rho u A_p)}{\partial x} = r_b \rho_{pr} P_b \quad (1)$$

The momentum conservation equation is

$$\begin{aligned} \frac{\partial}{\partial t} (\rho u A_p) + \frac{\partial}{\partial x} (\rho A_p u^2) &= - A_p \frac{\partial P}{\partial x} + \frac{\partial}{\partial x} (A_p \tau_{xx}) \\ &- \tau_w P_w \cos \theta_w + \rho A_p B_x - (\rho_{pr} r_b P_b) V_{gf} \sin \theta_w \end{aligned} \quad (2)$$

The energy conservation equation written in terms of the total stored energy (internal and kinetic) per unit mass, E, is

$$\begin{aligned} \frac{\partial}{\partial t} (\rho A_p E) + \frac{\partial}{\partial x} (\rho A_p u E) &= \frac{\partial}{\partial x} (\lambda A_p \frac{\partial T}{\partial x}) - \frac{\partial}{\partial x} (A_p \rho u) \\ &+ \frac{\partial}{\partial x} (\tau_{xx} A_p u) + \rho_{pr} r_b P_b h_f - \bar{h}_{cp} P_b (T - T_{ps}) \\ &+ B_x \rho A_p u - \bar{h}_{cv} (P_w - P_b)(T - T_{ws}) \end{aligned} \quad (3)$$

The conservation equations are further simplified by an order of magnitude analysis in which the following terms are negligible: 1) forces between molecules due to viscous normal stress in axial direction; 2) viscous dissipation and rate of work done by the force caused by viscous normal stresses in the energy equation; and 3) axial heat conduction between gas molecules in the energy equation.

The propellant surface temperature at a fixed location along the crack before the attainment of ignition is calculated from the solid-phase heat conduction equation written in unsteady one-dimensional form:

$$\frac{\partial T_{pr}(t,y)}{\partial t} = \alpha_{pr} \frac{\partial^2 T_{pr}(t,y)}{\partial y^2} \quad (4)$$

where the length variable y is measured perpendicular to the local propellant crack surface. Initial and boundary conditions are

$$T_{pr}(0, y) = T_{pi} \quad (5)$$

$$T_{pr}(t, \infty) = T_{pi} \quad (6)$$

$$\frac{\partial T_{pr}}{\partial y}(t, 0) = -\frac{\bar{h}_c(t)}{\lambda_{pr}} [T(t) - T_{ps}(t)] \quad (7)$$

The heat conduction equation is solved by using an integral method [25] which employs a third-order polynomial, or by direct numerical solution of Eqs. (4-7) with variable mesh size in the subsurface.

For the gas phase, the Noble-Abel equation is used for the equation of state:

$$p(\frac{1}{\rho} - b) = RT \quad (8)$$

The gas-phase equations, i.e. Eqs. (1), (2) and (3), are non-linear, inhomogeneous, partial differential equations. Along with the partial differential equation for the solid phase (Eq. (4)), they are solved simultaneously, using the finite difference method. The derivation described above was implemented into a computer program, crack combustion code (CCC) by Kuo et al. [26].

STRUCTURAL ANALYSIS

To conduct the structural analysis of the solid propellant, three main features must be included in the numerical formulations: 1) modeling of viscoelastic material behavior, 2) simulation of ablating boundary, and 3) treatment of material responses by an interpolation scheme. Each feature is outlined below.

Viscoelastic Material Model

The material behavior of the solid propellant is assumed to be viscoelastic in shear and elastic in bulk. Only the isothermal condition is considered. The stress-strain relations with zero initial conditions are written in two parts.

1) Shear behavior:

$$S_{ij} = \int_0^t G_1(t-t') \frac{d}{dt'} e_{ij}(t') dt' \quad (9)$$

where G_1 is the relaxation modulus in shear. For most viscoelastic materials, it is usually considered

$$G_1 = g_0 + \sum_{m=1}^M g_m e^{-\beta_m t} \quad (10)$$

2) Bulk behavior:

$$\sigma_{kk} = 3K \epsilon_{kk} \quad (11)$$

As discussed in [27], the incremental stress-strain relations in matrix form are written as

$$\{\Delta\sigma\} = [D_{VE}] \{\Delta\epsilon\} - \{\sigma_0\} \quad (12)$$

where $\{\Delta\sigma\}^T = \{\Delta\sigma_{22}, \Delta\sigma_{33}, \Delta\tau_{23}, \Delta\sigma_{11}\}$ (13)

$$\{\Delta\epsilon\}^T = \{\Delta\epsilon_{22}, \Delta\epsilon_{33}, \Delta\epsilon_{23}, \Delta\epsilon_{11}\} \quad (14)$$

$$\{\sigma_0\}^T = \sum_{m=1}^M B_m \{c_m^t, c_{22}^t, c_{33}^t, c_{23}^t, c_{11}^t\} \quad (15)$$

and

$$[D_{VE}] = \begin{bmatrix} (K + \frac{2}{3}A) & (K - \frac{1}{3}A) & 0 & (K - \frac{1}{3}A) \\ & (K + \frac{2}{3}A) & 0 & (K - \frac{1}{3}A) \\ & & \text{symmetric} & \frac{A}{2} & 0 \\ & & & & (K + \frac{2}{3}A) \end{bmatrix} \quad (16)$$

Furthermore,

$$A = g_0 + \sum_{m=1}^M g_m (1 - e^{-\beta_m \Delta t}) / (\beta_m \Delta t) \quad (17)$$

$$B_m = 1 - e^{-\beta_m \Delta t} \quad (18)$$

and the term c_{ij}^t has a recursive relationship, i.e.,

$$m^C_{ij}^t = e^{-\beta_m \Delta t} m^C_{ij}^{t-\Delta t} + \frac{g_m (1-e^{-\beta_m \Delta t})}{\beta_m \Delta t} e'_{ij} \quad (19)$$

$$e'_{ij} = e_{ij}^t - e_{ij}^{t-\Delta t} \quad (20)$$

The advantage of Eq. (19) is that all of the strain history can be obtained by referring only to information in the previous time step, thus reducing computer storage and numerical calculations.

From the virtual work principle and the relationship of Eq. (12), the finite element equilibrium equations for a typical time interval $[t, t + \Delta t]$ can be derived as

$$[K] \{ \Delta v \} = \{ \Delta f \} - \{ f_o \} \quad (21)$$

where

$$[K] = \int [B]^T [D_{VE}] [B] dv \quad (22)$$

and

$$\{ f_o \} = \int [B]^T \{ \sigma_o \} dv \quad (23)$$

Simulation of Ablating Boundary and Mesh Generation

Burning of the propellant causes a significant change in geometry, thus presenting complications in finite element structural analysis. The effect of ablating boundary is accounted for by redefining the finite element mesh at specified time intervals. This involves two stages of calculations: 1) tracking of the ablating boundary, and 2) generation of new finite element mesh. With some modifications, the procedures adopted herein are similar to those presented in [22].

Consider a structural geometry with ablating boundary. The spatial positions of the ablating boundary are determined by the ablation velocities which are found from the combustion analysis at discrete times. It is assumed that the ablation occurs always in the direction normal to the boundary. For structural analysis, the entire surface is divided into an ablating part and a non-ablating part; each part is formed by discrete line segments joining at the nodes of the finite element mesh. The new position of each line segment is located from the given ablating velocity. Consequently, the new boundary nodes are determined by calculating the intersections of two subsequent new line segments. Likewise, the nodes at the intersections of new ablating and non-ablating boundaries are then determined.

During the locating process, however, some of the boundary nodes may not lie on the new boundary and thus must be eliminated. If the distance from the tip of the normal vector at a new nodal position to any node on the original boundary is less than the value of the normal itself, the node is removed.

In general, the total number of nodes on the boundary at discrete times will be different because some of the nodes have been removed. However, in the analysis it is more convenient to generate a finite element mesh similar to the original one so that interpolation of material response can be made. One way to accomplish this is by keeping the number of boundary nodes constant. Consequently, the boundary nodes are redistributed between two discontinuity points which are specified in the input data in such a way that the lengths of the new line segments have the same ratio as those of the original lines.

Once the new boundary nodes are defined, an automatic mesh generation scheme is used to create the interior nodes for further analysis. Because of its flexibility in obtaining a desirable mesh, a Laplacian-isoparametric grid generation scheme [28] is utilized. However, this method is limited to a geometry bounded by four sides. A finite element mesh is shown in Fig. 1. The coordinates of the i -th interior node can be expressed in terms of those of neighboring nodes by

$$y_i = \frac{1}{4(2-w)} [2(y_{i1} + y_{i2} + y_{i3} + y_{i4}) - w(y_{i5} + y_{i6} + y_{i7} + y_{i8})] \quad (24)$$

$$z_i = \frac{1}{4(2-w)} [2(z_{i1} + z_{i2} + z_{i3} + z_{i4}) - w(z_{i5} + z_{i6} + z_{i7} + z_{i8})] \quad (25)$$

where w is the weighting factor for adjusting the distribution of interior nodes, and $0 \leq w \leq 1$.

Setting up the equations for each interior node yields two systems of simultaneous equations. It is observed that the resulting systems of equations are banded and symmetric. The Gaussian elimination scheme is employed to solve for the coordinates of the interior nodes.

Interpolation of Material Responses

As seen from Eq. (16), the stress increment $\Delta\sigma$ for the time interval $[t, t+\Delta t]$ varies with material properties and with the strain history at both current and previous time steps. When the region of an element changes over a period of time due to ablation, the material response history of the new elements is lost and must be determined by an interpolation procedure from the old elements at previous time steps. Accordingly, the interpolation procedure is carried out on the element level. For calculations, the material responses are separated into two groups: the first includes such variables evaluated at the Gaussian integration points, i.e., $\Delta\sigma_{ij}$, $\Delta\varepsilon_{ij}$, and C^t_{ij} ; the second includes the nodal displacements which are evaluated at nodal points. In the present calculations, two limitations are imposed: 1) eight-node quadrilateral elements are used throughout the analysis; and 2) the four sides of each element remain straight before and after ablation.

- 1) Interpolation of Gaussian variables - It is noted that the quadratic displacement approximation of an eight-node element yields a linear strain variation. With this fact in mind, the quantities of Gaussian variables at nodal points are first evaluated for every old element. As shown in Fig. 2a, b, this can be done by using the linear isoparametric shape functions, namely,

$$\bar{w}_k' = \sum_{i=1}^4 h_i(r_k', s_k') * w_i' \quad k = 1, 2, 3, 4 \quad (26)$$

where $h_i = 1/4(1 + r_i r)(1 + s_i s) \quad i = 1, 2, 3, 4$

For each new element, the local coordinates (r_k, s) of the k -th Gaussian point are known. The global coordinates, (\bar{y}_k, \bar{z}_k) , of that point are, therefore, computed by using the following equations:

$$\begin{aligned} \bar{y}_k &= \sum_{i=1}^4 h_i(r_k, s_k) * y_i \\ (27) \end{aligned}$$

$$\bar{z}_k = \sum_{i=1}^4 h_i(r_k, s_k) * z_i$$

After (\bar{y}_k, \bar{z}_k) are found, the old element to which the point belongs must be identified. A search process based upon the values of r' and s' is developed for this purpose. The search starts from the old element which corresponds to the neighboring elements. Equations for such calculations are given by

$$\begin{aligned} \bar{y}_k &= \sum_{i=1}^4 h_i(r', s') * y_i' \\ (28) \end{aligned}$$

$$\bar{z}_k = \sum_{i=1}^4 h_i(r', s') * z_i'$$

Fig. 2c shows how to identify the element to which the points, (r', s') , belong. Once the location of the point is verified, an interpolation procedure is performed, using the relationship

$$\bar{w}_k = \sum_{i=1}^4 h_i(r', s') * w_i' \quad (29)$$

2) Interpolation of nodal displacements - A similar procedure to that explained above is also used to determine the position of the node in question with reference to the old element. However, the interpolation procedure in Eq. (26) is no longer necessary since the nodal displacements are known. The nodal displacements of the new mesh are computed from

$$d_i = \sum_{i=1}^8 h_i(r', s') * d_i' \quad (30)$$

where h_i are the standard quadratic isoparametric shape functions.

All formulations discussed in this section have been implemented into a general purpose nonlinear finite element program called NFAP for conducting viscoelastic analysis of solid propellant with ablating boundary. Some numerical examples are presented in a later section.

COUPLING EFFECT

For structural analysis, the boundary condition along the crack geometry is defined by pressure distribution which varies with time, and ablation velocity; both are determined from combustion analysis. In the combustion analysis, the regression rate of the propellant is dependent on the deformed crack geometry. Therefore, the two processes are strongly interdependent. Such a coupling effect is obtained by combining the analysis of two computer programs: a crack combustion code (CCC) and a structural analysis code (NFAP). Both codes were developed independently to facilitate program verifications. Linkage of the two codes was made subsequently.

The coupling effect considered in the present analysis is limited to the major parameters, namely pressure loading, ablation velocity, and crack deformation. Pressure and ablation velocity are calculated by the CCC at each nodal point located on a one-dimensional grid along the length of the crack. The analysis of crack combustion incorporates the crack geometry variation caused by both mechanical deformation and mass loss through gasification of the propellant surface. Once the gas-phase equations are solved and the pressures and ablation velocities along the crack are calculated for a given time t , the data are transferred to the NFAP as the input information. NFAP then simulates the updated crack geometry from the ablation velocities and generates a new finite element mesh. With the new mesh and pressure data, NFAP updates the stiffness matrix and interpolates material responses for conducting a quasi-static analysis at time t . After obtaining the deformation, the change in the crack width at each finite different node is calculated and added to the existing crack width. Since the crack width is the input of the combustion analysis, one cycle of calculations is thus completed. The same procedure is followed for every specified time increment.

EXAMPLES

For program verification and demonstration of its analysis capability, three sample problems were run either by NFAP alone or in the combined NFAP/CCC program. The results of the analysis are discussed in the following. The numerical results obtained from CCC alone are contained in reference [26].

1. A Reinforced Thick-walled Cylinder

Figure 3 shows a cylinder of viscoelastic material bonded by a steel casing and subjected to a step-function internal pressure. The example was selected because it is composed of two different materials and the analytical results are readily available for comparison. Only five eight-node axisymmetric elements were used to model the cylinder. The material properties of the elastic casing are

$$E = 2.068 \times 10^6 \text{ MPa} \quad v = 0.3015$$

The material properties of the viscoelastic core are defined by

$$K = 689.5 \text{ MPa} \quad G_1 = 51.71 * \exp(-0.1t) \text{ MPa}$$

In Fig. 4, the variations of circumferential stresses with time are plotted for comparison with the analytical solution obtained in [9]. It is observed that both solutions agree very closely. This problem was analyzed previously by Zienkiewicz et al. [18], using strain rate formulation of the finite element method. However, the formulation presented in the present paper is more easily incorporated into the NFAP program.

2. A Star-shaped Solid Rocket Motor

As an application of the present approach in dealing with the moving boundary, a star-shaped solid rocket motor was analyzed by assuming both a constant and ablating inner boundary. The configuration and finite element mesh are shown in Fig. 5, and the material properties of outer casing and inner propellant are identical to those of the first example. Taking advantage of the symmetry condition, only a 30°-sector was modeled by finite element mesh. The contours of maximum compressive stress analyzed by constant inner boundary at various times are shown in Fig. 5. Comparing the present results with those of [18], it is evident that the general pattern is quite similar but that some small differences do exist. Since the geometry of the rocket motor in [18] was not clearly defined, the difference in dimension used in these two analyses could be the cause of such deviations.

The actual case of a solid rocket motor can be modeled more closely by considering the inner boundary being ablated. Figure 6 shows the contours of maximum compressive stress predicted by NFAP, using the option of moving boundary. The results obtained are quite different from those of [18]. However, observing the differences between Figs. 5 and 6, we can conclude that the results obtained by NFAP are quite reasonable. The solution reveals that the high stress region obtained for ablating boundary propagates faster than that with non-ablating boundary.

3. A Propellant Crack Specimen

As a final example, a propellant crack sample was analyzed, using the combined NFAP/CCC program to demonstrate the coupling effect. The initial geometry and finite element mesh generated by NFAP is given in Fig. 7. The crack is 0.15 m long and the initial gap-width is 0.89 mm. The web thickness is 8 mm along the crack and 20 mm at the tip. Because of symmetry, only half of the sample was modeled by 80 plane strain elements. The shear relaxation modulus of the propellant was assumed to be

$$G_1(t) = 1.461 + 7.43 * \exp(-.095t) \text{ MPa}; \text{ and } K = 4,826 \text{ MPa.}$$

Calculated pressure distributions at various times, from the CCC alone, are given in Fig. 7. The burning phenomenon of the propellant can be briefly described as follows. The pressure in the chamber increases with time, causing the hot gases to penetrate further into the crack. As time passes, the pressure wave travels along the crack and is reflected from the closed end. At about

200 μ s, the pressure front has already reached the tip and is reflected, causing pressure at the tip to increase.

Figure 8 shows the results obtained from the combined NFAP/CCC program. During the initial period, the general trend of the pressure distribution is similar to that from convective burning analysis alone. However, as time progresses, noticeable differences between the two cases begin to appear. Up to 200 μ s, the pressures obtained from the combined analysis are lower, except near the crack entrance region. At $t = 300 \mu$ s, two pressure peaks appear. At $t = 325 \mu$ s, three pressure peaks appear. These pressure peaks are caused by the partial closure of the gap. The deformation pattern of the propellant is quite irregular because of the uneven distribution of the pressure along the crack surface. The elements at the crack entrance are compressed by the high chamber pressure, which results in the propellant being pushed into the crack. Since chamber pressure increases more quickly than pressure inside the crack, the propellant is pushed toward the lower pressure region inside the crack. The mechanical deformation of the propellant causes narrowing of the crack width, and consequently results in a local crack closure. This local gap closure manifests itself in a pressure peak. The localized pressure peaks or gap closures move along the crack. At $t = 325 \mu$ s, this localized pressure phenomenon becomes evident at $x/L = 0.167, 0.433$, and 0.633 .

CONCLUSION

The computer program for evaluating the coupling effect between convective burning and structural deformation was developed by combining the Crack Combustion Code and a Nonlinear Finite-Element Analysis Program. In structural analysis, the linear viscoelastic material model, together with the capabilities of simulating ablating boundary and interpolating material responses, was considered. Also, the coupling effect estimated by the combined analysis shows some significant interaction between the combustion and mechanical deformation. This phenomenon will be verified further by future experiments.

SYMBOLS

1. Combustion Analysis

- A_p = cross-sectional area of crack
 B_x = body force
 b = co-volume
 c_p = specific heat at constant pressure
 E = total stored energy
 \bar{h}_c = local convective heat-transfer coefficient
 \bar{h}_{cp} = local convective heat-transfer coefficient over propellant surface
 \bar{h}_{cw} = local convective heat-transfer coefficient over nonpropellant port wall
 h_f = enthalpy of combustion gas at adiabatic flame temperature
 P_h = burning perimeter
 P_w = wetted perimeter of port
 p = static pressure
 R = specific gas constant for combustion gases
 r_b = burning rate of solid propellant, including erosive burning contribution
 T = temperature (without subscript, static gas temperature)
 T_f = adiabatic flame temperature of solid propellant
 T_{pi} = initial propellant temperature
 T_{ps} = propellant surface temperature
 T_{ws} = nonpropellant wall surface temperature
 t = time
 u = gas velocity
 v_{gf} = velocity of propellant gas at burning surface
 x = axial distance from propellant crack opening
 y = perpendicular distance from propellant surface into solid
 α = thermal diffusivity

γ = ratio of specific heats
 λ = thermal conductivity
 μ = gas viscosity
 ρ = density (without subscript, gas density)
 τ_w = shear stress on port wall
 τ_{xx} = normal viscous stress
 θ_w = angle measure, in a counterclockwise direction, at lower side of propellant, degree

Subscripts

i = initial value
 pr = solid propellant (condensed phase)
 c = rocket chamber

2. Structural Analysis

s_{ij} = stress deviators
 e_{ij} = strain deviators
 σ_{ij} = stress tensor
 G_1 = shear relaxation modulus
 K = bulk modulus
 $(\)^t$ = a quantity at time t
 $\{\Delta\sigma\}$ = incremental stress
 $\{\Delta\varepsilon\}$ = incremental strain
 $\{\sigma_0\}$ = equivalent initial stress vector due to viscoelastic behavior
 $[K]$ = stiffness matrix
 $[]^T$ = transpose of matrix
 M = number of terms of series in relaxation modulus

$\{g_0\}$ = }
 $\{g_m\}$ = } material constants in relaxation modulus
 $\{\beta_m\}$ = }

$\{\Delta v\}$ = increment of nodal displacement vector

$[D_{VE}]$ = viscoelastic material matrix

$[B]$ = strain-nodal displacement transformation matrix

\bar{w}'_k = values of Gaussian variables at k-th integration point referred to old element

w'_i = values of Gaussian variables at i-th nodal point referred to old element

(r'_k, s'_k) = local coordinates of k-th integration point referred to old element

(y_i, z_i) = global coordinates of i-th nodal point referred to new element

D_i = i-th nodal displacement referred to new element

D'_i = i-th nodal displacement referred to old element

(r', s') = local coordinates of point in equation referred to old element

REFERENCES

1. Taylor, J.W.: The Burning of Secondary Explosive Powders by a Convective Mechanism. *Trans. Farad. Soc.* 58, 1962, p. 561.
2. Belyaev, A.F.; Korotkov, A.I.; Sulimov, A.A.; Sukoyan, M.K.; and Obemin, A.V.: Development of Combustion in an Isolation Pore. *Combustion, Explosion and Shock Waves*, Vol. 5, Jan.-March 1969, pp. 4-9.
3. Belyaev, A.F.; Bobolev, V.K.; Korotkov, A.A.; Sulimov, A.A.; and Chuiko, S.V.: Development of Burning in a Single Pore, Transition of Combustion of Condensed Systems to Detonation, Chap. 5, Pt.A., Science Publisher, 1973, pp. 115-134.
4. Cherepanov, G.P.: Combustion in Narrow Cavities. *J. of Appl. Mech.*, Vol. 11, 1970, pp. 276-281.
5. Godai, T.: Flame Propagation into the Crack of a Solid-Propellant Grain. *AIAA Journal*, Vol. 8, July 1970, pp. 1322-1327.
6. Krasnov, Yu. K.; Margulis, V.M.; Margolin, A.D.; and Pokhil, P.F.: Rate of Penetration of Combustion into the Pores of an Explosive Charge. *Combustion, Explosion, and Shock Waves*, Vol. 6, July-Sept. 1970, pp. 262-265.
7. Jacobs, H.R.; Williams, M.L.; and Tuft, D.B.: An Experimental Study of the Pressure Distribution in Burning Flaws in Solid Propellant Grains. Univ. of Utah, Salt Lake City, Utah, Final Report to Air Force Rocket Propulsion Laboratory, AFRPL-TR-72-108, UTEC DO 72-130, Oct. 1972.
8. Jacobs, H.R.; Hufferd, W.L.; and Williams, M.L.: Further Studies of the Critical Nature of Cracks in Solid Propellant Grains, AFRPL-TR-75-14, March 1975.
9. Lee, E.H.; Radok, J.R.M.; and Woodward, W.B.: Stress Analysis for Linear Viscoelastic Material. *Trans. Soc. Rheol.*, Vol. 3, 1959, pp. 41-59.
10. Arenz, R.J.; and Williams, M.L.: The Stresses in an Elastically Reinforced Pressurized Viscoelastic Sphere with an Eroding Boundary. *Proceedings 20th Meeting Joint Army-Navy-Air Force Physical Properties Panel*, Johns Hopkins Univ., Baltimore, Md., 1961, p. 143.
11. Corneliusen, A.H.; and Lee, E.H.: Stress Distribution Analysis for Linear Viscoelastic Materials. *International Union of Theoretical and Applied Mechanics Symposium on Creep*, 1960, pp. 1-20.
12. Corneliusen, A.H.; Kamowitz, E.F.; Lee, E.H.; and Radok, J.R.M.: Viscoelastic Stress Analysis of a Spinning Hollow Circular Cylinder with an Ablating Pressurized Cavity. *Trans Soc. Rheol.*, Vol. 7, 1963, pp. 357-390.
13. Shinozuka, M.: Stresses in a Linear Incompressible Viscoelastic Cylinder with Moving Inner Boundary. *J. Appl. Mech.*, Vol. 13, 1963, pp. 335-341.
14. Rogers, T.G.; and Lee, E.H.: The Cylinder Problem in Viscoelastic Stress Analysis. *Quart. Appl. Math.*, Vol. 22, 1964, pp. 117-131.

15. Schapery, R.A.: An Approximate Method of Stress Analysis for a Large Class of Problems in Viscoelasticity. *Purdue Univ. Rept. A.* and ES62-18, 1963.
16. Christensen, R.M.; and Schreiner, R.N.: Response to Pressurization of a Viscoelastic Cylinder with an Eroding Internal Boundary, *AIAA Journal*, Vol. 3, 1965, pp. 1451-1455.
17. Chang, T.Y.: Approximate Solutions in Linear Viscoelasticity. Ph.D. Dissertation, Dept. of Civil Eng., Univ. of California, Berkeley, 1966.
18. Zienkiewicz, O.C.; Watson, M.; and King, I.P.: A Numerical Method of Viscoelastic Stress Analysis. *Int. J. Mech. Sci.*, Vol. 10, 1968, pp. 807-827.
19. White, J.L.: Finite Element in Linear Viscoelasticity. *Proceedings of 2nd Conference on Matrix Method in Structural Mechanics*, Airforce Flight Dynamics Lab, Wright Patterson AFB, Ohio, AFFDL-TR-68-150, 1968, pp. 489-516.
20. Gupta, K.K.; and Heer, E.: Viscoelastic Structures. *Structural Mechanics Computer Programs*, Univ. Press of Virginia, Charlottesville, 1974, pp. 207-225.
21. Sankaran, G.V.; and Jana, M.K.: Thermoviscoelastic Analysis of Axisymmetric Solid Propellant Grains. *J. Spacecraft*, Vol. 13, 1976, pp. 641-642.
22. Weeks, G.E.; and Cost, T.L.: An Algorithm for Automatically Tracking Ablating Boundary. *Int. J. Num. Method. Engr.*, Vol. 14, 1979, pp. 441-449.
23. Chang, T.Y.; and Prachuktam, S.: NFAP - A Nonlinear Finite-Element Analysis Program. *Dept. of Civil Engr., Univ. of Akron, Rept. No. SE76-3*, 1976.
24. Kuo, K.K.; Chen, A.T.; and Davis, T.R.: Transient Flame Spreading and Combustion Process Inside a Solid Propellant Crack. *AIAA Paper 77-14*, AIAA 15th Aerospace Science Meeting, Jan. 1977.
25. Goodman, T.R.: Application of Integral Methods to Transient Nonlinear Heat Transfer. *Advances in Heat Transfer*, Vol. 1, Academic Press, New York, 1964, pp. 51-122.
26. Kuo, K.K.; Chen, A.T.; and Davis, T.R.: Convective Burning in Solid-Propellant Cracks. *AIAA Journal*, Vol. 16, June 1978, pp. 600-607.
27. Chang, J.P.: Finite Element Analysis of Linear Viscoelastic Solids. M.S. Thesis, Dept. of Civil Engr., Univ. of Akron, 1980.
28. Herrmann, L.R.: Laplacian-Isoparametric Grid Generation Scheme. *J. of Engr. Mech. Div., Proc. of the ASCE*, Vol. 102, Oct. 1976, pp. 749-756.

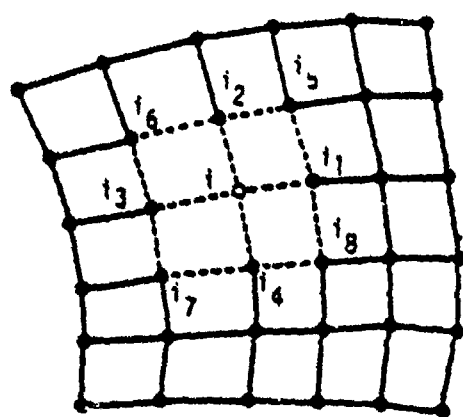


Figure 1.- Neighborhood of node i .

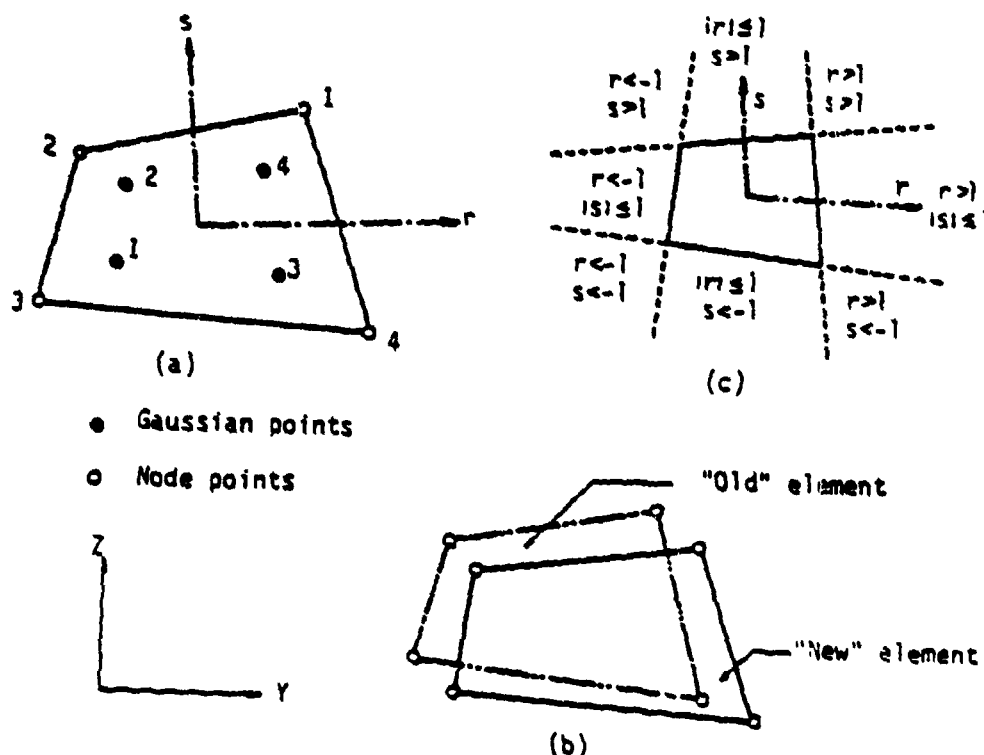


Figure 2.- Interpolation scheme.

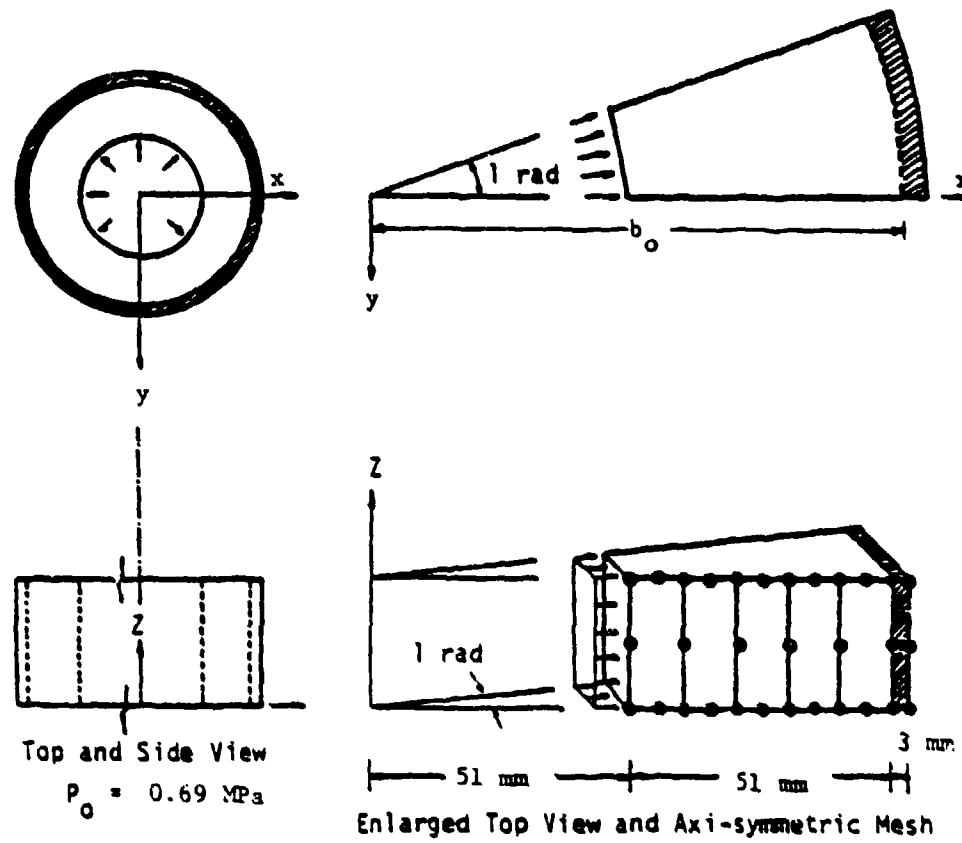


Figure 3.- Finite element mesh of a reinforced thick-walled cylinder.

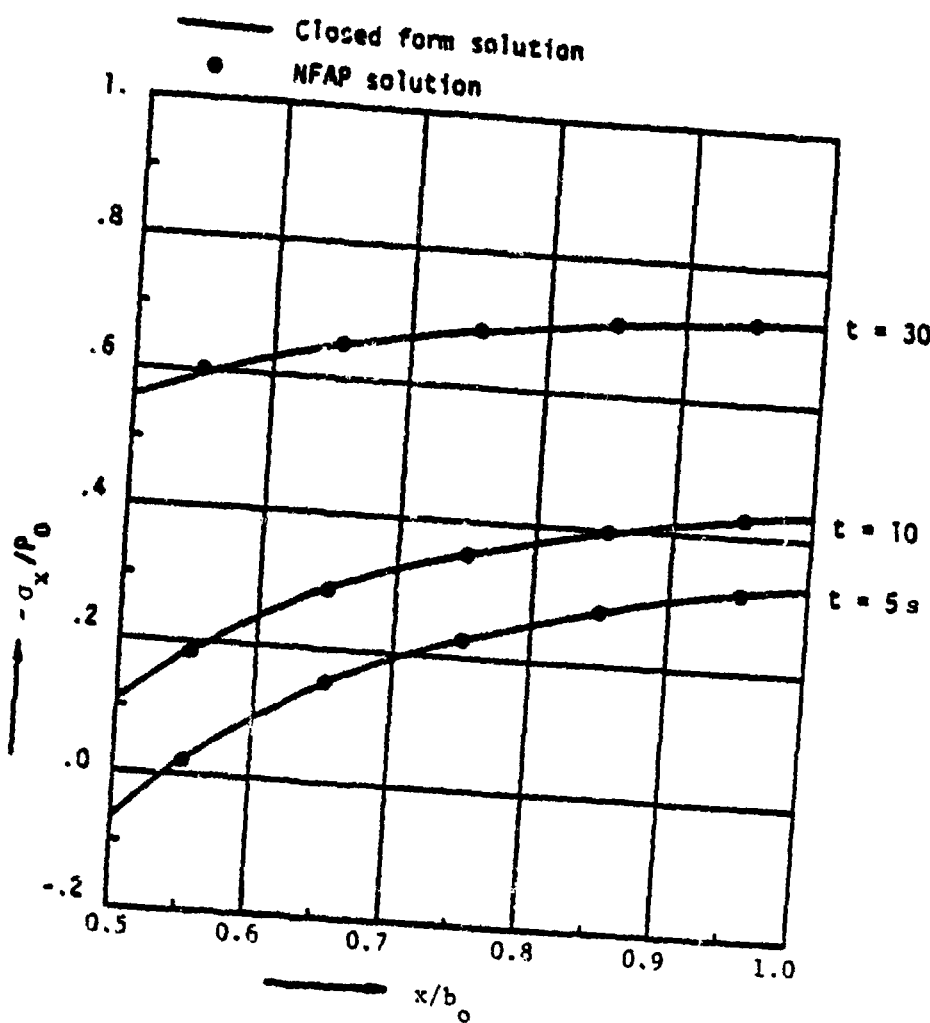


Figure 4.- Reinforced cylinder under internal pressure
variation of hoop stress.

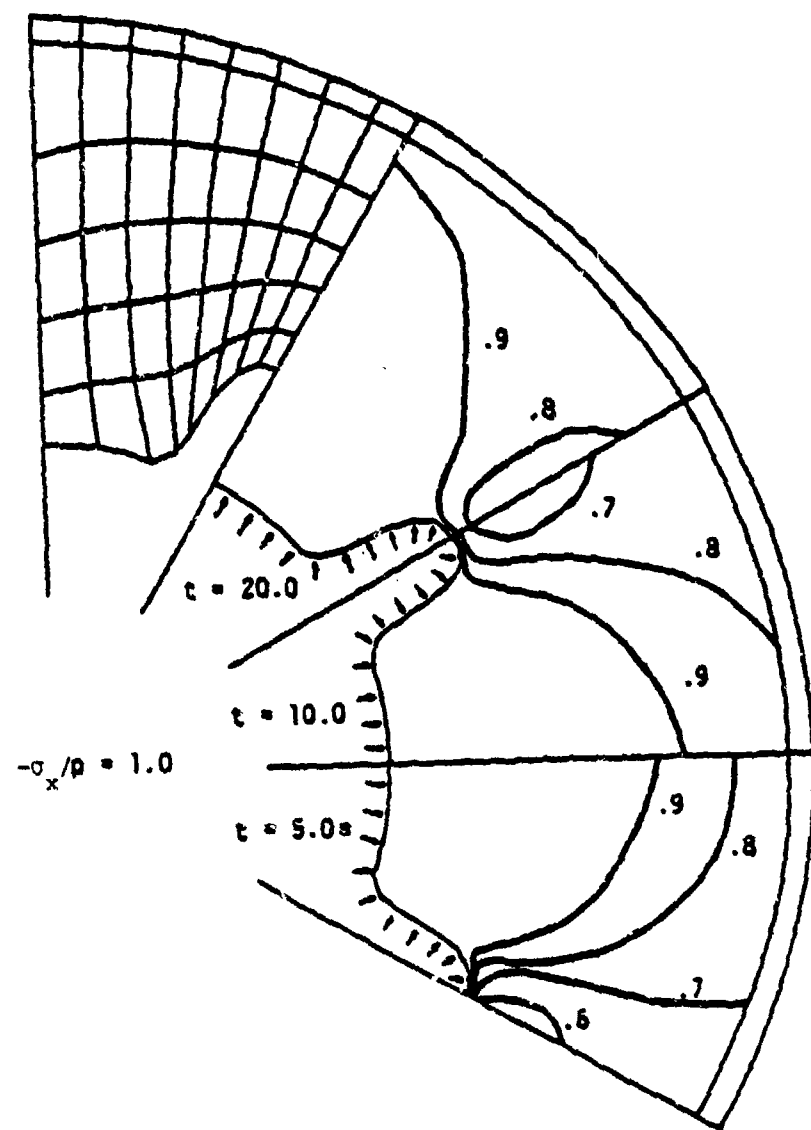


Figure 5.- Finite element mesh and contours of maximum principal stress of a star-shaped rocket motor with fixed boundary.

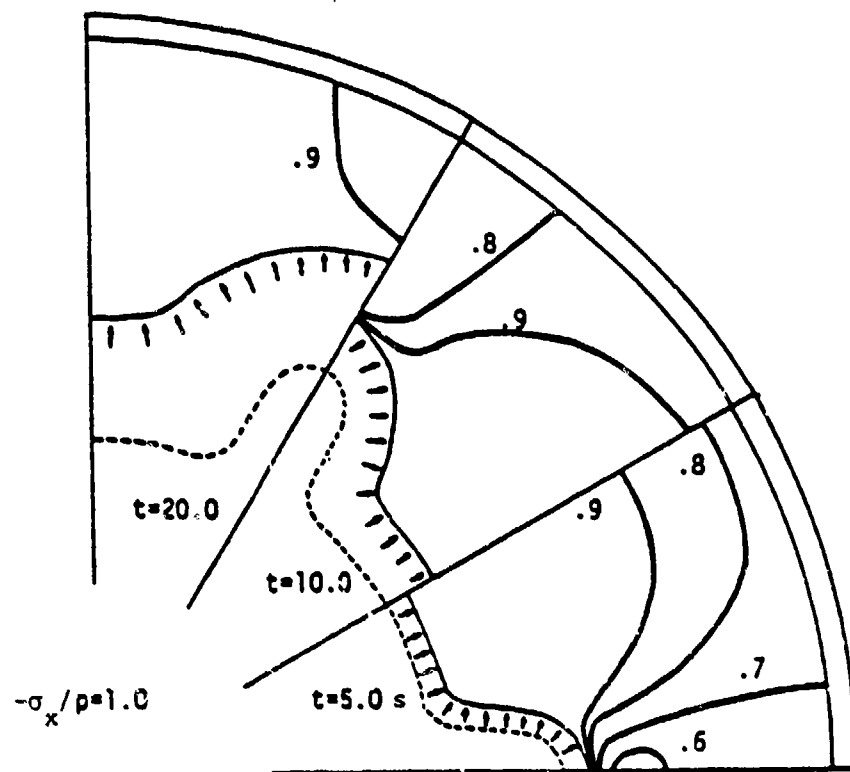


Figure 6.- Contours of maximum principal compressive stress of a star-shaped rocket motor with moving boundary.

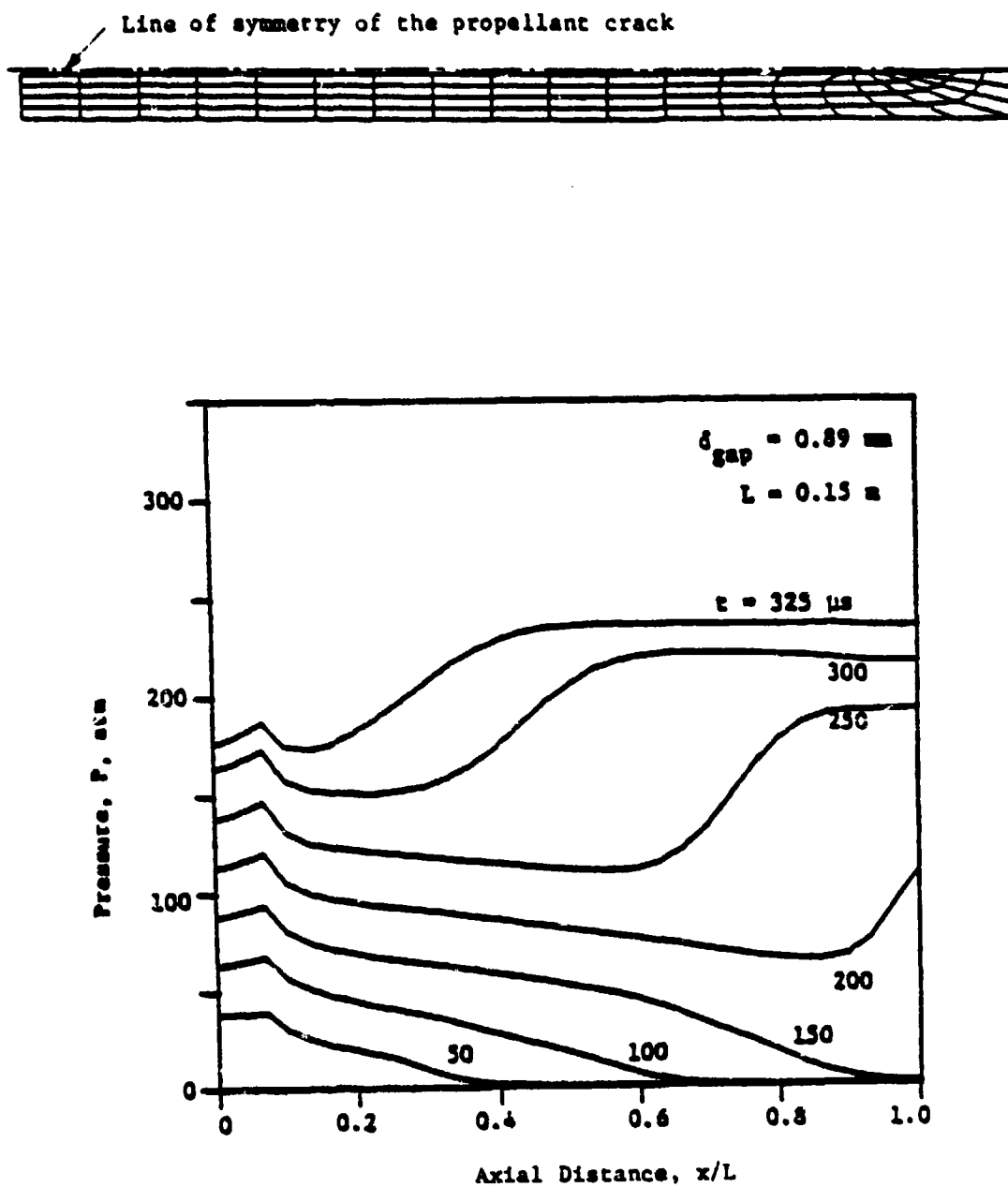


Figure 7.- Finite element mesh of a propellant crack and calculated pressure distributions for various times from the crack combustion code.

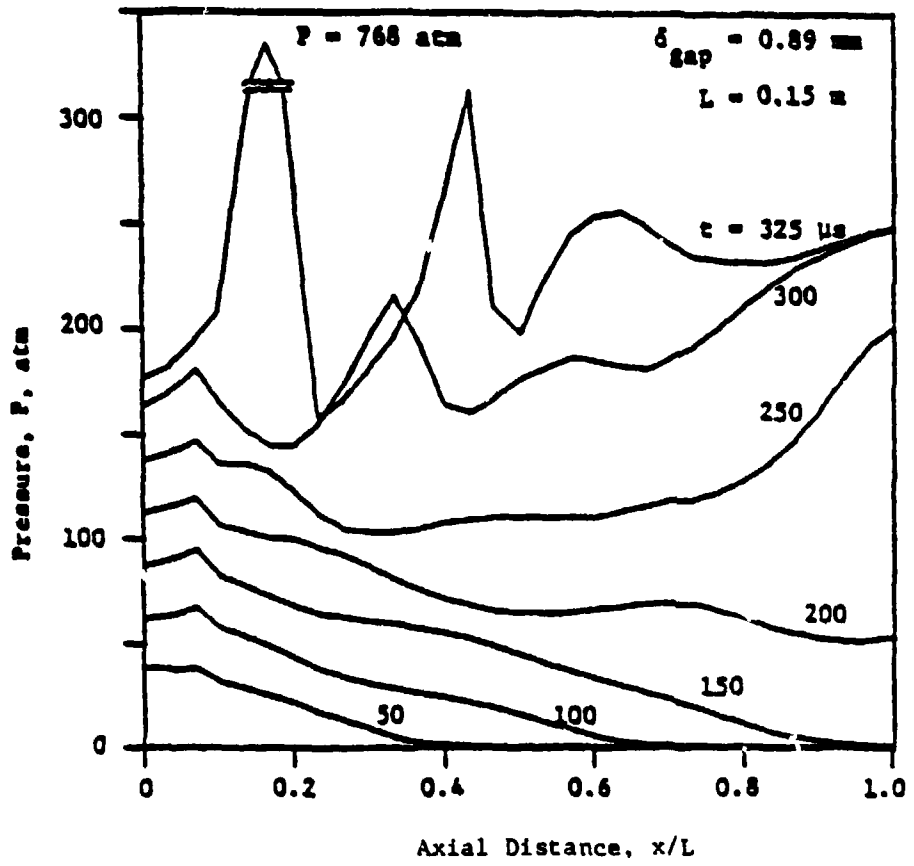


Figure 8.- Calculated pressure distributions for various times from the combined crack combustion and non-linear finite-element analysis program.

APPENDIX B (Ref. No. 4)

EFFECT OF PROPELLANT DEFORMATION ON IGNITION
AND COMBUSTION PROCESSES IN SOLID PROPELLANT CRACKS*

M. Kumar[†] and K. K. Kuo^ξ
 Department of Mechanical Engineering
 The Pennsylvania State University
 University Park, Pennsylvania 16802

ABSTRACT

A comprehensive theoretical model was formulated to study the development of convective burning in a solid propellant crack which continually deforms due to burning and pressure loading. In the theoretical model, the effect of interrelated structural deformation and combustion processes was taken into account by considering a) transient, one-dimensional mass, momentum, and energy conservation equations in the gas phase, b) a transient, one-dimensional heat conduction equation in the solid phase, and c) quasi-static deformation of the two-dimensional, linear viscoelastic propellant crack caused by pressure loading. This set of coupled, nonlinear, partial differential equations was solved numerically. Several regions of partial crack closures were observed experimentally in narrow cracks (~450 μm). Predicted results indicate that the partial closures may generate substantial local pressure peaks along the crack, implying a strong coupling between chamber pressurization, crack combustion, and propellant deformation, especially when the cracks are narrow and the chamber pressurization rates are high. Predicted results for ignition front propagation and pressure distribution are in good agreement with the experimental data. Both theoretical and experimental results indicate that the maximum pressure in the crack cavity is generally higher than that in the chamber. It was found that, under the conditions studied, the initial flame-spreading process is not substantially affected by propellant deformation.

INTRODUCTION

High-energy propellants, which are used to obtain increased specific impulse in rocket motors, generally contain high solids loading of energetic materials, e.g., cyclotetramethylenetrinitramine (HMX). As the density of solids in the propellant is increased, the probability that cracks and flaws will develop in the propellant grain is also increased. Defects in propellant grains can originate during manufacture, storage, or handling, during ignition and combustion, or during loading of different segments of a segmented rocket.

The extent to which cracks can reduce the reliability of solid rocket motors has been a major concern in the development of high-energy propellant

*This work represents a part of the results obtained under the contract N00014-79-C-0762 sponsored by the Power Program, Office of Naval Research, Arlington, Virginia. The support of Dr. Richard S. Miller is appreciated.

[†]Assistant Professor

^ξAssociate Professor

grains. It is known that cracks in solid propellant grain can allow hot, high-pressure gases to penetrate the cavity, thereby providing additional surface area for combustion. The phenomenon of such a rapid flame propagation into a propellant cavity and the subsequent rapid regression is called convective burning. The convective burning rate often exceeds the normal (conductive) burning rate. Mechanical deformation and crack propagation may result when combustion processes inside the crack produce much higher pressure than the designed maximum pressure. If the local pressure rise due to the gasification is sufficiently rapid, it may produce strong compression waves, or even shock waves, which can initiate detonation. The generally understood mechanism of transition from deflagration to detonation (DDT) is given in Ref. 1. DDT is more likely to occur in gas-permeable propellants, such as granular propellant beds or propellant grains with flaws or cracks, which have large burning surface areas. Even if the convective burning rate does lead to catastrophic failure, the combustion inside the propellant crack can cause the performance of a rocket motor to deviate significantly from expectations.

Convective burning inside a crack is complicated because it involves several interdependent processes such as a) pressure wave phenomenon, b) convective heating of the propellant crack surface and subsequent flame propagation along the crack, c) pressurization of the crack cavity due to burning, which may result in flow reversal when the pressure inside the crack exceeds that of the chamber, d) change in the crack geometry due to burning, as well as mechanical deformation caused by pressure loading, and e) propagation of the crack due to regression and mechanical fracture. Parameters which may significantly affect the combustion process are: chamber pressure and pressurization rate, geometry of the crack, erosive burning effects due to high gas velocities, physicochemical properties of the propellant, composition of the igniter gas, and initial and boundary conditions.

This paper deals with the formulation of a comprehensive theoretical model, which includes the effect of propellant deformation to predict flame spreading and combustion processes during the development of convective burning in solid propellant cracks. Predicted results are also compared with some of the experimental investigations^{2,3} conducted by the authors for model validation.

As mentioned earlier, convective flame propagation and subsequent crack propagation/branching may lead to anomalous burning or even DDT. Since the propellant is deformable, burning inside a solid propellant crack is basically a coupled solid mechanics and combustion phenomenon. The combustion phenomenon inside the crack is strongly influenced by the crack geometry. The geometry, or gap-width, can be altered for the following two reasons:

1. Mass loss due to gasification or ignition of the propellant surface along the crack during the combustion process, leading to a variation in the geometry.
2. Mechanical deformation of the propellant crack due to a) pressure loading on the interior surface of the crack, b) pressure force of the combustion chamber acting on the propellant grain near the crack entrance, and c) stresses in the propellant,

caused by temperature gradients in the grain, which may also cause changes in the crack geometry.

Both burning rate and the mechanical deformation are governed by pressure acting on the crack surfaces. On the other hand, a change in gap width or geometry will cause pressure distribution to vary. Pressure distribution will strongly influence deformations along the crack and stress concentration at the crack tip. It is obvious, therefore, that pressure and crack geometry are strongly interdependent in a burning solid propellant crack.

Convective burning inside a solid propellant crack has been a subject of interest in recent years. An extensive literature review in this area was recently conducted by Bradley and Boggs.⁴ Belyaev et al.⁵ have compiled most of the recent Russian work on convective burning and DDT. Both theoretical and experimental studies in the area of crack combustion have been conducted at The Pennsylvania State University.⁶⁻¹⁰ Convective burning studies can be subdivided into two broad categories: a) onset of convective burning, and b) development of convective burning. This study is restricted to the development of convective burning in isolated propellant cracks. The following paragraphs list some of the important research conducted in this area.

Experimental and theoretical studies on the development of convective burning are limited. Belyaev et al.^{11,12} made preliminary experimental investigations of the development of combustion in single pores. Kuo et al.⁶ developed a detailed theoretical model for predicting the development of convective burning in isolated propellant cracks. However, this model⁶ does not include the mechanical deformation of the crack during the development of convective burning. Kim¹³ studied the possibility of shock to detonation transition in propellant cracks using the model of Kuc et al.⁶ and an extremely simplified, one-dimensional, elastic model for propellant deformation. Pilcher¹⁴ has also reported some computations conducted on a deformable crack, but has given no details.

High pressures present in the crack during the development of convective burning, as well as associated mechanical deformation and stress concentrations, may lead to crack propagation. Most of the earlier work in the area of crack propagation was done in the USSR.¹⁵⁻¹⁷ Kiraanova and Leipunskii¹⁵ examined the mechanical stability of propellant cracks, using steady-state approximations. Only continuity and momentum equations were considered in the gas phase. The erosive burning effects were ignored. The material was assumed to be elasto-brittle, and stress intensity was used to determine the initiation of crack propagation. The stable crack length obtained from their simplified model was a function of the crack length, chamber pressure, burning rate, gas enthalpy, stress intensity factor, and propellant density. The autostabilization condition for the unstable burning crack was also obtained.

A greatly improved analytical model for the same problem was formulated by Cherepanov.¹⁶ He stated that if the cavity was sufficiently long and narrow, the pressures in the crack would reach a high value and render the system unstable. Even though his gas-phase equations contained nonsteady terms, several important terms were ignored. The propellant material was

assumed to be elasto-plastic, and the deformation process to be quasistatic. However, Cherepanov did not solve the governing set of equations and, therefore, did not present any results. He obtained a sufficient condition for the stability of a steady-state problem.

Belyaev et al.¹⁷ proposed modifications to the Kirsanova and Leipunskii¹⁵ model and pointed out some of its limitations. It was noted that an elasto-brittle material model cannot describe the visco-elastic character, which is typical of solid propellants. They made maximum pressure measurements in the crack, and accordingly changed the empirical correlation for maximum pressure in the cavity. The maximum pressure in the crack was a function of chamber pressure and the ratio of crack length to half-width. They proposed that, depending upon the chamber pressure and crack geometry, the stability of the crack can be subdivided into four regions: a) a region of absolute mechanical stability; b) a region of practical stability; c) a region of bounded growth; and d) a region of self-sustained growth.

Jacobs et al.¹⁸⁻²⁰ studied the critical nature of cracks and debonds, assuming a quasi-steady model. The propellant was considered to be linear viscoelastic. They also measured the pressure distribution along the crack surface under the condition of instantaneous ignition over the entire surface.¹⁹ The gas dynamics equations of Jacobs et al. are inadequate because they include numerous simplifications and assumptions. Other related studies on crack combustion have been reported.²¹⁻²³ Takata and Wiedermann^{22,23} have been investigating the initiation of detonation in a propellant crack by introducing the effect of stress wave interaction with the crack boundary, and assuming a foam layer to be present on the propellant surface during combustion. The propellant is considered to be linear, isotropic, elastic material which does not yield or fail.

Numerous studies, based purely on solid mechanics considerations,²⁴⁻³⁹ have been conducted on crack propagation. All are based on quasi-static crack propagation in viscoelastic material and use the concept of local energy dissipation at the crack tip. Work on dynamic crack propagation is currently underway, with Swanson⁴⁰ reporting some progress in this area. However, there is at present no theoretical model capable of realistically predicting stress concentrations at the tip of a burning crack, which is a necessary input for all crack propagation theories.

It is apparent that a theoretical model is needed to predict the development of convective burning, while also taking into account the effect of mechanical deformation. Such a model would also be extremely useful in making realistic predictions of crack propagation; at present, these predictions are based purely on solid mechanics considerations. Even though this investigation will not attempt to study crack propagation caused by mechanical fracture at the tip, the analysis and program developed here can be extended easily for such a study.

The specific objectives of this study are:

1. To develop a theoretical model to study ignition, flame spreading and convective burning in a solid propellant crack which continually deforms due to burning and pressure loading.

2. To study the effects of such parameters as chamber pressurization rate, dP/dt , and crack gap width on the flame spreading and combustion process in propellant cracks.
3. To test the validity of the theoretical model by comparing the predicted results with the experimental data.

Actual propellant defects may consist of several irregularly branched cracks. However, because of the complexity of physical processes involved in the study of combustion in propellant cracks, and for mathematical tractability, this investigation is limited to a single isolated crack.

ANALYSIS

DESCRIPTION OF PHYSICAL MODEL

A schematic diagram of the physical model chosen to simulate a propellant crack is shown in Fig. 1. The location of the crack is normal to the

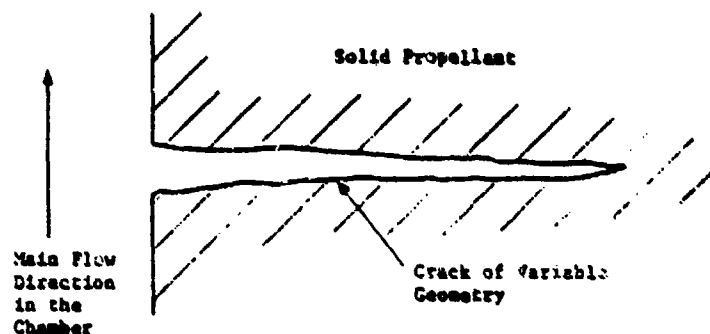


Figure 1 Schematic Diagram of the Physical Model

main flow direction in the combustion chamber or in a rocket motor. The current analysis is applicable to a crack of variable geometry. However, in order to closely simulate the assumptions of the physical model, and for ease of manufacturing a reproducible propellant crack, specimens used in the experimental study were of uniform rectangular cross-section. A schematic diagram of the propellant crack geometry used in the experimental investigation is shown in Fig. 2.

As the hot combustion gases flow through the main chamber, a portion of the gases is driven into the crack because of the pressure gradient. And as the hot gases flow over the propellant crack, energy is transferred from the gas to the propellant. The rate of heat transfer to the propellant depends upon the local temperature, velocity, and density of the gas, and the temperature of the propellant surface. The heat transfer may cause the

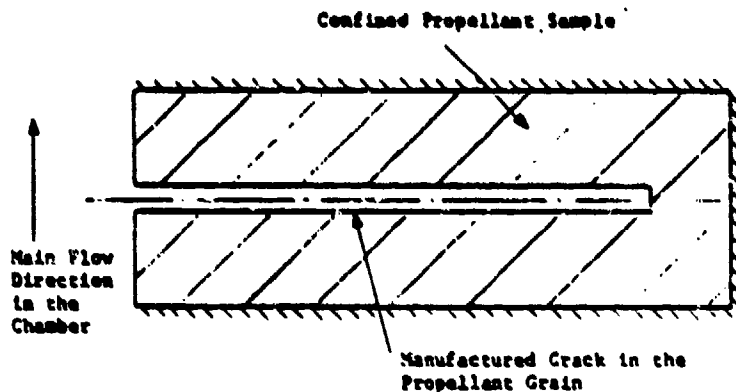


Figure 2 Schematic Diagram of Cracks Used in Experiments

propellant to ignite. As additional gases are driven into the crack, the density and velocity increase further, resulting in a faster flame propagation along the crack. As the ignition front moves downstream, more hot gases are generated by combustion of the propellant surface, causing local pressure to increase. At the same time, the deformation of the propellant will also alter the pressure. The net result of these two opposing and interdependent phenomena determines the local pressure.

BASIC ASSUMPTIONS

The following basic assumptions are made in the derivation of the theoretical model:

1. The gas-phase reaction zone is considered quasi-steady. In other words, the relaxation time associated with the flame is much shorter than that associated with transient pressure variation; therefore, the flame adjusts itself immediately to chamber conditions.
2. The deformation of the propellant is quasi-steady, that is, the mechanical deformation of the propellant can be obtained by using a static analysis.
3. All chemical reactions occur near the propellant surface in a very thin planar zone, and the distance of the combustion zone from the propellant surface is small when compared to the crack gap width.
4. The bulk flow of the gases in the pores is considered to be one-dimensional.
5. The gases present in the propellant crack obey the Noble-Abel gas law.

6. The propellant surface temperature is uniform, and the thermal properties of the propellant are constant.

7. The propellant can be represented by a linear viscoelastic material model; the material is assumed to be isothermal, homogeneous and isotropic. The propellant grain is two-dimensional, with no mechanical fracture at the crack tip.

The validity of assumptions 1 and 2 can be shown by comparing the characteristic times associated with pressure variation, gaseous flame zone, and compression wave propagation through the propellant grain. In the crack combustion experiments, the typical time associated with the pressure excursion, τ_g , is in the order of 1 ms. The other characteristic times are evaluated as follows:

$$\frac{\tau_g}{\tau_s} = \frac{a/v_{gf}^2}{a_{pr}/r_b^2} = \frac{\lambda \rho c_{pr}}{\lambda_{pr} \rho_{pr} c_p} \quad (1)$$

where τ_s is the characteristic time associated with the solid phase, and is given by

$$\tau_s = a_{pr}/r_b^2 = 0 \text{ (1 ms)} \quad (2)$$

Since $(\lambda c_{pr})/(\lambda_{pr} c_p) = 0(1)$, and $(\rho/\rho_{pr}) = 0(.01)$, we get $\tau_g = 0(.01 \text{ ms})$.

The time associated with the stress waves in the solid is

$$\begin{aligned} \tau_v &= \frac{\text{web thickness}}{\text{stress wave propagation speed}} = \frac{0(.01 \text{ m})}{0(\sqrt{K/\rho})} = \frac{0(.01 \text{ m})}{0(2000 \text{ m/s})} \\ &= 0(5 \mu\text{s}) \end{aligned} \quad (3)$$

Since τ_g and τ_v are both $\ll \tau_p$, the quasi-steady assumption of the flame zone and mechanical deformation are valid. The value of τ_v calculated from the shear modulus will be an order of magnitude higher; however, it will still be smaller than τ_p . Assumption 3 is reasonable for AP-based composite solid propellants in the pressure range of interest. Even though the heat release zone is distributed, the diffusion flame stand-off distance is usually in the order of 50 μm , and is small in comparison to the gap width (gap widths are in the order of 500 μm in the present experimental investigation).

Assumption 4 is well justified for the crack dimensions used in this investigation. The crack length to hydraulic diameter ratio was approximately 100. The dense gas relation (assumption 5) can adequately describe the departure from the ideal gas law at high pressures. Assumption 6, employed for mathematical simplicity, allows the use of a one-dimensional transient heat conduction equation for the solid. Since the thermal wave penetration depth is of the same order of magnitude as the oxidizer particle size of the propellant, the actual heat transfer process is three-dimensional.

However, researchers in the field have not yet investigated the three-dimensional treatment of the heat conduction process in composite solid propellants because of the complexities associated with the three-dimensional structure of oxidizer crystals and fuel binder, and the fact that numerical solutions are cumbersome and time consuming.

Most of the solid propellants can be well characterized by a viscoelastic material model.²⁴⁻⁴⁰ For simplicity, the viscoelastic material model was assumed to be linear. Even though the assumption of isothermal condition for material response is not strictly accurate, it is a good approximation, since the thermal wave penetration depth is less than 100 μm . Fracture of the propellant at the crack tip was considered beyond the scope of the present investigation, since it is a vast subject area in itself. The viscoelastic nature of the material, i.e., the time dependence of the relaxation modulus, may not be very significant during the period of experimental test firings of this study because the stress relaxation time is much greater than the transient pressure variation time. Indeed, the analysis and model developed here are applicable to a wide variety of operating conditions and are not simply limited to the experimental test conditions of this study.

In this analysis, ignition is defined as the attainment of a critical temperature at the propellant surface. It is assumed that no solid or gas-phase reaction takes place before onset of ignition. The tacit assumption is made here that there is little time between the attainment of a critical surface temperature and the reaction between the fuel and the oxidizer species to cause ignition.

CONSERVATION EQUATIONS

To formulate the theoretical model, we first write the unsteady, variable area, one-dimensional gas-phase conservation equations for reacting compressible fluid flow. The conservation equations are:

Mass Conservation:

$$\frac{\partial(\rho A_p)}{\partial t} + \frac{\partial(\rho u A_p)}{\partial x} = r_b \rho_{pr} P_b \quad (4)$$

Momentum Conservation:

$$\begin{aligned} \frac{\partial}{\partial t} (\rho u A_p) + \frac{\partial}{\partial x} (\rho A_p u^2) &= - A_p \frac{\partial P}{\partial x} + \frac{\partial}{\partial x} (\overline{A_p} \vec{F}_{xx}) \\ &- P_w \tau_w \cos \theta_w + \rho A_p B_x - (\rho_{pr} r_b P_b) v_{gf} \sin \theta_w \end{aligned} \quad (5)$$

Energy Conservation:

$$\begin{aligned}
 \frac{\partial}{\partial t} (\rho A_p E) + \frac{\partial}{\partial x} (\rho A_p u E) = & \cancel{\frac{\partial}{\partial x} (\rho A_p \frac{\partial T}{\partial x})} - \frac{\partial}{\partial x} (A_p P u) \\
 & + \cancel{\frac{\partial}{\partial x} (\rho_{xx} A_p u)} + \rho_{pr} r_b \rho_b h_f \\
 & - \bar{h}_{cp} \rho_b (T - T_{ps}) + B_x \rho A_p u \\
 & - \bar{h}_{cw} (P_w - P_b) (T - T_{ws})
 \end{aligned} \tag{6}$$

An order of magnitude analysis was made; the terms crossed with arrows in Eqs. (5) and (6) were found to be much smaller than the others, and hence were dropped.

Equation of state for the gas-phase:

$$P(\frac{1}{\rho} - b) = RT \tag{7}$$

Equation for stress equilibrium in the solid-phase (neglecting body force):

$$\frac{\partial \sigma_{ij}}{\partial x_j} = 0 \tag{8}$$

Constitutive law for linear viscoelastic material:

$$\begin{aligned}
 \sigma_{ij}(t) = & \int_{-\infty}^t G_1(t-\tau) \frac{d}{d\tau} \epsilon_{ij}(\tau) d\tau \\
 & - \frac{1}{3} \delta_{ij} \int_{-\infty}^t G_1(t-\tau) \frac{d\epsilon_{kk}}{d\tau} d\tau + \delta_{ij} K \epsilon_{kk}
 \end{aligned} \tag{9}$$

The transient heat conduction equation for the solid-phase, before ignition:

$$\frac{\partial T_{pr}}{\partial t} = \alpha_{pr} \frac{\partial^2 T_{pr}}{\partial y^2} \tag{10}$$

The initial and boundary conditions for Eq. (10) are:

$$T_{pr}(0, y) = T_{pi} \tag{11}$$

$$T_{pr}(t, \infty) = T_{pi} \quad (12)$$

$$\frac{\partial T_{pr}}{\partial y}(t, 0) = -\frac{\bar{h}_c(t)}{\lambda_{pr}} [T(t) - T_{ps}(t)] \quad (13)$$

After rearranging the gas-phase conservation equations and making some simplifications, velocity-variation, temperature-variation, and pressure-variation equations were obtained. These equations were found to be totally hyperbolic in nature.⁴¹

The gas-phase and solid-phase equations were solved separately; this is justified because of the quasi-steady assumption. Details of numerical scheme for solving the gasdynamics equations and the solid mechanics equations are given in a later section.

INITIAL AND BOUNDARY CONDITIONS

Initial and boundary conditions must be specified in order to complete the theoretical formulation. The three initial conditions necessary for the solution were specified as

$$u(0, x) = u_i \quad (14)$$

$$T(0, x) = T_i \quad (15)$$

$$P(0, x) = P_i \quad (16)$$

The number of physical boundary conditions that can be specified depends upon the flow conditions at the opening of the crack. When the gases flow into the crack at a subsonic speed, the boundary conditions are

$$P(t, 0) = P_c(t) \quad (17)$$

$$T(t, 0) = T_c(t) \quad (18)$$

$$u(t, x_L) = 0 \quad (19)$$

When the gases flow out of the crack, and the outflow is subsonic, only one boundary condition can be specified at the crack opening. The boundary conditions are given as

$$P(t, 0) = P_c(t) \quad (20)$$

$$u(t, x_L) = 0 \quad (21)$$

When the gas flowing out of the crack is supersonic, no boundary condition can be specified at the crack entrance. In such a case, the only specified boundary condition is

$$u(t, x_L) = 0 \quad (22)$$

For turbulent flow, the final expression for h_c is

$$\bar{h}_c = 0.0346 \text{ Fr}^{-0.6} c_p (\rho_u / R)^{0.8} V_k^{0.2} T_{af}^{-0.67} (x d_h)^{-0.1} \quad (24)$$

Before local ignition, $\bar{h}_c = \bar{h}_{\text{cw}} = \bar{h}$; after local ignition, $\bar{h}_c = 0$. The Prandtl number in Eq. (24) is calculated from Sveala's equation:⁴⁴

$$\text{Pr} = \frac{\gamma}{1.77\gamma - 0.45} \quad (25)$$

The correlation for the friction coefficient for turbulent flow used in this study is

$$c_f = \frac{0.4491 (d_h/x)^{0.1}}{\left\{ \ln \left[\frac{\epsilon_s/d_h}{3.7} + \frac{1.46 R V_k T_{af}^{1.65} (d_h/x)^{0.05}}{P u d_h c_f^{0.5}} \right] \right\}^2} \quad (26)$$

where ϵ_s/d_h is the relative equivalent sand roughness. This expression is actually a modified form of the well-known Colebrook formula^{47,48} for turbulent flow in pipes with roughness. Entrance effects are taken into account by modifying the friction coefficient by a power function of the distance-to-diameter ratio (the original Colebrook expression was obtained for $x/d_h > 20$). Additionally, Eq. (26) implicitly accounts for the temperature dependence of the gas density and viscosity, each evaluated at the average film temperature, T_{af} . After the propellant surface begins to burn locally, the value of the friction coefficient is set at zero, due to the attenuation of wall shear stress caused by surface blowing.

The burning-rate expression is obtained from the strand burning rate data and is given by

$$r_b = a P^n \quad (27)$$

The effect of erosive burning is taken into account by using either the erosive-burning augmentation factor obtained by Razdan and Kuo,^{49,50}

$$r_b = a P^n [1 + K(P) P(u)^n u^n] \quad (28)$$

or the Lenoir-Robillard burning-rate formula,⁵¹

$$r_b = a P^n + K_e \bar{h}_c \exp(-\beta r_b \nu_{pr} / u \nu) \quad (29)$$

NUMERICAL SCHEME FOR GASDYNAMICS EQUATIONS

An implicit finite difference scheme is used to solve the nonlinear coupled partial differential equations. A central difference method was used for the derivatives. The predictor-corrector method was used to handle the non-linear nature of the governing equations. A quasilinearization method was used to linearize the inhomogeneous terms of the governing

equations. The set of finite difference equations thus obtained is solved simultaneously, using a block tridiagonal matrix inversion method.

Six boundary conditions are required when the central difference method is used for spacewise derivatives. This is the case because the difference equations for the first-order spatial derivative obtained by using this method correspond essentially to the second-order partial differential equation.⁵² The extraneous boundary conditions needed for the solution of the finite difference equations are derived from the compatibility relationships at the boundaries. These relationships were obtained by transforming the governing hyperbolic equations into their characteristic form. The equations determining the extraneous boundary conditions are all first-order, ordinary differential equations. They are simultaneously integrated, using a fourth-order Runge-Kutta integration technique.

The extraneous boundary conditions used are as follows. When the gas flows into the crack, in addition to the physical boundary conditions (17) to (19), the three extraneous boundary conditions required are velocity at the crack entrance, and pressure and temperature at the crack tip. When the gas flows out of the crack subsonically, the four extraneous boundary conditions necessary are pressure and velocity at the crack entrance, and pressure and temperature at the crack tip. When the gas flows out of the crack supersonically, the five extraneous boundary conditions needed are pressure, temperature and velocity at the crack entrance, and pressure and temperature at the crack tip.

NUMERICAL SCHEME FOR SOLID-PHASE HEAT EQUATION

The governing partial differential equation for the solid phase, Eq. (10), was solved by using an implicit finite difference technique with a variable mesh system. The variable grid spacing provides finer grid spacing near the surface. The central-difference method was used to approximate both time and spatial derivatives. The resulting set of simultaneous algebraic equations was solved by using a standard tridiagonal matrix inversion method.

NUMERICAL SCHEME FOR STRUCTURAL ANALYSIS

Mechanical deformation of the propellant was obtained by using a general purpose structural analysis program which is called the Nonlinear Finite-Element Analysis Program (NFAP).⁵³ This is an extended version of the Non-linear Structural Analysis Program (NONSAP).^{54,55} Since NONSAP is well-documented and easily accessible, details of the numerical procedure used in NONSAP will not be repeated here. NFAP was modified and consolidated to suit the needs of the present study, and for computational storage efficiency. Three major features added to the numerical formulations are: 1) modeling of the viscoelastic material behavior, 2) simulation of the ablating boundary, and 3) treatment of the material response by an interpolation scheme. Details of this formulation can be found elsewhere.^{8, 56}

To test the numerical procedure developed in this section, the modified version of NFAP was used to compute several viscoelastic problems for which exact solutions are known. The agreement between the NFAP solution and the exact solution is excellent. Details of these comparisons are given in Ref. 56.

The extraneous boundary conditions needed to solve the equations are obtained by using the characteristic equations.⁴¹

A schematic diagram of the boundary conditions for two-dimensional structural analysis is shown in Fig. 3. Because of the symmetry of the crack specimens (see Fig. 2), only half of the crack is considered. All surfaces of the propellant are either pressure-loaded or have fixed boundaries. The propellant surface exposed to the chamber experiences the chamber pressure, $P_c(t)$, whereas the surface along the crack experiences the local pressure along the crack, $P(t,x)$. Due to the symmetry along the center line of the crack, the propellant boundary at the tip is allowed to have deformations only along the axial direction. Along the surfaces of the propellant in contact with the brass mold, the boundaries are assumed to be fixed.

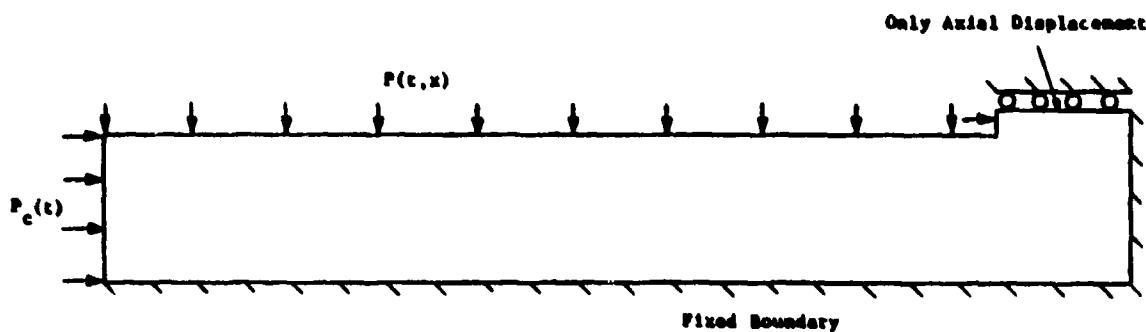


Figure 3 Boundary Conditions for a Test Specimen

EMPIRICAL CORRELATIONS

To close the system of governing equations, empirical correlations are needed for the heat transfer coefficient, drag coefficient, and burning-rate law. The units of the variables in the following correlation are in cgs system, and the units of pressure are in gf/cm².

The correlation for the local convective heat transfer coefficient, \bar{h}_c , is deduced from the Dittus-Boelter correlation for flow in a pipe. The effect of the entrance region is taken into account by using a power function of length to hydraulic diameter ratio.^{42,43} The gas properties are evaluated at an average film temperature, T_{af} , to take into account the variation of the physical properties of the gas across the boundary layer. The dependence of viscosity on temperature was included, using Svehla's expression⁴⁴ for viscosity of air at high temperature. Bartz⁴⁵ has shown good comparisons between Svehla's equation and the published NBS data.⁴⁶ Svehla's expression for viscosity is

$$\mu = v_k T^{0.65} \quad (23)$$

$$\text{where } v_k = 8.699 \times 10^{-7} M_w^{0.5}$$

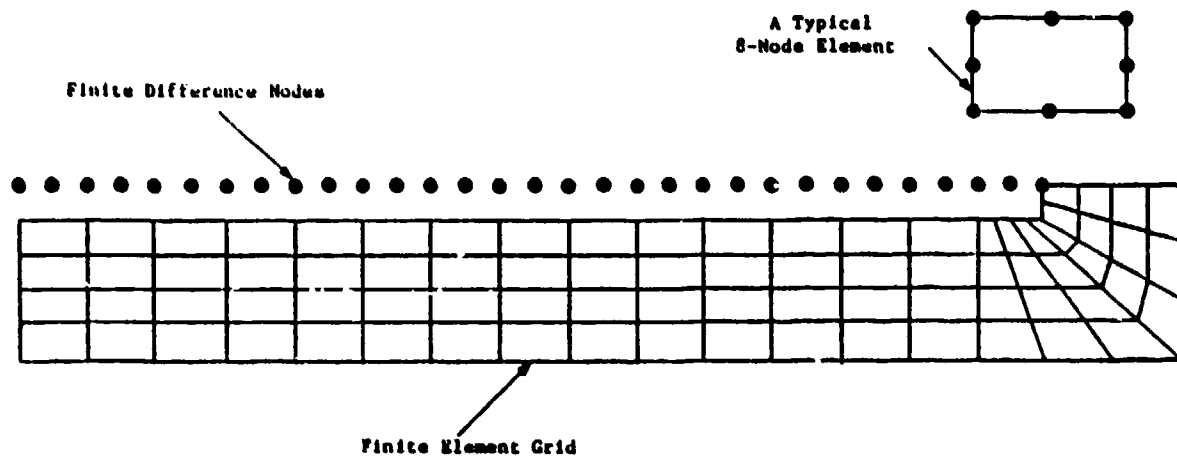


Figure 4 Finite Element Grid and Finite Difference Nodes

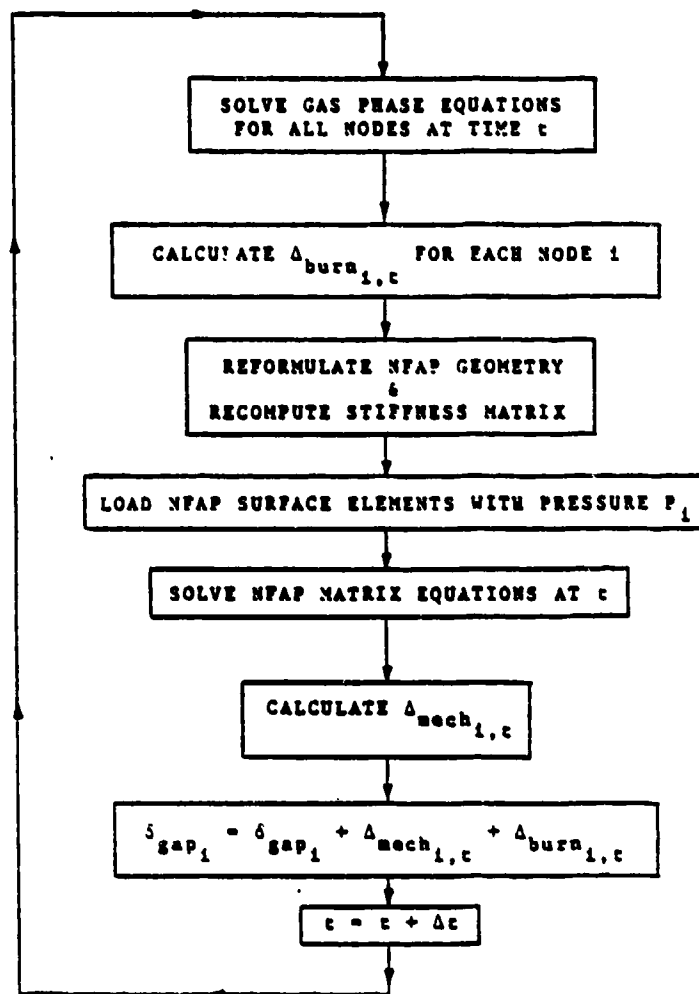


Figure 5 General Layout of the Computer Program

NUMERICAL PROCEDURE

Of the several interdependent gasdynamic and solid mechanics processes that may influence combustion behavior in a propellant crack, the coupling between the pressure along the crack and the structural deformation was considered to be the most important. Other coupled processes, such as thermal stresses due to the temperature gradient in the solid, variation in burning rate due to compression of the propellant, etc., were considered to be of secondary importance and were ignored in the present analysis.

The general layout of the numerical procedure is shown in Fig. 4. Pressure is calculated by the gasdynamic portion of the computer program at each nodal point on a one-dimensional grid along the length of the crack. The convective burning analysis of the crack combustion incorporates the crack geometry variation caused by both mechanical deformation and mass loss through gasification of the propellant surface. Once the gas-phase equations are solved, and pressures and burning rates along the crack are calculated for a particular time t , program control is transferred to the structural analysis (NFAP) portion of the combined program. NFAP reformulates the geometry because of the material loss, and updates the stiffness matrix for the new time step. Surface elements of the finite-element mesh are loaded with the pressure obtained through the gas-phase equations. The propellant deformation is calculated in NFAP using a static analysis at time t . The general stress-strain equations are solved using a plane-strain analysis; this is congruous to the experimental test configuration. The transient nature of the pressure loading is considered by using a static analysis at incremental time steps.

Figure 5 is a diagram of the finite element grids used for the structure analysis and the finite-difference nodes used for the gas-phase solutions. The configuration is compatible with the geometry considered in the theoretical model as well as with that used in the experiments. Two-dimensional, eight-node, isoparametric, quadrilateral elements were used to model a sample crack. Because of symmetry, only half of the crack needs to be considered. Of the eight nodes in an element, four are located at the corners, and one at the midpoint of each side. Except near the tip region, the finite-difference nodes used for the gas-phase solution are in a one-to-one correspondence with the finite-element nodes which form the propellant surface in the two-dimensional structural analysis mesh. This is helpful in reducing the computational effort in transferring the values from the finite-difference nodes to the finite-element grids, and vice versa.

RESULTS AND DISCUSSION

EXPERIMENTAL RESULTS

Figure 6 shows a schematic diagram of the test configuration used for detailed observation of the flame front. The crack is formed between a propellant slab and an inert, transparent plexiglass window; the crack is perpendicular to the direction of flow in the main chamber. This type of configuration provides direct (front view) observation of the ignition front propagation and burning propellant surface, even for very narrow cracks. Most of the experimental results were obtained with cracks formed by cutting

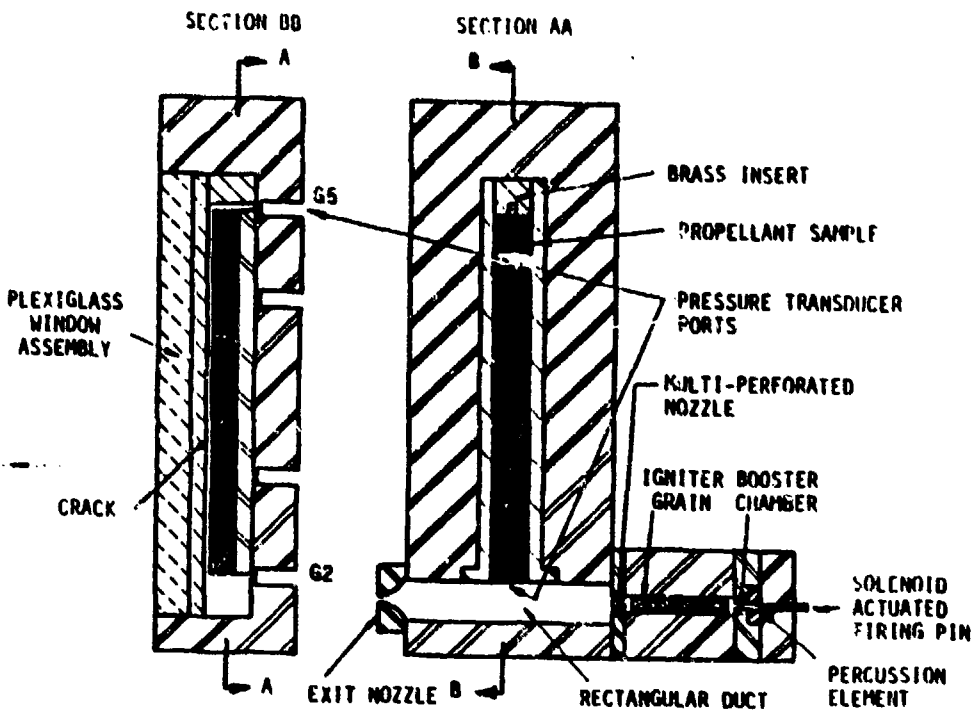
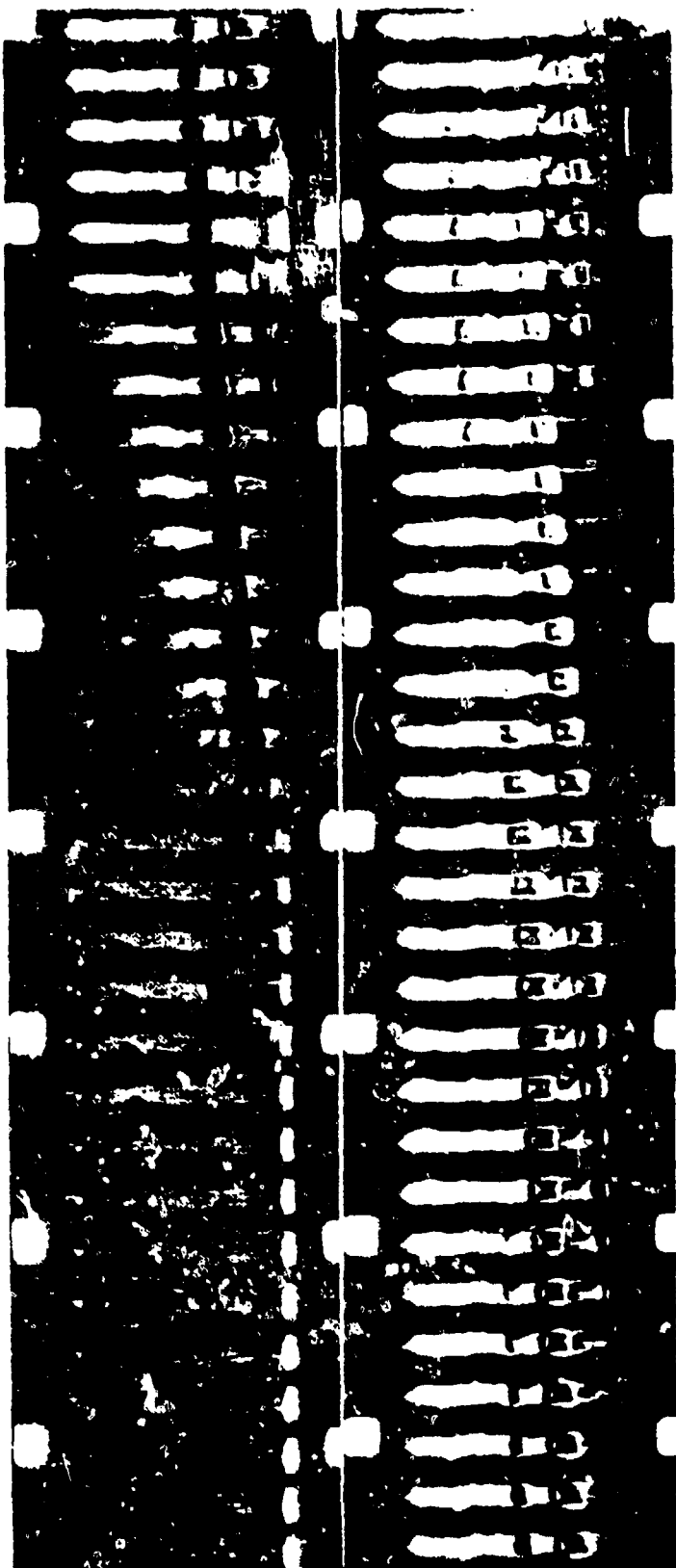


Figure 6 Schematic Diagram of Configuration Used for Detailed Observation of the Flame-Front

a slot of desired width in a propellant slab (see Refs. 2 and 3). Details of the experimental setup and experimental results are given in Refs. 2 and 3. The entrance of the crack gap is rounded to facilitate the gas penetration.

Figure 7 presents a sequence of pictures obtained from a test performed on a 183 mm long, narrow crack ($\delta \sim 455\mu\text{m}$). The framing rate in this case was 36,700 pictures per second. The crack configuration is the same as that shown in Fig. 6. It was observed that when the width of the crack gap is very small ($< 500\mu\text{m}$), partial closure of the crack occurs due to propellant deformation. This partial closure first appears near the entrance. As time progresses, the closure region moves downstream and a second partial closure region develops near the entrance. This process continues; at times, three or four such partial closures are observed simultaneously (for initial gap widths of the order of $450\mu\text{m}$). Usually, at the moment when the third closure develops at the entrance, the second and first are located, respectively, at approximately 20% and 50% of the crack length from the entrance. Later, as the combustion process becomes more pronounced, the partial closure regions disappear as a result of both propellant regression and higher pressure in the cavity.

The entire process is believed to be the result of deformation caused by high pressure acting on the propellant surface exposed to the chamber, and by the complex interaction between propellant deformation and pressure distribution in the crack cavity. Propellant surfaces exposed to the chamber are compressed by the high chamber pressure, which results in the propellant being



Filming Rate = 36,700 Pictures per Second

Figure 7 A Sequence of Photographs Showing Crack-Gap Closures

pushed into the crack. Since pressure increases faster in the chamber than in the crack, during this initial pressure transient, the propellant is pushed toward the region of lower pressure inside the crack. The mechanical deformation of the propellant causes narrowing of the crack gap, and consequently results in local crack closure.

THEORETICAL PREDICTIONS AND COMPARISONS

The important physical properties of the two propellants studied are given in Table I. Numerical values of the input variables used in the predictive program are listed in Table II. The recorded pressure-time trace near the crack entrance was used as an input. The temperature of hot gases in the chamber was assumed to be the adiabatic flame temperature of product gases from the igniter. An estimate of heat loss indicated that it is less than 3% of the chemical heat release; therefore, this assumption is justified. The flame temperature for propellant A was obtained from Price⁵⁷ of NWC; for the other propellant, it was computed from the CEC 72 thermochemistry program.⁵⁸

TABLE I Propellant Properties

Propellant Type	A	B
Composition	AP-based	AP/PBAA-EPON
Weight percent of oxidizer	-	75
Average particle size, d_{AP} , μm	-	76
Pre-exponential factor in Saint Robert's burning rate law, a , $\text{mm/s}/(\text{atm})^n$	1.62	0.9591
Pressure exponent in Saint Robert's burning rate law, n	.4108	.41
Flame temperature, T_f , K	3000	1920
Propellant density, kg/m^3	1710	1600

The calculated pressure distributions at various times for a typical test case for Propellant A are shown in Fig. 8. Results are presented only for the initial rapid pressure rise portion, since that is the region of interest for this study. The average pressurization rate at the crack entrance was 1.75×10^5 atm/s. During the initial period, a traveling pressure wave is present in the crack cavity. This wave moves toward the crack tip and is reflected from the tip, resulting in higher pressure near the tip at $t = 0.6$ ms. As time progresses, the overall pressure in the crack cavity continues to rise. This is the result of a combination of two simultaneous

TABLE II Numerical Values of Input Variables

<u>Variable</u>	<u>Units</u>	<u>Propellant A</u>	<u>Propellant B</u>
x_p	mm	0.0	0.0
x_L	mm	195.0	195.0
s_x	N/kg	0.0	0.0
b	m^3/kg	1.0×10^{-3}	1.0×10^{-3}
x_w	kg/kmole	26.10	20.381
γ	-	1.21	1.26
ρ_{pr}	kg/m^3	1710	1600
λ_{pr}	kcal/s-m-K	0.8×10^{-4}	0.5×10^{-4}
β_{pr}	m^2/s	0.18×10^{-6}	0.11×10^{-6}
c_s/d_h	-	.025	.025
T_f	K	3000	1920
T_{ign}	K	850	850
T_i	K	295	295
a	$(mm/s)/(atm)^n$	1.62	0.9591
n	-	0.4108	0.41
K_e	$m^3-K/kcal$	0.70×10^{-3}	-
α	-	53	-
T_c	K	1920	1920
G_1	atm	$14.4 + 136 e^{-0.095c}$	Same as A
χ	atm	47619	47619
K^*	$(MPa)^{-n_p} (m/s)^{-n_u}$	-	2×10^{-4}
n_p^*	-	-	0.705
n_u^*	-	-	1.252

*Defined in Eq. (28)

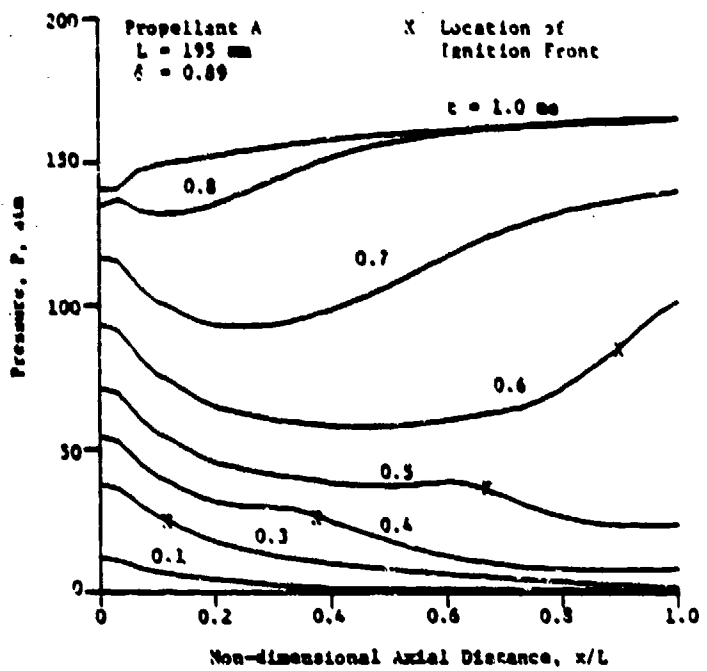


Figure 8 Calculated Pressure Distribution at Various Times

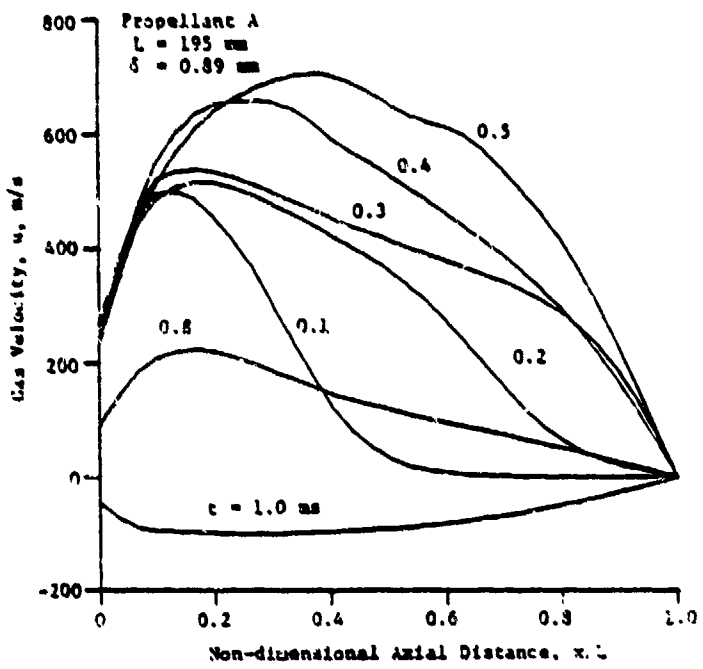


Figure 9 Calculated Velocity Distributions at Various Times

processes: a) a continuous increase in chamber pressure during this period, and b) mass addition due to burning of the crack walls. After about 0.8 ms, the pressure in the crack becomes more uniform because the rate of increase of chamber pressure has become quite small, and the ignition front has propagated to the tip. It should be noted that as time progresses, the maximum pressure in the crack cavity becomes higher than that in the chamber.

Predicted velocity distributions at various times are plotted in Fig. 9. At $t = 0.1$ ms, velocity in the latter half of the crack is almost zero. Because the initial favorable pressure gradient causes the gases to accelerate, the gas velocity at any axial location increases continuously until $t = 0.5$ ms. The adverse pressure gradient generated by the compression wave reflection at the crack tip causes the gases to decelerate. Since velocities continue to decrease after 0.5 ms, only one velocity distribution between 0.5 and 1.0 ms is shown in the figure to avoid confusion. At 1.0 ms, velocity in the entire crack is negative, i.e., gases flow out of the crack since pressure throughout the cavity is higher at that time than the pressure in the chamber.

Calculated temperature distributions at various times are shown in Fig. 10. During the initial period ($t = 0.1$ ms), a steep temperature gradient is present. This is due mainly to the fact that the initial increase in the temperature in the cavity is caused by hot gas penetration. Since the gas velocity in the second half of the crack is nearly zero at 0.1 ms, the temperature in that region is also equal to the initial temperature of the gas. As the propellant starts to burn, the temperature in the crack cavity begins to increase, and is dominated by the flame temperature of the propellant. Since the flame temperature of propellant A is higher than that of the igniter gases, and also there is a compression effect in the cavity, maximum temperature in the crack is higher than that in the chamber.

Variation in the port height (\pm half of the gap width) at various times is shown in Fig. 11. The initial geometry of the crack is shown by the dashed line. Because of the rounding of the crack entrance, the gap width at the entrance is large. During the initial period, the high chamber pressure acting on the crack surface exposed to the chamber causes the propellant near the crack entrance to be pushed inside, resulting in a decreased port height near the crack entrance. At $t = 0.6$ ms, there are two minimum gap widths; the second is due to the effect of compression wave reflection in the gas phase (see Fig. 8). As time progresses, however, the pressure in the cavity exceeds that in the chamber, and the propellant continues to burn; the net result is an increase in the port height at 1.0 ms.

Comparisons of predicted and measured pressure-time traces at $x = 48$, 138, and 188 mm are shown in Figs. 12, 13, and 14, respectively. The predicted values are in good agreement with the experimental data. The steepening of the pressurization as it moves along the crack is evident from both the predicted traces and experimental data. The effect of the increase in pressurization rate is most pronounced near the tip of the crack. This is due to the combined effect of coalescence of the compression waves and steepening of the pressure front caused by gasification of the propellant behind the front.

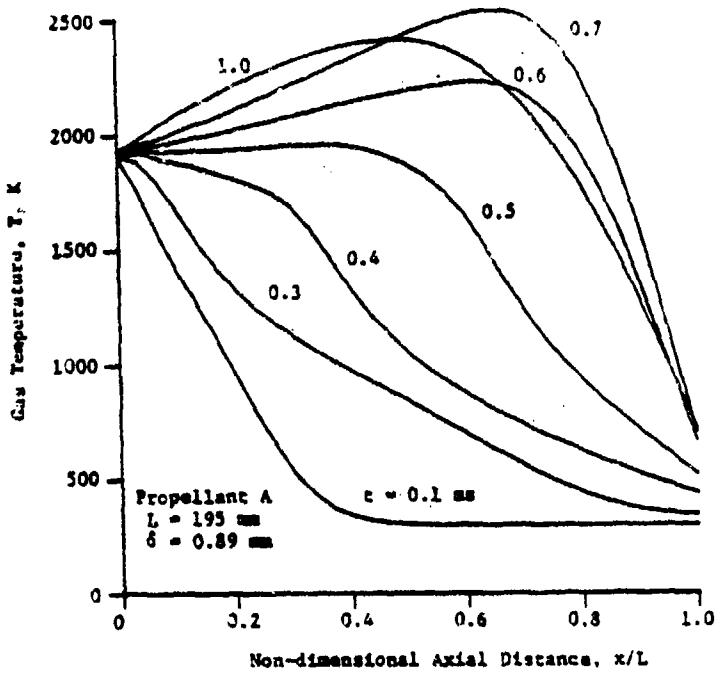


Figure 10 Calculated Temperature Distributions at Various Times

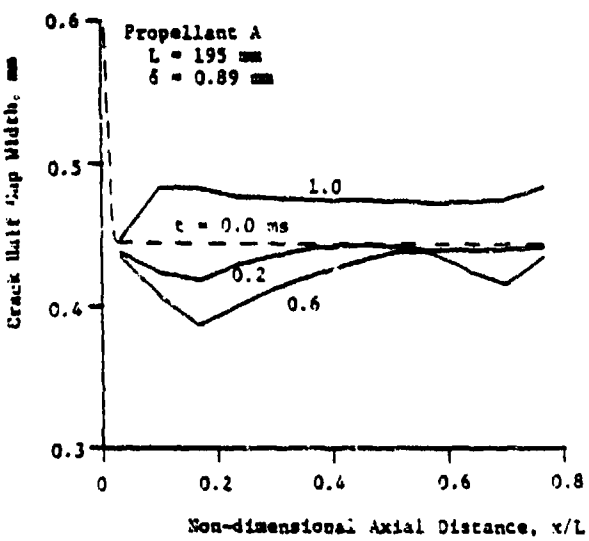


Figure 11 Calculated Variations in Port Height

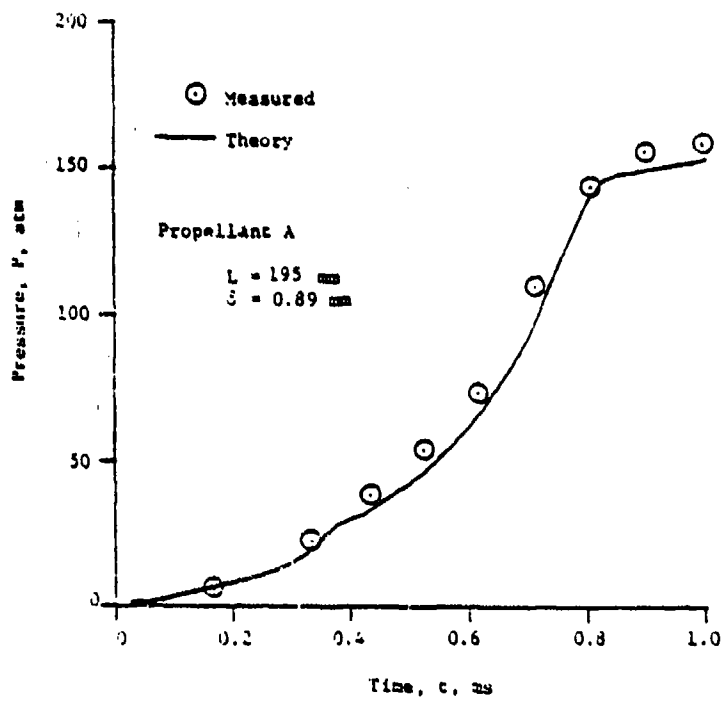


Figure 12 Comparison between Predicted and Measured Pressure-Time Traces at $x=48 \text{ mm}$

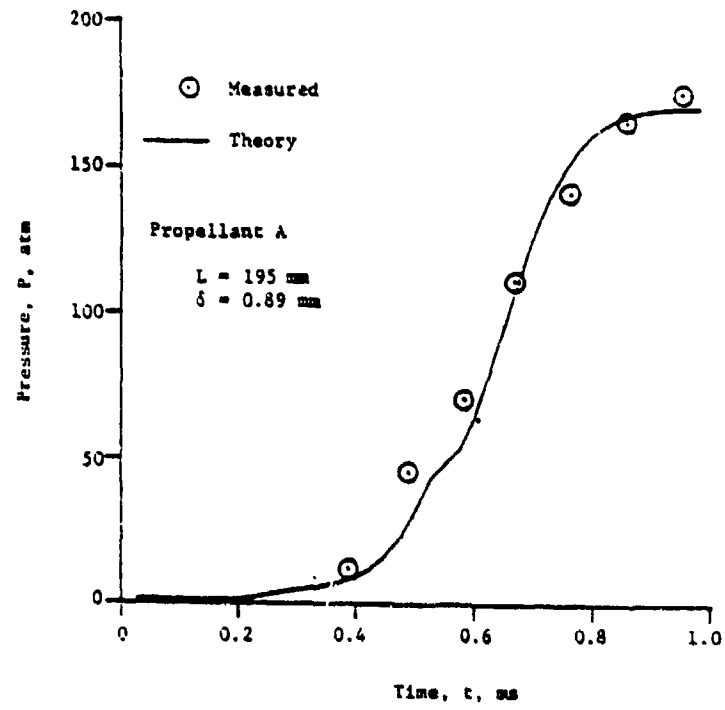


Figure 13 Comparison between Predicted and Measured Pressure-Time Traces at $x=138 \text{ mm}$

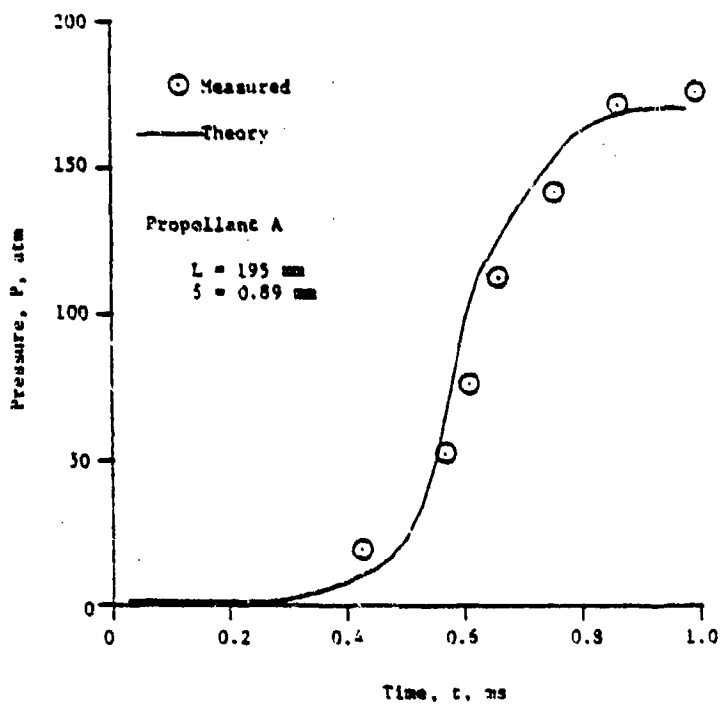


Figure 14 Comparison between Predicted and Measured Pressure-Time Traces at $x=188$ mm

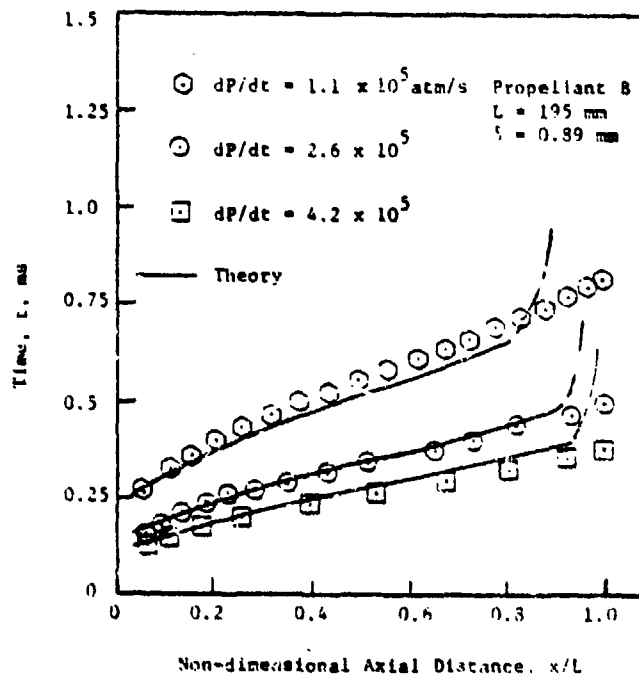


Figure 15 Comparison between Predicted and Measured Location of the Ignition Front for Various Pressurization Rates

Comparison of predicted and measured ignition-front locations for various pressurization rates is shown in Fig. 15. It can be seen that the model predicts the location of the igniton front quite well except very close to the tip. Near the tip region, the model overpredicts the deceleration of the ignition front. This is believed to be caused by the one-dimensional assumption in the model. The one-dimensional assumption is inadequate to describe the flow near the tip. Since the calculated velocities near the tip are small (see Fig. 9), both the gas temperature (see Fig. 10) and heat transfer coefficient are low; heat transfer to the propellant is, therefore, quite small. In an actual case, the presence of a secondary flow near the closed end will produce higher rate of heat transfer to the propellant, resulting in less pronounced flame front deceleration. It is believed that the discrepancy between the predicted and measured ignition-front locations near the tip region of the crack can be alleviated if the effect of enhanced heat transfer near the closed end can be incorporated into the model. It should be noted that, under the conditions studied, the initial flame-spreading process is not substantially affected by propellant deformation.

Figures 16 and 17 show calculated pressure distributions at various times for cases in which propellant deformation becomes very important. For results shown in Fig. 16 (Case 1), the chamber pressurization rate was 3.8×10^5 atm/s and the gap-width was 0.51 mm. Only those curves of interest are shown, and for ease of explanation, they are not superimposed. Between $t = 0.25$ and 0.275 ms, the pressure in the crack shows a wavy distribution which corresponds to the deformation pattern. During this period the crack gap at the entrance is extremely small (partially closed). At $t = 0.3$ ms, high pressures in the chamber and at the crack entrance cause the partial closure to move to $x/L = 0.1$, the gasification in the minimum flow area region results in a local pressure peak. The localized high pressure at $x/L = 0.1$ causes the propellant to deform; the region of partial gap closure moves to $x/L = 0.2$, resulting in a substantial increase of local pressure. The subsequent closure results in a zero gap width and causes the gas dynamic solution to blow up. The predicted movement of the partial gap closure is qualitatively similar to that observed experimentally (see Fig. 7).

Case 2, $\epsilon = 1$ m in Fig. 17, was computed for a pressurization rate of 5×10^5 atm/s and an initial gap width of .89 mm. Before 0.475 ms, the partial gap closure occurs near the crack entrance. Similar to case 1, both the high pressure near the entrance in the cavity and that acting on the side walls of the propellant exposed to the chamber cause the partial gap closure to move downstream. This area reduction and the continued gasification process result in a pressure peak near $x/L = 0.17$ (at 0.475 ms). At 0.5 ms, two regions of partial gap closures are obtained, resulting in pressure peaks at $x/L = 0.1$ and 0.27, respectively. As the pressure peak moves downstream, another gap closure develops near the entrance at 0.525 ms. This type of process continues in a repeated manner as shown by the distributions at $t = 0.525$ ms, 0.55 ms and 0.575 ms. Once again, these results qualitatively explain the behavior of the partial gap closures observed experimentally.

Results obtained here indicate that closure of the crack gap, which may initially occur at the crack entrance because of small gap widths and high

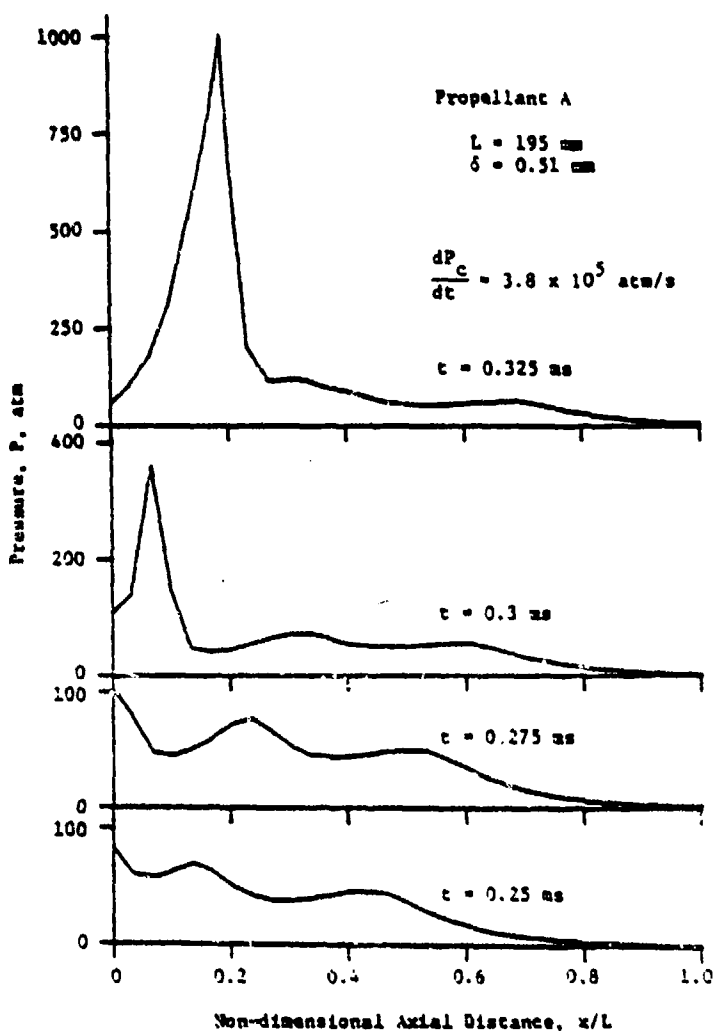


Figure 16 Calculated Pressure Distribution at Various Times during Crack-Gap Closure (Case 1)

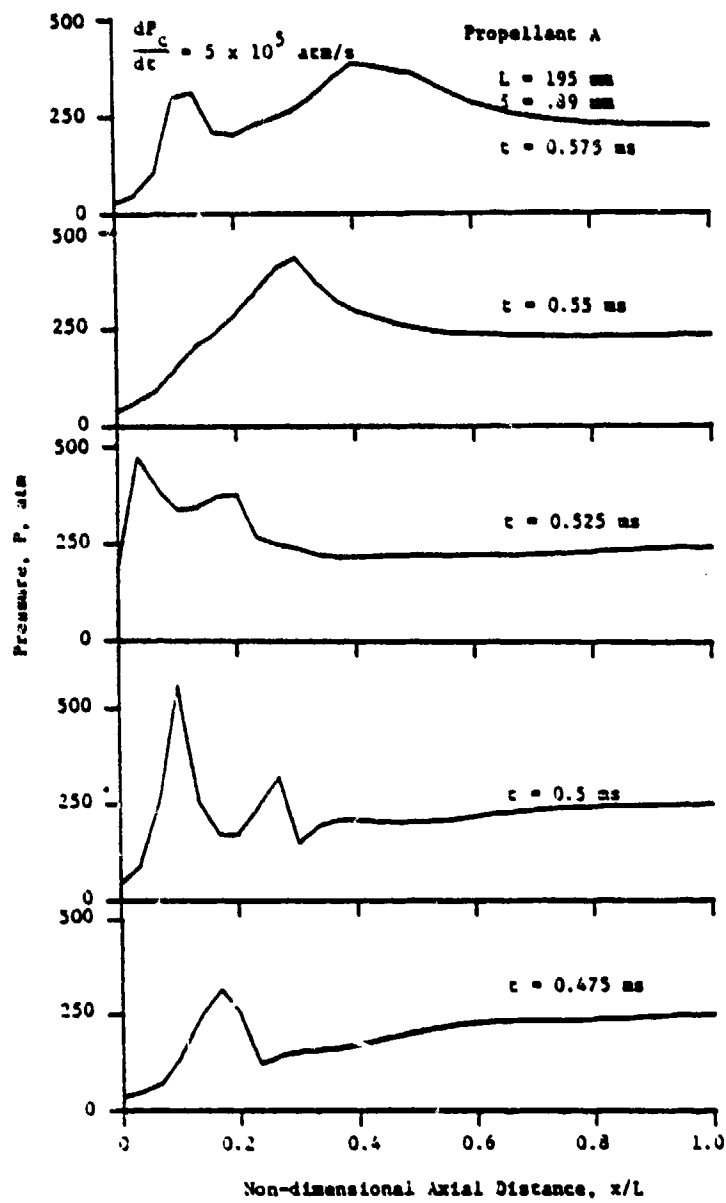


Figure 17 Calculated Pressure Distribution at Various Times during Crack-Gap Closure (Case 1)

chamber pressures, may propagate along the crack and result in local pressure peaks. The gap closure is not observed for cracks with large gap widths or at low chamber pressures because propellant deformation under these conditions is small and does not affect the ignition process substantially. Gap closures and resulting pressure peaks can strongly influence the convective burning process in the crack and may contribute to the deflagration-to-detonation transition process.

SUMMARY AND CONCLUSIONS

This research program was undertaken to investigate the development of convective burning in solid propellant cracks which continually deform due to burning and pressure loading. Both theoretical and experimental methods were employed to study the flame spreading and combustion processes in propellant cracks. In the theoretical model, the effect of inter-related structural deformation and combustion phenomena was taken into account by considering a) transient one-dimensional mass, momentum, and energy conservation equations in the gas phase, b) a transient, one-dimensional heat conduction equation in the solid phase, and c) quasi-static deformation of the two-dimensional, linear-viscoelastic propellant crack due to pressure loading. This set of coupled, nonlinear, partial differential equations was solved numerically. The gas-dynamic equations were solved using a finite difference analysis and the structure mechanics equation was solved using a finite element analysis.

Several important observations and conclusions from this study are summarized below.

1. Results indicate that coupling between chamber pressurization, crack combustion, and propellant deformation is quite important, especially in the case of very narrow cracks, and for high chamber pressurization rates.
2. Several regions of partial gap closures were observed experimentally in narrow cracks. Calculated results show that these partial closures may generate substantial local pressure peaks along the crack. The gap closures generally do not occur in the case of large gap widths or low chamber pressures.
3. The initial flame-spreading process, or the time for the ignition front to reach the crack tip, is not substantially affected by propellant deformation. However, structural deformation may significantly affect the pressure distributions along the crack.
4. Both theoretical and experimental results show that, in general, the maximum pressure in the crack cavity is higher than that in the chamber.
5. Except near the crack tip region, predicted results for the ignition front propagation are in good agreement with experimental data. Predicted and measured pressure distributions are also in good agreement.

NOMENCLATURE

<u>Symbol</u>	<u>Description</u>
A_p	Cross-sectional area of the crack, m^2
A_{px}	Spatial change of cross-sectional area of crack with respect to the axial distance, m
a	Pre-exponential factor in the nonerosive burning rate law, $a p^n$, $(mm/s)/(atm)^n$
B_x	Body force, N/kg
b	Co-volume, m^3/kg
c_f	Friction coefficient, $2g\tau_w/u^2$
c_p	Specific heat at constant pressure, kJ/kg-K
d_h	Hydraulic diameter of the crack, m
E	Total stored energy (internal and kinetic), kJ/kg
E_a	Activation energy for surface reactions
G_1	Relaxation modulus, kPa or atm
\bar{F}	Local convective heat-transfer coefficient, kJ/m^2-s-K
\bar{f}	Local convective heat-transfer coefficient over the propellant surface, kJ/m^2-s-K
\bar{h}_{cw}	Local convective heat-transfer coefficient over non-propellant port wall, kJ/m^2-s-K
K	Bulk modulus, kPa or atm
K_e	Erosive burning constant, m^3-K/kJ
L	Length of the crack, m
M_w	Molecular weight, kg/kmole
n	Pressure exponent in the non-erosive burning rate law
P	Pressure, kPa or atm
P_r	Prandtl number
P_b	Burning perimeter, m

P_w	Wetted perimeter of the port, m
R	Specific gas constant for the combustion gases, N-m/kg-K
Re	Reynolds number
r_b	Burning rate of the solid propellant, including the erosive burning contribution, mm/s
T	Temperature (without subscript, static gas temperature), K
T_{af}	Average film gas temperature, $(T + T_{ps})/2$, K
T_f	Adiabatic flame temperature of the solid propellant, K
T_{pi}	Initial propellant temperature, K
T_{ps}	Propellant surface temperature, K
T_{ws}	Nonpropellant wall surface temperature, K
t	Time, s
u	Gas velocity, m/s
v_k	The coefficient in viscosity-temperature relation
v_{gf}	The velocity of propellant gas at the burning surface, m/s
x	Axial coordinate, m
x_L	Position at the end of crack, m
x_p	Axial distance along the crack at which propellant begins, m
y	Perpendicular distance from the propellant surface into the solid, m

Greek Letters

α	Thermal diffusivity, m^2/s
β	Erosive burning exponent
γ	Ratio of specific heats
δ	Gap width of the crack, m
ϵ	Strain tensor
ϵ_s	Surface roughness, m
λ	Thermal conductivity, kJ/m-s-K

σ	Stress tensor
μ	Gas viscosity, kg/m-s
ρ	Density (without subscript, gas density), kg/m ³
τ_g	Characteristic time of the gaseous flame
τ_p	Transient pressure variation time (characteristic time of the pressure variation)
τ_s	Characteristic time of the unburned solid phase
τ_w	Shear stress on the port wall, kPa
τ_{xx}	Normal viscous stress, kPa
θ	Weighting parameter
θ_w	Angle measured, in a counterclockwise direction, at the lower side of the propellant, degree

Subscripts

c	Rocket chamber
cri	Critical condition for surface ablation
eff	Effective
g	Gas
i	Initial value
ign	Ignition condition
pr	Propellant
ps	Propellant surface

REFERENCES

1. Price, E.W., Ed., Proceedings of the ONR/AFCSR Workshop on "Deflagration to Detonation Transition," CPIA Publication 299, Sept. 1978.
2. Kumar, M., Kovacic, S.M., and Kuo, K.K., "Gas Penetration, Flame Propagation and Combustion Processes in Solid Propellant Cracks," AIAA Paper No. 80-1206, presented at the AIAA/SAE/ASME 16th Joint Propulsion Conference, July 1980.
3. Kumar, M., "A Study of Flame Spreading and Combustion Processes in Solid Propellant Crack," Ph.D. Thesis, The Pennsylvania State University, Aug. 1980.

4. Bradley, H.H., Jr., and Boggs, T.L., "Convective Burning in Propellant Defects: A Literature Review," Naval Weapons Center, China Lake, Calif., NWC TP 6007, Feb. 1978.
5. Belyaev, A.F., Bobolev, V.K., Korotkov, A.I., Sulimov, A.A., and Chuiko, S.V., Transition from Deflagration to Detonation in Condensed Phases, translated from Russian by Israel Program of Scientific Translations, Jerusalem, 1975.
6. Kuo, K.K., Chen, A.T., and Davis, T.R., "Convective Burning in Solid-Propellant Cracks," AIAA Journal, Vol. 16, June 1978, pp. 600-607.
7. Kumar, M., and Kuo, K.K., "Ignition of Solid Propellant Crack Tip Under Rapid Pressurization," AIAA Journal, Vol. 18, July 1980, pp. 825-833.
8. Kumar, M., and Kuo, K.K., "Flame Spreading and Combustion in Solid Propellant Cracks." Final Report to the Naval Weapons Center, China Lake, Calif., July 1980.
9. Kuo, K.K., Kumar, M., Kovacic, S.M., Wills, J.E., and Chang, T.Y., "Combustion Processes in Solid Propellant Cracks." Annual Report from The Pennsylvania State University to the Naval Weapons Center, China Lake, Calif., 1979.
10. Kuo, K.K., Kovalcin, R.L., and Ackman, S.J., "Convective Burning in Isolated Solid Propellant Cracks," Naval Weapons Center, China Lake, Calif., NWC TP 6049, Feb. 1979.
11. Belyaev, A.F., Kerotkov, A.I., Sulimov, A.A., Sukoyan, M.K., and Obmenin, A.V., "Development of Combustion in an Isolated Pore," Combustion, Explosion & Shock Waves, Vol. 5, No. 1, March 1969, pp. 4-9.
12. Belyaev, A.F., Bobolev, V.K., Korotkov, A.I., Sulimov, A.A., and Chuiko, S.V., "Development of Burning in a Single Pore," Transition of Combustion of Condensed Systems to Detonation, Chap. 5, Part A, Section 22, Science Publisher, 1973, pp. 115-134.
13. Kim, K., "Effect of Propellant Crack Burning on High Energy Propellant Safety," 16th JANNAF Combustion Meeting, Monterey, Calif., CPIA Publication 308, Dec. 1979, pp. 121-141.
14. Pilcher, D.T., "Modeling the DDT Process." Proceedings of the ONR/AFOSR Workshop on Deflagration-to-Detonation Transition," Atlanta, Ga., CPIA publication 299, Sept. 1978, pp. 143-160.
15. Kirsanova, Z.V., and Leipunskii, O.I., "Investigation of the Mechanical Stability of Burning Cracks in a Propellant," Combustion, Explosion, and Shock Waves, Vol. 6, No. 1, 1970, pp. 68-75.
16. Cherepanov, G.P., "Combustion in Narrow Cavities," Journal of Applied Mechanics and Technical Physics, Vol. 11, No. 2, 1970, pp. 276-281.

17. Belyaev, A.F., Sukoyan, M.K., Korotkov, A.I., and Sulimov, A.A., "Consequences of the Penetration of Combustion into an Individual Pore," Combustion, Explosion and Shock Waves, Vol. 6, April-June 1970, pp. 149-153.
18. Williams, M.L., and Jacobs, H.R., "The Study of Crack Criticality in Solid Rocket Motors," AFRPL TR 71-21, January 1971.
19. Jacobs, H.R., Williams, M.L., and Tuft, D.B., "An Experimental Study of the Pressure Distribution in Burning Flaws in Solid Propellant Grains," AFRPL-TR-72-108, Oct. 1972.
20. Jacobs, H.R., Hufferd, W.L., and Williams, M.L., "Further Studies of the Critical Nature of Cracks in Solid Propellant Grains," AFRPL-TR-75-14, March 1975.
21. Francis, E.C., Lindsey, G.J., and Parmerter, R.R., "Pressurized Crack Behavior in Two-Dimensional Rocket Motor Geometries," Journal of Spacecraft and Rockets, Vol. 9, June 1972, pp. 415-519.
22. Takata, A.N., and Wiedermann, A.H., "Initiation Mechanism of Solid Rocket Propellant Detonation," IITRI Interim Reports for AFOSR, Aug. 1976-Nov. 1979.
23. Takata, A.N., and Wiedermann, A., "Initiation Mechanism of Solid Rocket Propellant Detonation," 14th JANNAF Combustion Meeting, CPIA Publication 292, Dec. 1977.
24. Williams, M.L., "Initiation and Growth of Viscoelastic Fracture," International Journal of Fracture Mechanics, Vol. 1, Dec. 1964, pp. 292-310.
25. Knauss, W.G., "Stable and Unstable Crack Growth in Viscoelastic Media," Transactions of the Society of Rheology, Vol. 13, 1969, pp. 291-313.
26. Knauss, W.G., "Delayed Failure -- The Griffith Problem for Linearly Viscoelastic Materials," International Journal of Fracture Mechanics, Vol. 6, March 1970, pp. 7-20.
27. Knauss, W.G., and Dietmann, H., "Crack Propagation Under Variable Load Histories in Linearly Viscoelastic Solids," International Journal of Engineering Science, Vol. 8, Aug. 1970, pp. 643-656.
28. Mueller, H.K., and Knauss, W.G., "Crack Propagation in a Linearly Viscoelastic Strip," Journal of Applied Mechanics, Vol. 38, June 1971, pp. 483-488.
29. Knauss, W.G., "The Mechanics of Polymer Fracture," Applied Mechanics Review, Vol. 26, June 1973, pp. 1-7.

30. Francis, E.C., Carlton, C.H., and Lindsey, G.H., "Viscoelastic Fracture of Solid Propellants in Pressurization Loading Conditions," Journal of Spacecraft and Rockets, Vol. 11, Oct. 1974, pp. 691-696.
31. Nuismer, R.J., "On the Governing Equation for Quasi-Static Crack Growth in Linearly Viscoelastic Materials," Journal of Applied Mechanics, Vol. 41, 1974, pp. 631-634.
32. Knauss, W.G., "On the Steady Propagation of a Crack in a Viscoelastic Sheet -- Experiment and Analysis," Deformation and Fracture of High Polymers, edited by H.H. Kaush, J.A. Hassle, and R.K. Jaffe, Plenum Press, New York, 1974.
33. Knauss, W.G., and Mueller, H.K., Discussion of "On the Governing Equation for Quasi-Static Crack Growth in Linearly Viscoelastic Materials," Journal of Applied Mechanics, Vol 42, 1975, pp. 520-521.
34. Schapery, R.A., "A Theory of Crack Initiation and Growth in Viscoelastic Media, I. Theoretical Development," International Journal of Fracture, Vol. 11, Feb. 1975, pp. 141-159
35. Schapery, R.A., "A Theory of Crack Ignition and Growth in Viscoelastic Media, II. Approximate Methods of Analysis," International Journal of Fracture, Vol. 11, June 1975, pp. 369-388.
36. Schapery, R.A., "A Theory of Crack Initiation and Growth in Viscoelastic Media, III. Analysis of Continuous Growth," International Journal of Fracture, Vol. 11, Aug. 1975, pp. 549-562.
37. Swanson, S.R., "Application of Schapery's Theory to Viscoelastic Fracture of Solid Propellant," Journal of Spacecraft and Rockets, Vol. 13, September 1976, pp. 528-533.
38. Beckwith, S.W., and Wang, D.T., "Crack Propagation in Double-Base Propellants," Journal of Spacecraft and Rockets, Vol. 15, Nov. - Dec. 1978, pp. 355-361.
39. Langlois, G., and Gonard, R., "New Law for Crack Propagation in Solid Propellant Material," Journal of Spacecraft and Rockets, Vol. 16, No. 6, Nov. - Dec. 1979, pp. 357-360.
40. Swanson, S.R., "A Cohesive Crack Tip Model for Dynamic Viscoelastic Fracture," University of Utah Report, 1977.
41. Courant, R., and Hilbert, D., Methods of Mathematical Physics, Vol. 2, Interscience Publishers, New York, July 1966, pp. 407-550.
42. Peretz, A., "The Starting Transient of Solid Propellant Rocket Motors with High Internal Gas Velocities," Ph.D. Thesis, AMS Department, Princeton University, April 1973.

43. Peretz, A., Kuo, K.K., Caveny, L.H. and Summerfield, M., "Starting Transient of Solid-Propellant Rocket Motors with High Internal Gas Velocities," AIAA Journal, Vol. 11, No. 12, Dec. 1973, pp. 1719-1727.
44. Svehla, R.A., "Estimated Viscosities and Thermal Conductivities of Gases at High Temperatures," NASA TR R-132, 1962.
45. Bartz, D.R., "Survey of the Relationship Between Theory and Experiment for Convective Heat Transfer from Rocket Combustion Gases," Advances in Tactical Rocket Propulsion, AGARD Conference Proceedings No. 1, Technivision Services, Maidenhead, England, Aug. 1968, pp. 291-381.
46. Hilsenrath, J., et al, "Tables of Thermal Properties of Gases," U.S. Department of Commerce, NBS Circular 564, Nov. 1955.
47. Colebrook, C.F., "Turbulent Flow in Pipes with Particular Reference to the Transition Region Between the Smooth and Rough Pipe Laws," Journal of the Institute of Civil Engineers, Vol. 11, 1938-39, pp. 133-156.
48. Schlichting, H., "Turbulent Flow Through Pipes," Boundary Layer Theory, 6th Ed., McGraw-Hill, New York, 1968.
49. Razdan, M.K. and Kuo, K.K., "Measurements and Model Validation for Composite Propellants Burning Under Cross Flow Conditions," AIAA Journal, Vol. 18, June 1980, pp. 609-677.
50. Razdan, M.K., "Erosive Burning Study of Composite Solid Propellants by the Reacting Turbulent Boundary-Layer Approach," Ph.D. Thesis, The Pennsylvania State University, March 1979.
51. Lenoir, J.M., and Robillard, G., "A Mathematical Method to Predict the Effects of Erosive Burning in Solid Propellant Rockets," 6th Symposium (International) on Combustion, The Combustion Institute, Pittsburgh, Pa., 1956, pp. 663-667.
52. Vichnevetsky, R., and Tomalesky, A.W., "Spurious Wave Phenomena in Numerical Approximations of Hyperbolic Equations," Proceedings of the Fifth Annual Princeton Conference on Information Science and Systems, Princeton University, March 1971, pp. 1-7.
53. Chang, T.Y., and Prachuktam, S., "NFAP--A Nonlinear Finite Element Analysis Program," Report No. SE 76-3, Department of Civil Engineering, University of Akron, Ohio, Oct. 1976.
54. Bathe, K.J. and Wilson, E.L., "NONSAP--A Nonlinear Structural Analysis Program," Nuclear Engineering and Design, Vol. 29, No. 2, 1974, pp. 266-293.
55. Bathe, K.J., Wilson, E.L., and Iding, R.H., "NONSAP: A Structural Analysis Program for Static and Dynamic Response of Nonlinear Systems," University of California, Berkeley, CA, USENS 74-3, (also NTIS PB-231 112), Feb. 1974.

56. Chang, T.Y., Chang, J.P., Kumar, M., and Kuo, K.K., "Combustion-Structural Interaction in a Viscoelastic Material," Symposium on Computational Methods in Nonlinear Structural and Solid Mechanics, NASA CP 2147, Oct. 1980, pp. 67-90.
57. Price, C.F., Private Communication, Jan. 1978.
58. Gordon, S., and McBride, B.J., "Computer Program for Calculation of Complex Chemical Equilibrium Compositions, Rocket Performance, Incident and Reflected Shocks, and Chapman-Jouguet Detonations," NASA SP-273, 1971.

APPENDIX C
(Ref. No. 5)

**IMPROVED PREDICTION OF FLAME SPREADING DURING
 CONVECTIVE BURNING IN SOLID PROPELLANT CRACKS**

S. M. Kovacic,^{*} M. Kumar,[†] and K. K. Kuo^{*}

Department of Mechanical Engineering
 The Pennsylvania State University
 University Park, Pennsylvania

The development of convective burning in solid propellant cracks was studied both theoretically and experimentally. Comparison of the experimental results of flame spreading with the theoretical predictions of the previous crack combustion model (Kumar and Kuo 1980) showed good comparison except near the crack tip. The model was modified to include a) the effect of pressure-wave reflection near the crack tip on local ignition, b) the effect of flow recirculation in the crack-tip region on local heat transfer to the solid propellant, and c) turbulent transport terms in the Favre-averaged conservation equations along the crack. Predicted flame-spreading rates obtained from the modified model showed good agreement with experimental data, indicating significant improvements (near the crack tip) over predictions of the previous model. The inclusion of turbulent transport terms along the length of the crack did not significantly affect the flame-spreading process. Results of this study indicate that the effects of compression-wave reflection and recirculation are important in the crack tip region.

INTRODUCTION

Solid propellant grains sometimes develop cracks and flaws. These cracks or voids may be caused by defects in the manufacturing process, thermal stresses that occur during curing, the effect of aging during storage, damage received during handling and transportation, and thermal and mechanical stress during combustion. The cracks or flaws degrade the mechanical property and structural integrity of the grain. At the same time, they provide additional surface area for combustion. Burning within cracks may result in increased pressure in the cavity; the increased pressure may cause crack propagation, development of strong compression waves and possible generation of shock waves which could cause detonation.

Some of the processes found to be important [1-17] in ignition and com-

bustion of propellant cracks are: gas penetration into the crack, convective heating of the propellant crack surface prior to ignition, flame propagation along the crack, increased pressure in the crack cavity due to penetration of product gases and gasification associated with propellant burning, flow reversal when pressure inside the crack exceeds that of the main chamber, change in crack geometry due to burning as well as mechanical deformation, and propagation of the crack due to grain fracture. The governing parameters which have been found to influence convective burning [1-17] are: chamber pressure and pressurization rate, geometry of the crack, the effects of erosive burning caused by high-velocity gases present in the crack, physicochemical properties of the propellant, composition and flame temperature of igniter gases in the main chamber, and initial and boundary conditions to which the crack is subjected.

One of the important parameters which exerts a strong influence on time variation of the pressure distribution in the crack cavity is the instantaneous burning surface area. Since the flame-spreading rate determines the ignited

^{*}Graduate Student, presently working at TRW, DSSG, San Bernardino, California

[†]Assistant Professor

^{*}Associate Professor

fraction of the total surface area, accurate determination of the flame-propagation rate is important for better predictive capability of a model. Even though the present analysis is limited to a non-propagating crack, improved prediction of the flame-spreading rate would be helpful in developing models that include effects of crack propagation and branching. Furthermore, a detailed analysis of the flame spreading is desirable in order to understand some of the mechanisms associated with the multifacet problem of deflagration to detonation transition (DDT).

In the past, several researchers have investigated convective burning in propellant cracks. Prentice [1,2], Margolin and Margulis [3], Godai [4], Bobolev et al. [5], Payne [6], and Krasnov et al. [7] have studied the onset of convective burning. Preliminary investigations of the development of convective burning were conducted by Belyaev et al. [8,9]. Both theoretical and experimental investigations of the development of convective burning in solid propellant cracks have been conducted at The Pennsylvania State University [10-15]. Detailed reviews of previous research in this area are given in Refs. 11, 16, and 17. The crack combustion model developed by Kuo et al. [10,11] provided the basis for the present theoretical study.

This model [10,11] considers transient one-dimensional mass, momentum, and energy conservation equations in the gas phase. A one-dimensional transient heat conduction is considered in the solid phase. As the gas flows over the crack surface, it heats the propellant. Flame spreading is postulated to result from successive ignitions of adjacent surfaces by convective heat transfer. A comparison of predicted results from the Kuo model [10,11] and experimentally measured [13] ignition-front locations indicated that the model tends to underpredict the flame-spreading rate near the tip region [11, 14]. It appears that one of the main reasons for this discrepancy is the one-dimensional nature of the model. The assumption of one-dimensional flow is adequate along the crack; however, it cannot describe the flow recirculation near the crack tip. Predicted velocities near the crack tip are small, resulting in low gas temperature and heat transfer coefficient; consequently, the predicted rate of heat transfer to the surface is small.

In reality, the presence of recir-

culating flow near the tip region will cause the heat-transfer rate to be higher than that predicted by the one-dimensional model. A recent study [12] found that the effect of compression wave reflection and recirculation near the crack tip is important for ignition of the crack tip. In some of the experiments [15], it was found that the crack tip ignited before the convective ignition front reached the tip, leading to the conclusion that heat transfer process near the tip is different from that along the crack. It is clear that these complex processes near the crack tip must be taken into account to improve prediction of flame spreading.

This study was directed toward improving the predictive capability of the convective-burning theoretical model [10,11] by including a) the effect of pressure-wave reflection at the crack tip on the ignition process, b) an approximation to account for the effect of recirculating flow near the crack tip on local heat transfer to propellant surface, and c) turbulent transport terms in conservation equations along the crack. The objectives of this study are:

1. To improve the predictive capability of the convective-burning model so that the rate of flame propagation in a solid propellant crack can be accurately predicted.
2. To compare the predictions of the modified crack combustion model with experimental data of flame spreading and pressurization in propellant cracks.

ANALYSIS

The present model was developed to simulate a transverse propellant crack inside a rocket chamber, as shown in Fig. 1. Hot, high pressure gases from the main chamber penetrate the crack and transfer heat to unburned propellant surfaces. The rate of convective heat transfer from the hot gases to the propellant is determined by the instantaneous values of gas velocity, temperature, density, and local propellant surface temperature. As the gases continue to flow into the crack, gas pressure, temperature, and density along the crack increase. After being heated for a period of time, the propellant surface will begin to gasify or ignite, generating more hot gases. The flame will spread along the crack until the entire crack is ignited. It is possible that the local internal pressure may exceed the main chamber pressure, causing flow

reversal, with hot gases generated by the ignited propellant being forced out of the open end of the crack.

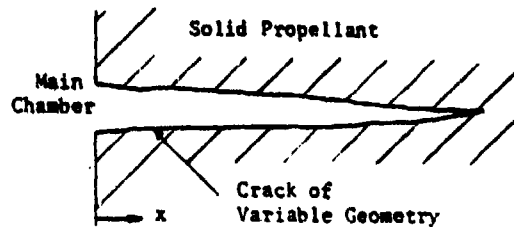


Fig. 1 Schematic of a Solid Propellant Crack

The following basic assumptions are employed in the analytic model:

- (1) Bulk flow of gases along the propellant crack is quasi-one-dimensional.
- (2) Gases flowing into the propellant crack obey the Nobel-Abel law for imperfect gases.
- (3) The flame zone is small compared to the gap width of the crack.
- (4) Rate processes in the gaseous flame are considered quasi-steady; that is, the characteristic time associated with the gas phase reactions is short compared to that of the transient pressure variation.
- (5) Deformation of the solid propellant is neglected during the flame-spreading process. Any changes in the geometry of the crack are due solely to ablation of the propellant surface.
- (6) Thermal properties of propellant are constant.

Most of these assumptions are justified for crack combustion studies [11,14]. Even though the propellant is deformable, it has been found that deformation does not significantly influence the flame-spreading process [14].

Based upon these assumptions, the quasi-one-dimensional, unsteady mass, momentum, and energy equations for the gas phase were obtained in terms of the instantaneous variables [18]. Instantaneous gas-phase equations were converted into a set of mean-conservation equations by using an averaging technique for turbulent flows. Since the gas is highly incompressible, the Favre de-

composition technique [19] was used. Neglecting the third-order turbulent correlations, the three Favre-averaged conservation equations can be written as follows:

Mean mass conservation equation:

$$\frac{\partial}{\partial t} (\bar{\rho} A_p) + \frac{\partial}{\partial x} (\bar{\rho} \bar{u} A_p) = r_b \rho_p P_b \quad (1)$$

The mean momentum conservation equation:

$$\begin{aligned} \frac{\partial}{\partial t} (\bar{\rho} \bar{u} A_p) + \frac{\partial}{\partial x} (\bar{\rho} \bar{u}^2 A_p) + \frac{\partial}{\partial x} (\bar{\rho} u'' u'' A_p) \\ = - \frac{\partial}{\partial x} (\bar{F} A_p) + \frac{\partial}{\partial x} \left[\frac{4}{3} u A_p \frac{\partial}{\partial x} (\bar{u} + \bar{u}'') \right] \\ + \bar{P} \frac{\partial}{\partial x} (A_p) - \frac{1}{2} f P_w \bar{\rho} \bar{u} |\bar{u}| \cos \theta_w \\ + \bar{\rho} A_p B_x - (r_b \rho_p P_b) V_{gf} \sin \theta_w \quad (2) \end{aligned}$$

The mean energy conservation equation:

$$\begin{aligned} \frac{\partial}{\partial t} (A_p [\rho C_v \bar{T} + \bar{\rho} \bar{u}^2 + \frac{1}{2} \bar{\rho} u'' u'']) \\ = - \frac{\partial}{\partial x} [A_p C_p (\bar{\rho} \bar{u} \bar{T} + \bar{\rho} u'' T'')] \\ - \frac{\partial}{\partial x} [A_p (\bar{\rho} \bar{u}^2 + 3 \bar{u} \bar{\rho} u'' u'')/2] \\ + \frac{\partial}{\partial x} [k A_p \frac{\partial}{\partial x} (\bar{T} + \bar{T}'')] \\ + (r_b \rho_p P_b) C_o T_f + \bar{\rho} \bar{u} A_p B_x \\ - E_{cp} P_b (\bar{T} - T_{ws}) \\ - E_{cw} (P_w - P_b)(\bar{T} - T_{ws}) \quad (3) \end{aligned}$$

The equation of state for the gas phase:

$$F \left(\frac{1}{\delta} - b \right) = RT \quad (4)$$

Further approximations are needed in order to achieve turbulence closure of the model. In an attempt to keep the model simple, and at the same time to take into account most of the important physical processes, the following relationships were used:

$$- \bar{\rho} u'' u'' = u_t \frac{\partial \bar{u}}{\partial x} \quad (5)$$

$$- C_o \bar{\rho} u'' T'' = k_t \frac{\partial \bar{T}}{\partial x} \quad (6)$$

These relationships could be regarded as the definitions for μ , and k . In addition, some further simplifications were made; these include

$$u \gg \bar{u}; \bar{T} \gg T^* \quad (7)$$

and

$$\bar{\rho}(c_v \bar{T} + \frac{u^2}{2}) \gg \frac{1}{2} \rho u^2 \quad (8)$$

The three mean conservation equations were rearranged to form a set of governing equations for calculating gas-phase temperature, pressure, and velocity.

The propellant surface temperature at any location along the crack before attainment of ignition is calculated by solving the transient, one-dimensional heat conduction equation in the same manner as given in Refs. 10 and 11. A two-temperature ignition criterion, simulating onset of ablation and ignition, is used to determine surface gasification and burning conditions. The temperature profile in the solid propellant is solved until ignition is achieved.

Empirical correlations are supplied for the heat-transfer coefficient, drag coefficient, propellant burning-rate law, etc. Sources of the correlations used in model are summarized in Table 1.

Table 1. Empirical Correlations Used in the Model

Parameter	Source
Heat transfer coefficient	Modified Dittus-Boelter correlation [20]
Gas viscosity	Svehla expression [21]
Franndt number	Svehla formula [21]
Friction coefficient	Modified Colebrook correlation [22,33]
Strain burning rate	Saint-Robert expression [24]
Erosive burning rate	Lenoir-Robillard [25] or Ruzdan-Kuo formula [26]

Initial conditions for the gas-phase equation describe a uniform distribution in the crack:

$$\bar{u}(0,x) = u_1; \bar{T}(0,x) = T_1; \\ \bar{P}(0,x) = P_1 \quad (9)$$

Boundary conditions depend upon flow conditions at the crack entrance

[10,11]. When the gases enter the crack, boundary conditions are:

$$\bar{P}(t,0) = P_c(t); \bar{T}(t,0) = T_c(t); \\ \bar{u}(t,x_L) = 0 \quad (10)$$

When the gases flow out of the crack subsonically, boundary conditions are:

$$\bar{P}(t,0) = P_c(t); \bar{u}(t,x_L) = 0 \quad (11)$$

When gases exit the crack supersonically, the boundary condition is that mean gas velocity at the crack tip is zero.

The equations and boundary conditions given above describe gas flow along the crack. As mentioned in the Introduction, heat-transfer processes near the tip region should include the effect of pressure-wave reflection and flow recirculation in order to improve prediction of the flame-propagation rate. As reported by Kumar and Kuo [12], the effect of pressurization rate and pressure-wave reflection is important for heat transfer at the end of a crack and for local ignition. Since the flow conditions and crack configuration of this study are similar to those presented in Ref. 12, the tip-ignition model [12] is compatible for direct incorporation into the present theoretical model. In the tip-ignition model, the propellant at the closer end is considered to be thermally thick. The propellant surface at the tip is heated by hot gases driven into the crack as a result of rapid chamber pressurization and the presence of strong pressure gradient forces. The tip-ignition model describes the process of heating to ignition at the closed end of the propellant crack; accordingly, this model is incorporated for calculations at the tip.

Although recirculating flows in gaps have been researched quite extensively [27,28], most researchers have only studied gaps with small length-to-diameter ratios (in the order of 5). Cracks with length-to-diameter ratios in the range of 30 to 200 were used in the present study. Kuo et al. [29] conducted flow-visualization experiments on gaps with aspect ratios as high as 24.5, but did not give special attention to recirculation near the tip of the crack.

As an attempt to improve the flame spreading prediction in the tip region without having to solve a complex multi-dimensional problem, a simple method

for approximating the rate of heat transfer caused by flow recirculation was incorporated into the theoretical formulation. As a first approximation, a condition of linear heat flux to the propellant was imposed between a point in the crack at the edge of the recirculation region and the tip of the crack. The heat flux, at any point before the region of recirculation, was calculated, using the temperature difference between the gas and solid phase and the heat-transfer coefficient based upon the modified Dittus-Boelter correlation [20]. The heat flux at the crack tip was calculated, using the tip-ignition model [12]. The heat flux at any point in the recirculation region was determined by interpolating between the flux at the crack tip and that at the edge of the recirculation region. The initial selection of the size of the recirculation region was based upon a good match between experimentally measured flame-spreading rates and theoretically calculated results for one test case. It was found that the location of the edge of the recirculation zone, so long as the length of the recirculation zone was about 1/5th of the crack length, does not significantly affect results.

The numerical technique for solving the gas and solid-phase governing equations along the crack employs an implicit scheme, similar to that given in Refs. 10 and 11. The crack combustion model calculates gas pressure and temperature in the region adjacent to the crack tip, and the tip ignition model calculates heat flux and surface temperature of the propellant at the crack tip. Numerical solution of crack combustion model equations and tip ignition model equations is carried out separately, but concurrently.

RESULTS AND DISCUSSION

An experimental investigation was conducted in order to validate results obtained from the theoretical model. A test rig was designed to simulate, as closely as possible, actual rocket chamber conditions. An igniter system incorporating a solid propellant charge was used as the source of hot gas generation. High-speed photographs and quick response pressure transducers were used to observe flame propagation and to measure pressure along the crack. Detailed discussions of the experimental setup and procedure can be found in Refs. 11 and 13. Two types of AP composite solid propellants were studied. Table 2 lists some of the important propellant properties.

Table 2 Propellant Properties and Input Parameters

Parameter (Unit)	Propellant A	Propellant B
Propellant Composition	AP-based	AP/FBAA-EPOI
a ($\text{mm}^2/\text{s}\cdot\text{atm}^n$)	1.62	0.3531
n (-)	0.4108	0.4100
T _f (K)	3000	1920
ρ_p (kg/m^3)	1710	1600
k _p (W/m-K)	3.35	2.1
a _p (m^2/s)	0.18x10 ⁻⁶	0.11x10 ⁻⁶
M _w (kg/kmole)	26.1	20.38
y (-)	1.21	1.26
b (m^3/kg)	0.001	0.001
T _{ign} (K)	50	950
μ_{eff}/μ (-)	100	100
Ref. 18		
k _{eff} /k (-)	300	300
Ref. 12		

Figures 2 and 3 display two sets of pressure traces from test firings in which all test conditions except the crack-gap width were approximately the same. Gap widths for Test 62 (Fig. 2) and 63 (Fig. 3) were 1.27 and 0.508 mm, respectively. Four pressure gauges (92-95) were used to measure pressure at four axial locations along the crack. Several differences can be seen from these pressure traces present in the two tests. In both tests, the rate of pressurization increases consecutively at each downstream location from the crack entrance, but the crack with smaller gap width experiences a higher peak pressure. Furthermore, the highest peak pressure occurs in the interior of the narrow crack, whereas peak pressure is much more uniform in the wider crack. This can be explained by noting that in both cracks the burning surface area is identical, but the port area in the narrow crack is proportionally smaller than that of the wide crack. As the propellant along the crack begins to oxidize, local pressure inside the crack may become greater than chamber pressure, causing gas flow to reverse and begin to exit the crack. The gaseous mass generated by the burning propellant soon becomes greater than the mass which is able to exit from the orifice of the crack, and the pressure inside the crack builds toward a maximum. For the narrow crack, the smaller port area will restrict the exiting flow sooner, resulting in a

higher peak pressure within the crack. Higher pressure in the interior of the narrow crack also causes the burning rate to increase, thus further increasing the pressure. Eventually, the pressure in the interior is higher than the pressure at the crack opening.

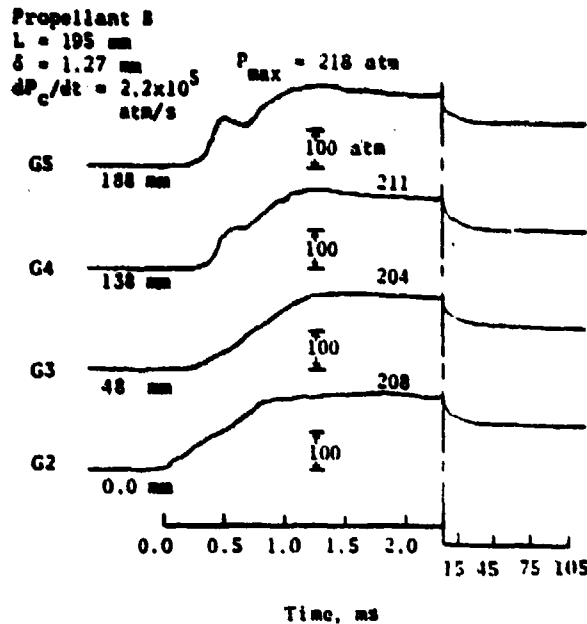


Fig. 2 Measured Pressure-Time Traces for Test 62

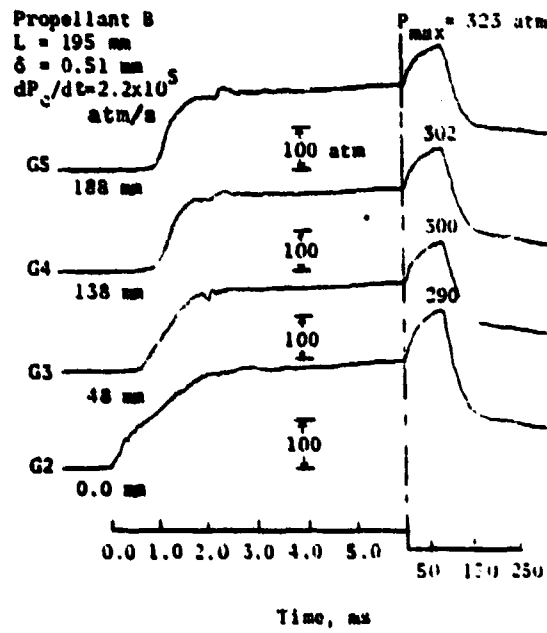


Fig. 3 Measured Pressure-Time Traces for Test 63

Another important difference between Test 62 and 63 is the effect of crack-gap width on pressure waves traveling along the crack. Pressure traces from Test 62 (shown in Fig. 2) indicate the presence of a strong pressure wave traveling along the crack, resulting in the local peak and valley at G5. The local peak is caused by the compression wave reflection at the crack tip, and the valley is believed to be the result of expansion waves generated by the reflection of the compression wave at the crack entrance. Pressure traces from Test 63 (shown in Fig. 3) indicate no strong pressure waves moving along the crack. This can be explained by considering the mechanical deformation of the propellant along the crack. As gases enter the crack, pressure waves traveling toward the crack tip coalesce and become stronger. In the region close to the pressure wave front, the propellant walls of the crack deform, increasing the local crack volume and lowering the local pressure in the region near the pressure wave front. In a very narrow crack, mechanical deformation of the propellant due to pressure loading can be very important. Propellant deformation for a given pressure will be approximately the same for the same web thickness, but the percentage change in the port area will increase as the original crack tip width decreases. The gap width of Test 63 is 2.5 times smaller than that of Test 62; hence the pressure wave effect is much less pronounced in Test 63.

The effect of chamber pressurization rate on the pressure-time history of the crack can be seen by comparing two sets of pressure traces from Tests 64 and 65 as shown in Figs. 4 and 5. These two tests were conducted with the same propellant (Propellant A) and same crack geometry ($L = 195 \text{ mm}$, $\delta = 0.89 \text{ mm}$), but with different chamber pressurization rates. Test 65, with a chamber pressurization rate of about $4.5 \times 10^5 \text{ atm/s}$, exhibits a strong pressure wave effect along the crack, while Test 64, with a chamber pressurization rate of about $1.3 \times 10^5 \text{ atm/s}$, shows no significant pressure wave effect in the crack.

Figures 6 to 9 present a comparison of predicted and measured flame front locations. The dashed lines represent predicted flame front locations obtained from the previous study [5, 11]; the solid lines present results obtained from the present study. The plots show the time required for the ignition front to reach a particular

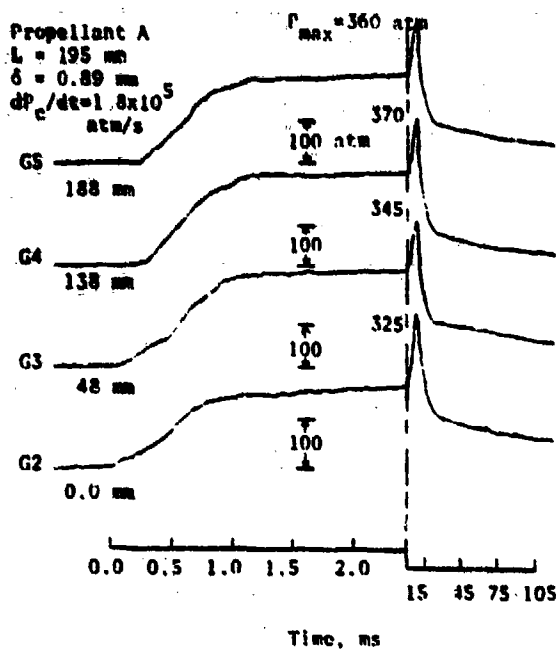


Fig. 4 Measured Pressure-Time Traces for Test 64

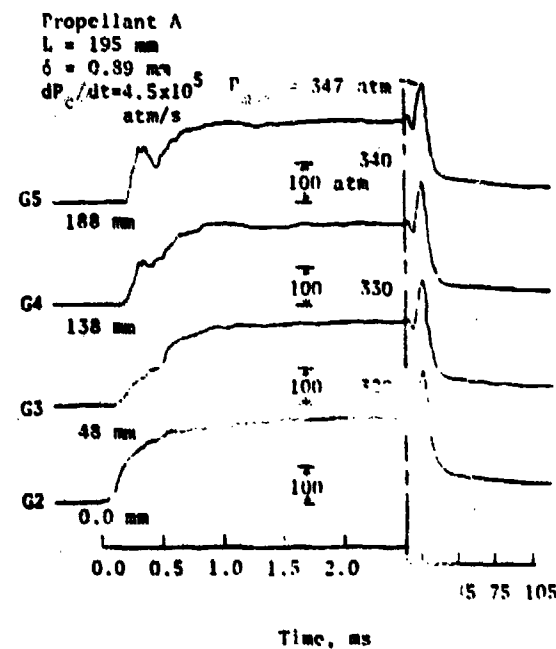


Fig. 5 Measured Pressure-Time Traces for Test 65

location versus the nondimensional axial distance along the crack. Substantial improvement in the prediction of the flame front near the crack tip region can be seen from these figures. The effect of various parameters on flame front propagation is given in Refs. 11 and 12.

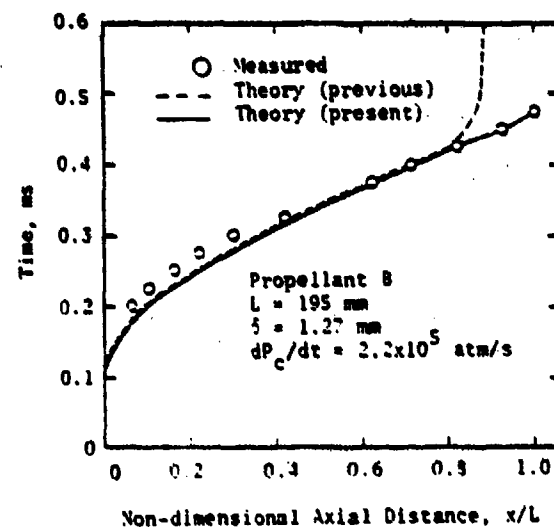


Fig. 6 Comparison of Predicted and Measured Ignition Front Propagation for Test 62

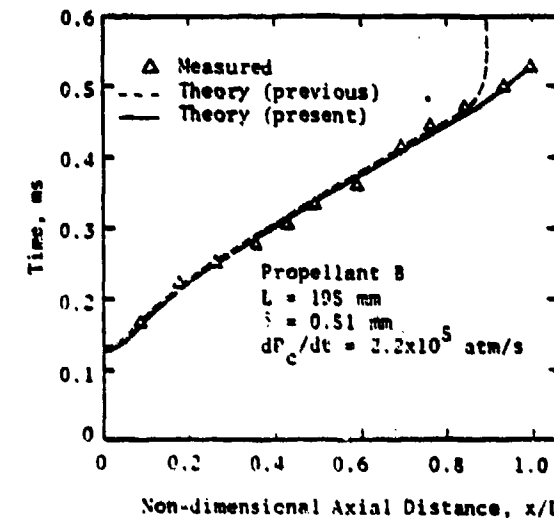


Fig. 7 Comparison of Predicted and Measured Ignition Front Propagation for Test 63

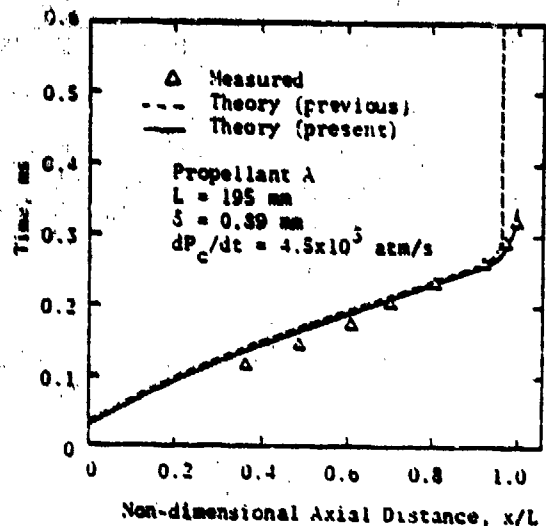


Fig. 8 Comparison of Predicted and Measured Ignition Front Propagation for Test 65

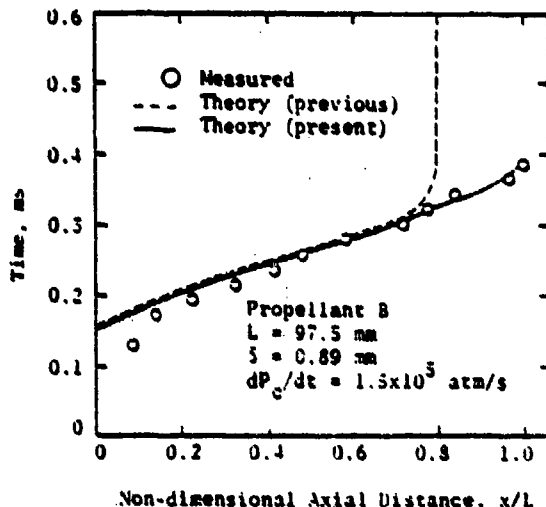


Fig. 9 Comparison of Predicted and Measured Ignition Front Propagation for Test 74

The predicted pressure variations with respect to time and axial distance for Test 74 is shown in a three-dimensional plot in Fig. 10. (Flame-spreading results of this test are shown in Fig. 9). In Fig. 10, the traveling pressure wave front can clearly be seen moving back and forth along the crack as time progresses. The calculated pressure-time trace is in reasonable agreement with the measured data [18]. The physical reason for the presence of crests and troughs on the plot is the same as that given earlier in the explanation of pressure peaks and valleys present in Figs. 2 and 5.

Propellant B

L = 97.5 mm

S = 0.89 mm

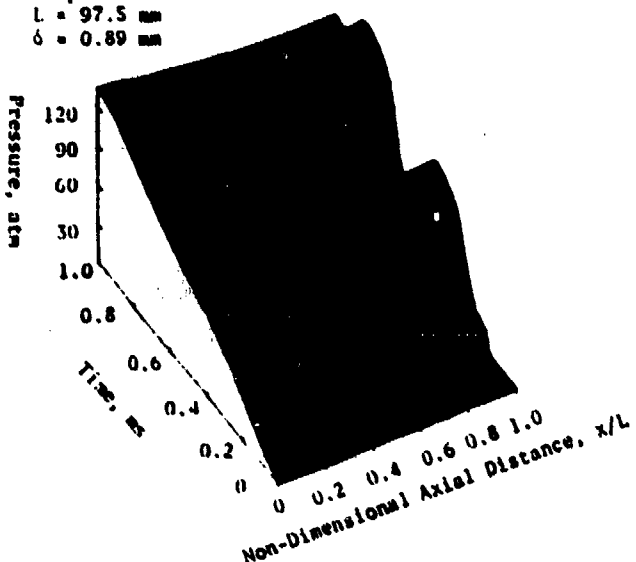


Fig. 10 Predicted Pressure Distributions Versus Time for Test 74

Predicted velocity variations with respect to time and axial distance for Test 74 are also shown in a three-dimensional plot in Fig. 11. During the initial period, the favorable pressure gradient causes the hot gas to penetrate the opening portion of the crack. As the propellant begins to burn and the flame continues to spread, local pressure and temperature increase, further facilitating gas penetration deeper into the crack and increasing gas velocity. As the pressure in the cavity increases, the favorable pressure gradient effect diminishes, resulting in a decrease in gas velocity. When t is about 0.45 ms, the adverse pressure gradient in the crack becomes strong enough to reverse flow; thereafter, gases produced in the crack cavity flow out of the crack. Velocity distribution is generally dictated by pressure distribution.

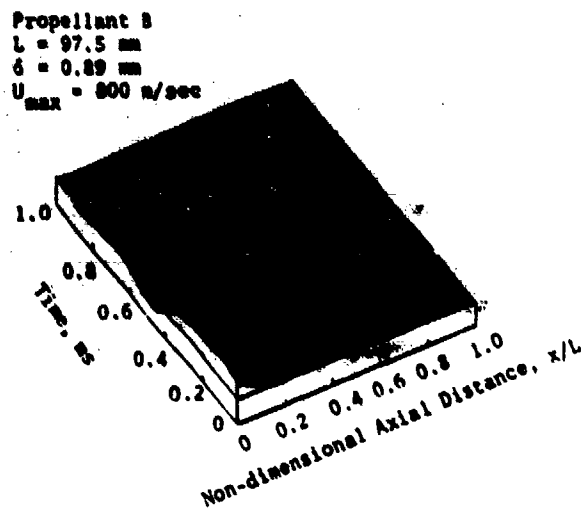


Fig. 11 Predicted Velocity Distributions Versus Time for Test 74

Results of the numerical computations show that although gas flow in the propellant crack is highly turbulent and high temperature gradients are present, as expected, the effect of turbulent transport in the axial direction was not significant when compared with other terms in the energy equation [18]. This is due to the fact that the flow is highly convective, and the energy transfer in the axial direction is dominated by convection caused by high gas velocities. The diffusion of energy in the axial direction by turbulent transport is much smaller than that by convective energy transport.

CONCLUSIONS

Several important observations and conclusions from this investigation are summarized below.

- (1) Predicted ignition front propagation, using the current theoretical model, was in very good agreement with experimental data, indicating significant improvement over predictions of the previous model near the crack tip.
- (2) The effects of compression wave reflection and flow recirculation are important in consideration of heat transfer between gas and solid propellant near the crack tip.

(3) Both experimental and theoretical results exhibit a traveling pressure wave phenomenon. This phenomenon is more pronounced with increases in crack gap width or chamber pressurization rate.

(4) Since the axial transport of energy in the gas phase is strongly dominated by convection, the inclusion of axial turbulent transport terms in the governing equations does not affect the flame-spreading rate along the crack.

ACKNOWLEDGEMENT

This research represents a part of results obtained under the project sponsored by the Power Program of the Office of Naval Research, Arlington, Virginia, under Contract No. N00014-79-C-0762. The support of Dr. Richard S. Miller is greatly appreciated.

NOMENCLATURE

A_p	Cross-sectional area of the crack, m^2
a	Pre-exponential factor in the non-creative burning rate law, m^n , $(\text{mm}/\text{s})/(1\text{atm})^n$
B_x	Body force, N/kg
b	Shear force, N/kg
C_p	Specific heat at constant pressure, $\text{J}/\text{kg}\cdot\text{K}$
C_v	Specific heat at constant volume, $\text{J}/\text{kg}\cdot\text{K}$
f	Friction coefficient, N_w/m^2
h_{cp}	Local convective heat-transfer coefficient over the propellant surface, $\text{W}/\text{m}^2\cdot\text{K}$
h_{cw}	Local convective heat-transfer coefficient over non-propellant port wall, $\text{W}/\text{m}^2\cdot\text{K}$
k	Thermal conductivity, $\text{W}/\text{m}\cdot\text{K}$
k_{eff}	$k + k_w$, $\text{W}/\text{m}\cdot\text{K}$
L	Length of the crack, m
M_w	Molecular weight, kg/kmole
n	Pressure exponent in the non-creative burning rate law
P	Pressure, Pa
P_b	Burning perimeter, m
P_w	Wetted perimeter of the port, m
R^*	Specific gas constant for the combustion gases, $\text{N}\cdot\text{m}/\text{kg}\cdot\text{K}$
r_b	Burning rate of the solid propellant, including the erosive burning contribution, m/s
T	Temperature (without subscript, static gas temperature), K
T_f	Adiabatic flame temperature of the solid propellant, K
T_{ps}	Propellant surface temperature, K
T_{ws}	Nonpropellant wall surface temperature, K
t	Time, s
U	Gas velocity, m/s

v_{sf} The velocity of propellant gas at the burning surface, m/s
 x Axial coordinate, m

Greek Letters

α Thermal diffusivity, m^2/s
 γ Ratio of specific heats
 δ Gap width of the crack, m
 μ Gas viscosity, $kg/m \cdot s$
 ρ_{eff} $\rho + \rho_t$, kg/m³
 ρ_0 Density (without subscript, gas density), kg/m³
 τ_w Shear stress on the port wall, Pa
 θ_w Angle measured, in a counter-clockwise direction, at the lower side of the propellant, degree

Subscripts

c Rocket chamber
 eff Effective
 g Gas
 i Initial value
 ign Ignition condition
 p Propellant (condensed phase)
 ps Propellant surface
 t Turbulent

Superscripts

$-$ Favre or mass-averaged quantity
 $-$ Reynolds or time-averaged quantity
 $"$ Fluctuating quantity in Favre averaging method

REFERENCES

1. Prentice, J. L., "Flashdown in Solid Propellants," U.S. Naval Ordnance Test Station, China Lake, Calif., NAVWEPS Report 7964, NORT TF 3009, Dec. 1962.
2. Prentice, J. L., "Combustion in Solid Propellant Grain Defects: A Study of Burning in Single- and Multi-Pore Charges," Naval Weapons Center, China Lake, Calif., NWC TM 3182, June 1977.
3. Margolin, A. D., and Margolin, V. M., "Penetration of Combustion into an Isolated Pore in an Explosive," Combustion, Explosion and Shock Waves, Vol. 5, No. 1, 1969, pp. 17-18.
4. Godai, T., "Flame Preparation into the Crack of Solid Propellant Grain," AIAA Journal, Vol. 8, No. 7, July 1970, pp. 1322-1327.
5. Bobylev, V. K., Margolin, A. D., and Chuiko, S. V., "The Mechanism by Which Combustion Products Penetrate into the Pores of a Charge of Explosive Material," Doklady Akademii Nauk USSR, Vol. 162, No. 2, May 1965, pp. 388-391.
6. Payne, C. E., "Flame Propagation in Propellant Cracks," AFRL-TR-69-66, Air Force Rocket Propulsion Laboratory, 1969.
7. Krasnov, Yu. K., Margolin, V. M., Margolin, A. D., and Fekhil, F. F., "Rate of Penetration of Combustion into the Pores of an Explosive Charge," Combustion, Explosion, and Shock Waves, Vol. 6, No. 3, 1970, pp. 262-265.
8. Belyaev, A. F., Korotkov, A. I., Sulimov, A. A., Sukyan, M. K., and Obmenin, A. V., "Development of Combustion in an Isolated Pore," Combustion, Explosion and Shock Waves, Vol. 5, No. 1, Jan.-March 1969, pp. 4-9.
9. Belyaev, A. F., Bobylev, V. K., Korotkov, A. I., Sulimov, A. A., and Chuiko, S. V., "Development of Burning in a Single Hole," Transition of Combustion of Condensed Systems to Detonation, Chap. 5, Part A, Section 22, Science Publisher, 1973, pp. 115-134.
10. Kuo, K. K., Chen, A. T., and Davis, T. R., "Convective Burning in Solid-Propellant Cracks," AIAA Journal, Vol. 16, No. 6, June 1978, pp. 600-607.
11. Kumar, M., and Kuo, K. K., "Flame Spreading and Combustion in Solid Propellant Cracks," Final Report to Naval Weapons Center, China Lake, Calif., July 1980.
12. Kumar, M., and Kuo, K. K., "Ignition of Solid Propellant Crack Tip Under Rapid Pressurization," AIAA Journal, Vol. 18, No. 7, July 1980, pp. 826-833.
13. Kumar, M., Kovacic, J. K., and Kuo, K. K., "Flame Preparation and Combustion Processes in Solid Propellant Cracks," AIAA Journal, May-June 1981 (to be published).

14. Kumar, M., and Kuo, K. K., "Effect of Propellant Deformation on Ignition and Combustion Processes in Solid Propellant Cracks," JANNAF Propulsion Systems Hazards Meeting, Monterey, Calif., Oct. 1980.
15. Kuo, K. K., Kovalcic, R. L., and Ackman, S. J., "Convective Burning in Isolated Solid Propellant Cracks," Naval Weapons Center, China Lake, Calif., NWC TR 6049, Feb. 1979.
16. Belvaev, A. F., Boholov, V. V., Korotkov, A. I., Sulimov, A. A., and Shulko, S. V., Transition from Deflagration to Detonation in Condensed Phases, translated from Russian by Israel Program of Scientific Translations, Jerusalem, 1975.
17. Bradley, H. H., Jr., and Boggs, T. L., "Convective Burning in Propellant Defects: A Literature Review," Naval Weapons Center, China Lake, Calif., NWC TR 6007, Feb. 1978.
18. Kovacic, S. M., "Improved Prediction of the Flame Spreading Process by Incorporating Tip Ignition and Turbulent Diffusion Effects into the Solid Propellant Crack Combustion Model," M.S. Thesis, The Pennsylvania State University, Nov. 1980.
19. Favre, A., "Equations des Gas Turbulents Compressibles," *J. de Mechanique*, Vol. 4, No. 3, 1965, pp. 261-280.
20. Feretz, A., Ku, K. K., Caveny, L. H., and Summerfield, M., "Starting Transient of Solid-Propellant Rocket Motors with High Internal Gas Velocities," *AIAA Journal*, Vol. 11, Nov. 12, Dec. 1973, pp. 1717-1727.
21. Svehla, R. A., "Estimated Viscosities and Thermal Conductivities of Gases at High Temperatures," *NASA TR R-132*, 1962.
22. Goldsmith, C. E., "Turbulent Flow in Pipes with Particular Reference to the Transition Region Between the Smooth and Rough Pipe Laws," *Journal of the Institute of Civil Engineers*, Vol. II, 1935-39, pp. 133-156.
23. Schlichting, H., "Turbulent Flow Through Pipes," *Boundary Layer Theory*, 6th Ed., McGraw-Hill, New York, 1968.
24. Barrere, M., Jaumotte, A., Deloche, R. F., and Vandenberghhe, J., *Rocket Propulsion*, Elsevier Publishing Co., New York, 1960, p. 195.
25. Lenior, J. M., and Robillard, G., "A Mathematical Method to Predict the Effects of Erosive Burning in Solid Propellant Rockets," *1st Symposium International on Combustion*, The Combustion Institute, Pittsburgh, PA, 1956, pp. 563-587.
26. Rubinek, W., and Fung, K. K., "Measurements and Model Validation for Composite Propellants Burning under Cross Flow of Oxides," *AIAA Journal*, Vol. 17, No. 1, June 1979, pp. 1-12.
27. Charent, A. F., Dewey, J. R., Jones, J. H., and Hitz, J. A., "An Investigation of Separated Flows Part III. Flow in the Gravity and Heat Transfer," *Journal of the Aerospace Sciences*, Vol. 28, No. 7, July 1961, pp. 514-527.
28. Coull, D. J., and East, L. F., "Three-Dimensional Flow in Combustion," *Journal of Fluid Mechanics*, Vol. 16, 1963, pp. 179-203.
29. Kuo, K. K., Chen, A. T., Savel, T. R., "Transient Flame Propagation and Combustion Processes Inside a Solid Propellant Crack," *AIAA Paper 77-118*, AIAA 15th Aerospace Sciences Meeting, January 1977.

THIS PAGE IS BEST QUALITY PRACTICABLE
FROM COPY FURNISHED TO DDC

Flame Propagation and Combustion Processes in Solid Propellant Cracks

Mridul Kumar,* Stephen M. Kovacic,† and Kenneth K. Kuot
The Pennsylvania State University, University Park, Penn.

The effects of pressurization rate, crack-gap width, crack length, and propellant type on the ignition and flame-spreading processes in isolated AP-based solid propellant cracks have been studied experimentally. Ignition front propagation rates were measured using a high-speed (up to 44,000 pictures/s) camera. Cracks up to 200 mm in length with gap widths as low as 450 μm were studied. It was observed that the hot gases precede the ignition front. The ignition-front propagation speed increases near the crack entrance, reaches a maximum, and then decreases near the crack tip. The results of parametric study indicate that the time required for the ignition front to reach the crack tip decreases, and that the maximum velocity of the ignition front increases as the pressurization rate or burning rate of the propellant is increased. The maximum pressure in the crack increases with an increase in burning rate or crack length, but decreases with an increase in gap width.

Nomenclature

a	= pre-exponential factor in Saint Robert's burning rate relationship aP^n , (mm/s)/(atm) ⁿ
An	= Andreev number, $r_0 d_0 / \alpha$
d_0	= hydraulic diameter of crack, mm
L	= length of crack, mm
n	= pressure exponent in Saint Robert's burning rate relationship
P	= pressure, atm
P_{\max}	= maximum pressure in the crack cavity, atm
r_0	= burning rate of solid propellant, mm/s
T	= temperature, K
t	= time, s
T_f	= adiabatic flame temperature of solid propellant, K
T_{f0}	= initial propellant temperature, 295 K
v_{cr}	= convective ignition front propagation velocity, m/s
x	= axial location, measured from entrance of crack, mm
α	= thermal diffusivity
δ	= gap width of crack
ρ	= density, kg/m ³

Introduction

UNDER certain operating conditions, high-pressure and high-temperature gases from the rocket chamber penetrate the defects or cracks that are present in solid propellants. The convective heat transfer from the hot gases heats the propellants along the cracks, and if a sufficient amount of energy is transferred to the propellants, ignition also occurs inside the defects. Burning inside defects or cavities may result in much higher pressures in the cavities; indeed, it is believed that given the proper stimuli, these defects or multiple cracks may initiate detonation. Even if this abnormal burning does not lead to a catastrophic failure, it may cause the performance of the rocket motor to deviate significantly from the designed conditions.

Presented as Paper 80-1206 at the AIAA/SAB/ASME 16th Joint Propulsion Conference, Hartford, Conn., June 30-July 2, 1980; submitted July 31, 1980; revision received Dec. 22, 1980. Copyright © American Institute of Aeronautics and Astronautics, Inc., 1980. All rights reserved.

*Assistant Professor, Department of Mechanical Engineering, Member AIAA.

†Graduate Student, presently working at TRW Ballistic Missiles Division, San Bernardino, Calif.

‡Associate Professor, Department of Mechanical Engineering, Associate Fellow AIAA.

This paper deals with a detailed experimental investigation of the development of convective burning in an isolated propellant crack. Convective burning is defined as enhanced burning of a propellant charge, caused by hot gas penetration into propellant defects. Forced convection is the primary heat transfer mechanism during convective burning. Even though the ignition, flame spreading, and combustion processes inside an isolated solid propellant crack represent an idealized case of the actual burning in propellant defects, a fundamental understanding of the ignition and flame-propagation processes in such a geometry is essential in order to study the extremely complex phenomenon of ignition in defects, leading to deflagration-to-detonation transition (DDT). It should be noted, however, that a single crack will result in a limited increase in burning surface area, and, therefore, may not cause detonation.

Prior to this study several researchers have investigated convective burning in solid propellant defects. Recently, Bradley and Boggs¹ have made an extensive literature review on convective burning in propellant defects. Belyaev et al.² have compiled most of the recent work done in this area in the USSR. These reviews indicate that the convective burning in solid propellant cracks has been investigated by a number of researchers in the past and that both theoretical and experimental techniques have been used. Studies in this area have also been conducted at The Pennsylvania State University.³⁻⁷ Experimental studies on convective burning in solid propellant cracks can be subdivided into two broad categories^{1,2}: 1) onset of convective burning, and 2) development of convective burning. Literature on the onset of convective burning is extensive; the studies are usually qualitative in nature and are characterized by tests of the go/no-go type. Results of studies on the onset of combustion are commonly presented in graphical form to indicate the operating conditions (usually pressure) under which the flame will penetrate a crack of a given dimension. The following paragraphs list some of the important work in this area.

Prentice⁸ conducted experimental investigations on the onset of convective burning in a transparent, nitrocellulose-petrin propellant. He observed that it was much easier to flashdown into a crack with both ends open than into a crack with one end closed. Catalytic additives caused flashdown to occur more readily. Flashdown was not observed up to 3.9 MPa in 1.6-mm-diam cracks. Both motion pictures and thermocouples were used to monitor flame penetration. Later, Prentice⁹ extended his work to opaque composite propellants. Vibration response spectroscopy (VRS) was used to monitor flashdown. Double-based propellants that displayed mesa burning were also investigated by Prentice. He

concluded that the critical pore diameter for flashback in a given propellant is inversely proportional to the burning rate. Margolin and Margolis¹⁰ noted that combustion penetrates more easily into a channel with two open ends than into a blind channel. They also observed that if the channel were open at one end, or if there were one or more outlets from the channel to the burning surface, the combustion gases instantaneously penetrated the pores when the Andreev number (A_n) was beyond a critical value. However, the critical Andreev number is not always constant.

Godai¹¹ made experimental investigations of flame propagation in the narrow slit and fine hole of solid propellant grain. Cracks of 22 mm in length were formed with 5 mm square slabs of AP-based composite propellants. The propellant was ignited with a nichrome wire, and the ignition event was filmed by motion-picture camera at a rate of about 32 frames/s. Tests were conducted in a slab of propellant with both a single hole and multiple holes. Godai observed that there is a threshold gap width or hole diameter below which the flame does not propagate into the defect, and that the threshold crack gap is fundamentally a function of the burning rate. Bobolev et al.,¹² Payne,¹³ and Krasnov et al.¹⁴ also studied the onset of convective burning in solid propellant cracks.

Experimental studies on the development of convective burning are limited. Belyaev et al.^{15,16} made preliminary investigations of the development of combustion in single pores. The flame propagation rate was observed to increase initially, and then to reach a constant value. The pressure in the crack was found to be greater than that of the chamber, and the effect of erosive burning was found to be important. The maximum pressure in the crack was correlated with the crack length and the ratio of the crack length to crack width.

The focus of previous investigations of combustion in propellant cracks has been on the onset of convective burning; the development of convective burning has yet to be investigated fully. It is generally believed that the development of convective burning in a propellant defect is a necessary condition for subsequent transition to detonation. Almost all of the previous studies have been conducted at constant pressure conditions. The effect of chamber pressurization rate (dP/dt) on flame propagation, which is of interest in actual rocket motor and DDT studies, has not yet been investigated.

The aim of the present research was to narrow some of the technological gaps that exist in the study of the development of convective burning in solid propellant cracks. The specific objectives of this investigation are:

1) To experimentally study the effect of the following parameters on ignition and flame propagation inside Ammonium-Perchlorate-based composite solid propellant cracks: a) chamber pressurization rate, b) crack gap width, c) length of the crack, and d) propellant composition.

2) To establish a data base for the convective flame-propagation rate and the maximum pressure in the crack cavity as a function of pressurization rate, crack geometry, and the physicochemical properties of the propellant.

The results of this study can also be used for verification purposes, in order to compare the flame-propagation rates and pressure measurements along axial locations of the crack, with the numerical predictions of a parallel theoretical study being conducted by the authors at The Pennsylvania State University.

Experimental Setup and Procedures

Test Apparatus

The test apparatus and experimental conditions for this study incorporated the following major design considerations: 1) the test apparatus should allow a wide range of variation in crack geometry and operating conditions; and 2) test conditions should simulate, as closely as possible, those in an actual rocket motor. A solid propellant igniter system (details of which are given in the following section) was used

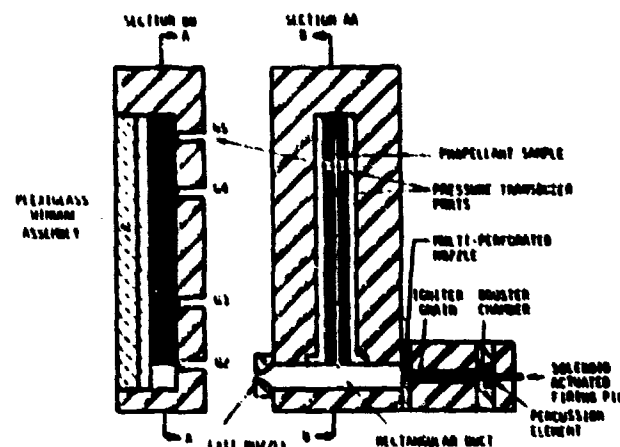


Fig. 1 Schematic diagram of combustion chamber.

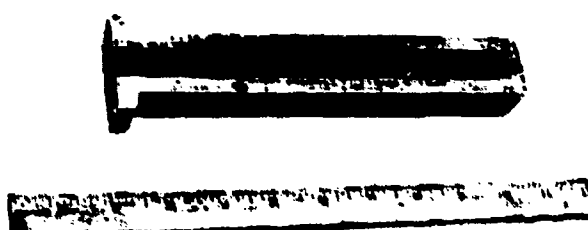


Fig. 2 Typical propellant crack sample.

to simulate igniter gas composition similar to that in an actual rocket motor. Using this igniter system, it was possible to obtain pressures up to 200 atm in the chamber in approximately 2 ms. The test apparatus is also compatible with the theoretical model developed by the authors^{3,17} and, therefore, the results obtained here could later be used for model validation.

Igniter System

A solid propellant igniter system was the source for hot gas generation. Percussion primers were used as initiators for ignition of a propellant charge. A remotely controlled, solenoid-activated firing pin was used to trigger the primer. A schematic diagram of the test chamber and igniter system is shown in Fig. 1. The igniter system consists of 1) a solenoid mounted on the retainer block of a spring-loaded firing pin, 2) a percussion element and its housing unit, 3) a propellant igniter charge and igniter chamber, and 4) a multiperforated nozzle plate. All hardware was made of stainless steel.

High-temperature, high-velocity gases, under rapidly increasing pressure conditions that simulate flow conditions in a rocket chamber, were obtained by burning a 50 mm long, rectangular cross-sectional ($\sim 5.7 \times 5.7$ mm) solid propellant charge. This charge was placed inside the cavity of the igniter chamber; the diameter of the cavity is 8 mm. When the primer was triggered, it produced hot gases which flowed over and ignited the solid propellant charge. The product gases flowed through a multiperforated converging nozzle into the main chamber. The pressurization rate of the chamber can be varied by altering the dimensions of the propellant strip in the igniter, by changing the dimensions of the multiperforated nozzle, or by changing the exit nozzle of the chamber.

Test Chamber and Crack Configurations

The test chamber shown in Fig. 1 was made of stainless steel 304. The discharge of the igniter system passes through a 124 mm long, rectangular cross-sectional (10×25.4 mm) channel. The propellant crack sample is placed perpendicular

to the flow direction in the main chamber. Cracks were formed by cutting a slot of desired width in a propellant slab (of 25.4×17 mm cross section) glued into a brass retainer. It was possible to manufacture cracks up to 210 mm in length, with gap widths as low as 450 μm . Figure 2 shows a typical propellant crack sample. Four pressure ports were provided along the center of the crack in order to measure pressure variation along the crack. An interchangeable, convergent exit nozzle was used to vary pressure and flow conditions in the chamber. The nozzle was made of titanium in order to alleviate the problem of metal erosion caused by highly corrosive gases. The exit diameter of the nozzle was varied between 2.5 and 3.8 mm. For safety, the chamber was also equipped with a port for a burst diaphragm. If for any reason pressure inside the chamber exceeded a predetermined value (usually 680 atm), the burst diaphragm would rupture to vent pressure and avoid an explosion.

Flame propagation in the crack was observed through a set of transparent plexiglass windows. The window assembly consisted of a sacrificial window ($238 \times 65 \times 6.3$ mm) and a viewing window ($251 \times 78 \times 25.4$ mm). The window assembly was held in place by a stainless steel window retainer. To achieve a good seal, rubber O-rings were used between the two halves of the chamber, and between the inlet and exit nozzles and the chamber. During the tests, the chamber was completely sealed, except for the interchangeable exit nozzle through which product gases were discharged into the atmosphere. Since the sacrificial window is placed directly over the propellant surface, it is destroyed after each test firing. The test sample is clearly visible through the windows during the test.

To obtain a more detailed observation of the flame-front propagation, an alternative crack sample shown in Fig. 3 was used to replace the one shown in Fig. 2. The alternative crack sample provided direct (front view) observation of the gas penetration and ignition-front propagation processes. In this configuration, the crack was formed between a propellant slab and the sacrificial plexiglass window, i.e., one side of the crack was an inert, transparent, plexiglass window and the other side was a propellant slab glued to a stainless steel base plate. The gap width of such a crack configuration is varied by the amount by which the propellant surface is recessed below the side-leg assembly (see Fig. 3). The propellant slabs for these tests were 183 mm long and 17.7 mm wide. Gap widths of the crack were varied between 0.43 and 1.5 mm. It should be noted that for this configuration only two pressure traces can be obtained: one at the crack entrance, and the other at the tip.

Instrumentation

Data Acquisition System

A block diagram of the data acquisition system for the convective flame propagation studies is shown in Fig. 4. The data acquisition system consists of three major parts: 1) pressure measuring system, 2) flame propagation measuring system, and 3) transient waveform recording system. Details of measurement techniques are given in the following sections. The data acquisition system includes: pressure transducers, charge amplifiers, a high-speed movie camera, a light-emitting diode (LED) driving unit, a motion analyzer, a 9-channel transient waveform recorder (Physical Data Model #515-234), a 7-channel FM tape recorder, an oscilloscope and an x-y plotter. The maximum sampling rate of the Physical Data System is 2×10^6 samples/s, and the maximum amplitude resolution is 0.1% with a 4096 word memory per channel. The recording speed of the HP type recorder is 60 in./s at a carrier frequency of 104 kHz. The tape can be played back at a much lower speed (1 in./s) to expand the duration of the transient signals. Data recorded on the Physical Data System can be displayed on an oscilloscope, or plotted on an x-y plotter for a hard copy. Data recorded on tape is digitized before display or plotting.

Fig. 3 Propellant sample for detailed observation of ignition front.

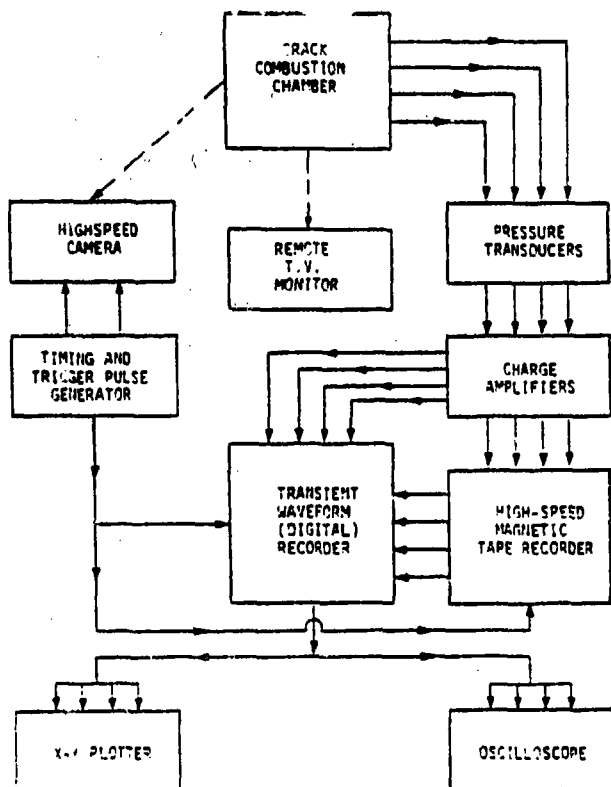


Fig. 4 Block diagram of data acquisition system.

Pressure Measurements

Four ports are provided along the length of the crack for transient pressure measurements. The first port is located in the main chamber, very close to the crack entrance. The other three are located at 48, 138, and 188 mm from the first transducer port. Piezoelectric quartz transducers were used to measure the pressure. The transducers have a rise time of 1.5 μs and a natural frequency of 300 kHz, and can accurately record pressures up to 1000 atm. The transducers were mounted in a water-cooled adapter that prevented drifting or damage due to excessive heat. In addition, a thin layer of silicon rubber insulation was placed on the transducer surface to further protect the transducer diaphragm from high-temperature gases. The transducers were mounted about 2 mm below the bottom surface of the chamber.

Charge signals from the pressure transducers were carried through an insulated, high-impedance, coaxial cable to a charge amplifier. The output (voltage signal) of the charge amplifiers was recorded simultaneously on the transient waveform recorder and on the magnetic tape. In order to accurately determine the pressure level, calibration signals equivalent to 69 atm (1000 psig) were also recorded for each channel. Calibration signals for each transducer were checked periodically by comparing them with signals obtained from measuring a known pressure of a high-pressure nitrogen or air tank.

Flame-Propagation Measurements

A high-speed, 16 mm motion picture camera was used to observe the complete ignition event in the chamber. With a quarter-frame optical head, the camera was capable of filming at a maximum of about 44,000 pictures/s. The Hycam camera is equipped with a dual light-emitting diode (LED) system; one LED records timing marks and the other records a common-time signal on the film. The common-time signal is generated at the start of the event, and is used to correlate events recorded on the transient waveform recorder or tape with those on the film. The LED driver unit, a common-time pulse and high-frequency (up to 10 kHz) timing generator, was used to operate the LED time system. The frequency of the timing pulse in the present investigation was set at 1 or 10 kHz.

The Vanguard motion analyzer was used to analyze the film, frame by frame. The motion analyzer screen is equipped with two cross hairs to traverse in two perpendicular directions in a plane. Two micrometer dials, accurate to a thousandth of an inch, are used to record the movement of the cross hairs. The analyzer's frame counter is designed to keep track of the number of frames analyzed. In order to obtain the flame-propagation speed for a fixed y location (centerline of the crack), x readings (along the crack) were taken for each frame until the flame reached the crack tip. Readings of the micrometer dials were scaled by using the known value of the initial length of the crack and the total distance traversed by the crosswire. The time interval between each picture was obtained from the time marks on the film.

Remotely Controlled Ignition Circuit

The transient ignition processes in a solid propellant crack involve high pressures and very high pressurization rates ($\sim 10^5$ atm/s). Because pressurization rates of such a magnitude are potentially hazardous, experiments were carried out in a test cell with 1½-ft thick concrete walls, and the ignition event was remotely controlled.

A block diagram of the remotely controlled ignition and high-speed photography system is shown in Fig. 5. The solenoid that triggers the percussion primer is activated by an event switch built into the high-speed camera. After the camera is switched on, about one second is required to reach the desired framing rate. This delay time can be related to the footage of the film that passes through the camera before the

attainment of the prescribed framing rate. The event switch is controlled by a footage indicator. During operation, the footage indicator is set to a preselected value corresponding to the desired framing rate. For example, the indicator is set at 100 ft for a framing rate of 40,000 pictures/s. After a specified length of film (preset on the footage indicator) passes through the camera, the event switch closes, causing 12 V ac to be applied across the relay, and the relay is activated. The relay, in turn, activates two other switches; one switch triggers the solenoid (by causing a current to flow through it) and initiates the ignition event, and the other closes the common-time switch on a light-emitting-diode (LED) driver unit. At the instant at which the common-time switch closes, the LED driver unit generates a 2 ms pulse that is recorded on the transient waveform recorders and is simultaneously marked on the film. These common-time marks are used for time correlation of the data recorded on the tape and film.

Test Procedure

Test samples were prepared from cast propellant grains obtained from propellant processing laboratories. Propellant slabs (approximately $215 \times 26 \times 17$ mm) were cut from the cast propellant with a remotely controlled milling machine. A slightly oversized propellant slab was glued into a brass retainer. The sample was left to dry for 24 h in order to achieve a good adhesive bond between the propellant and the brass retainer. The sample was machined again to the desired dimensions. A crack of the desired dimension was then precisely cut through the center of the crack sample with a jeweler's slitting saw. Propellant samples for the alternative configuration (for detailed flame-front observation) were obtained in a similar manner. Oversized propellant slabs were glued onto a steel plate and machined to the desired dimensions. The entrance region of the crack was rounded slightly to ensure smooth flow development inside the crack. After machining, the samples were carefully cleaned with a high-pressure air jet to remove any loose particles in the crack cavity.

During assembly of the test chamber, a part of the propellant side surface in contact with the sacrificial plexiglass window and the combustion chamber was coated with a thin layer of flame retardant to help prevent the flame from penetrating between the propellant and the contact surfaces. A layer of rubber-based adhesive sealant was applied to all contact surfaces of the various components of the test chamber to prevent leaks during experiments. After the crack sample was mounted into the crack combustion chamber, the crack geometry was carefully measured and recorded. High-intensity camera lights were used during the test to facilitate motion-picture recording. In order to observe the ignition event remotely and to detect possible leaks during the test, a video monitor with a TV camera was used.

Results and Discussion

Four types of AP-based composite solid propellants were used in this investigation. Table I lists the propellants and some of their properties. Propellants A and B have almost identical pressure exponents in the Saint-Robert's burning rate relationship; however, propellant A has a higher burning rate since it has a larger pre-exponential factor. Propellant B (AP/MBAE-EPOM) was used in most of the tests. Propellants C and D have identical binder (HTPB) and oxidizer weight fractions (73%); however, the oxidizer particle size in propellant C is 20 μm , whereas the oxidizer particle size in propellant D is 200 μm . The effect of oxidizer particle size on the ignition and flame propagation processes can be obtained from a comparison of the results of these two propellants.

The physical processes that take place during the test can be described generally as follows. Discharge of product gases from the igniter system pressurizes the test chamber, causing hot ignition gases to penetrate the crack cavity. The pressure-wave fronts move along the crack, and the hot gases transfer

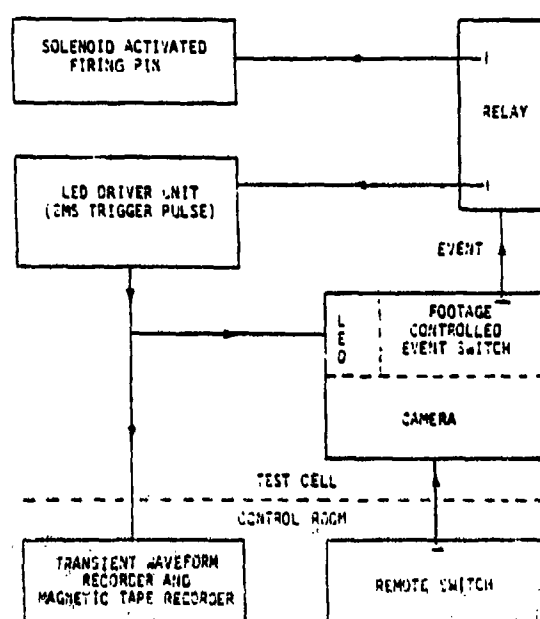


Fig. 5 Block diagram of remotely controlled ignition and photography system.

Table I Propellant properties

Propellant type	A	B	C	D
Composition	AP-based	AP/PBAA-EPON	AP/HTPB	AP/HTPB
Weight percent of oxidizer	75	75	75	75
Average particle size d_{AP} , μm	76	76	20	200
Pre-exponential factor in Saint Robert's burning rate expression a , $\text{mm}^2/\text{s}/(\text{atm})^n$	1.62	0.9391	0.8441	0.5849
Pressure exponent in Saint Robert's burning rate expression, n	0.4108	0.41	0.5611	0.5427
Flame temperature T_f , K	3000	1920	1667	1667
Propellant density, kg/m^3	1710	1600	1492	1492

* AP weight percent and particle size for propellant A not available to the authors.

heat to the crack surface, resulting in an increase in propellant surface temperature. As the pressure in the chamber continues to increase, more hot gases are driven into the crack, and there is also an increase in the convective heat-transfer rate. Eventually, the ignition condition is realized, and the propellant begins to burn. Following the flame-spreading period, the gasification of the crack surface may generate a pressure higher than that in the chamber. Finally, the gases flow out of the crack into the main chamber.

As mentioned in the section on instrumentation, pressure measurements were made at four axial locations along the crack. The ignition-front propagation speed was deduced from films of the flame-front propagation made by a high-speed camera. Because of the complexity involved with accurate quantitative measurement of temperature for highly transient flow situations, no attempt was made to measure the temperature in the crack. (The time required for the flame to propagate from the crack entrance to the crack tip was less than 1 ms in most cases.) High gas temperatures also make this kind of measurement difficult. In all test firings the initial pressure in the crack chamber was 1 atm, and the initial temperature of the propellant was about 295 K. Results of pressure and flame-propagation measurements are discussed next, followed by results of the parametric study.

A typical set of time-correlated pressure traces is shown in Fig. 6. In this figure a dual time base is used to obtain maximum information in one plot. The initial portions of the $P-t$ traces have been expanded to illustrate the pressurization processes at various locations along the crack. Gage G2 is located at the crack entrance, and G5 near the crack tip. The qualitative nature of the curves is similar, with the following important differences: 1) the first discernible pressure rise for each pressure gage occurred consecutively from the crack entrance to the crack tip, i.e., from G2 to G5; 2) the pressurization rate increased consecutively downstream from the crack entrance; and 3) the maximum pressure occurred in the interior of the crack. The time delay between the first discernible pressure rise at downstream locations and that at the crack entrance is caused by the finite time required for the hot product gases to travel from the entrance to the tip during initial pressurization. The increase in pressurization rate at downstream locations is caused by the coalescence of the traveling pressure waves. This can be further explained by noting that as the igniter is discharged, the pressure of the chamber rises, causing weak pressure waves to travel downstream of the crack. As the pressure waves travel down the crack, they are followed by stronger pressure waves caused by rapidly increasing pressure in the chamber. At the same time, some of the propellant in the upstream region begins to gasify, thus creating higher pressure behind the pressure front. The result of the combined effect of the high pressure regions behind the front is a steepening of the pressure front as it moves downstream.

The pressure trace at any location can be subdivided into three regions: 1) the initial rapid pressurization region, which is controlled mainly by chamber conditions; 2) the slowly rising pressure region; and 3) the depressurization region. The initial uprising portion of the pressure-time trace is quite

linear. In most cases, the flame reaches the crack tip during the initial uprising portion of pressure-time trace at the tip. Pressure in regions 2 and 3 is controlled by combustion and flow processes in the crack. As the burning of the propellant in the crack continues, the pressure in the cavity rises above that at the crack opening; later, this pressure difference causes the gases to flow out of the crack. Pressure in the crack continues to rise until the mass flow rate of the gases from the crack is greater than that generated by the burning of the propellant in the cavity. Since the pressure in this region is governed by combustion processes inside the crack, and because gage G2 is located at the crack opening in the main chamber, the highest peak pressure occurs in the interior of the crack. Depressurization is caused by the increase in crack cavity volume, as well as by the enlargement of the crack opening, but the burning surface area remains constant.

The common-time signal, which is used to correlate pressure measurement and film, is not shown in Fig. 6 because of the 10-12 ms time lag between the common-time signal and first discernible pressure rise at the crack entrance location. In order to include the common-time signal, pressure-time traces would have to be compressed substantially, which is not desirable. The time-correlated pressure and ignition data

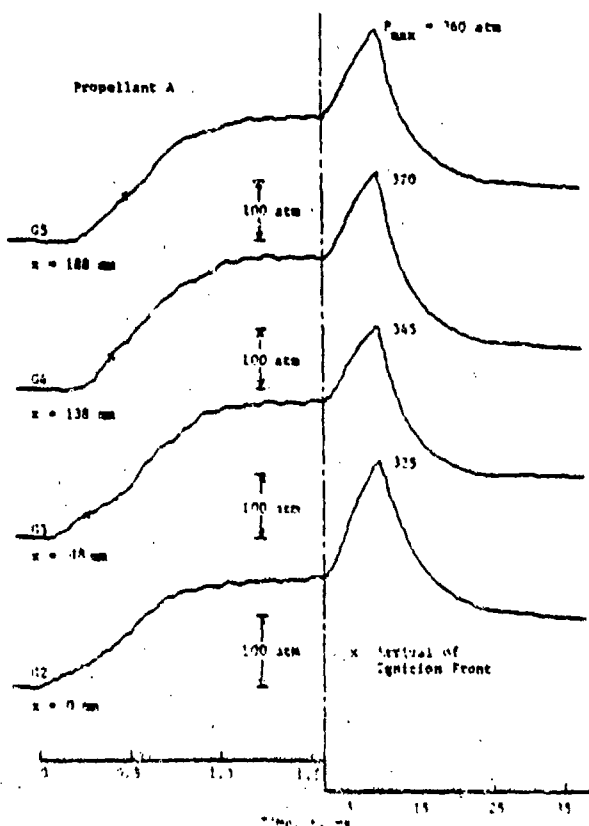


Fig. 6 Measured pressure-time traces.

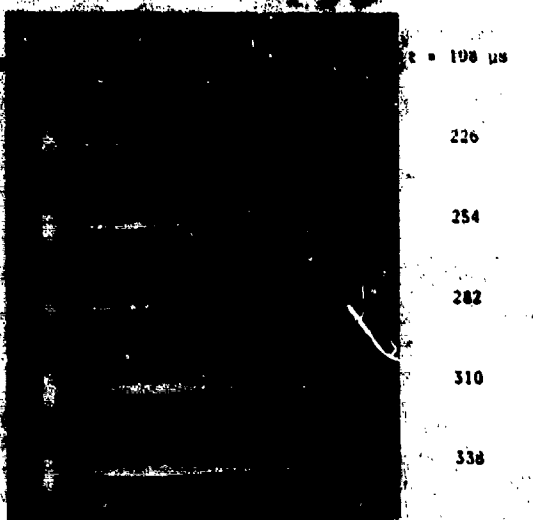


Fig. 7 Photographs of ignition front location for a typical crack test.

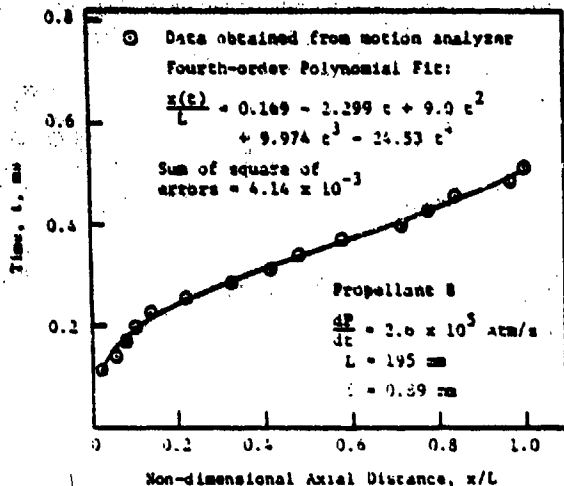


Fig. 8 Least-squares polynomial fit to measured ignition front location vs time data.

indicate that the appearance of hot igniter gases at the crack entrance coincides with the first discernible pressure rise at that point. Therefore, the initial time $t=0$ in this study can be defined as either the first discernible pressure rise at the crack entrance location, or the first appearance of hot gases on the film.

Figure 7 shows typical continuous photographs of the ignition-front propagation in a crack. The instantaneous location of the ignition front x was obtained by analyzing the film of the ignition event on a motion-picture analyzer, as discussed in the last section. The time marks on the film were used to determine the time t corresponding to each reading. A least-squares polynomial was fitted to the $x-t$ data, and an analytic derivative of this curve was used to obtain the ignition-front propagation rate ($v_{if} = dx/dt$). This procedure made it possible to obtain flame-propagation rates from the measured ignition-front locations. Polynomials between the third and fifth order were used, and the polynomial with the best fit was chosen to represent the analytic function relating the instantaneous flame-front location to time. Figure 8 shows a typical fourth-order polynomial fit to the measured ignition-front location vs time data. As can be seen from this figure, the curve fits the data quite well. The sum of the square of errors for this polynomial fit is 4.14×10^{-3} . In this paper, the remainder of the figures of ignition-front location vs axial distance show only the fitted polynomial. Errors are of the same order as that given in Fig. 6.

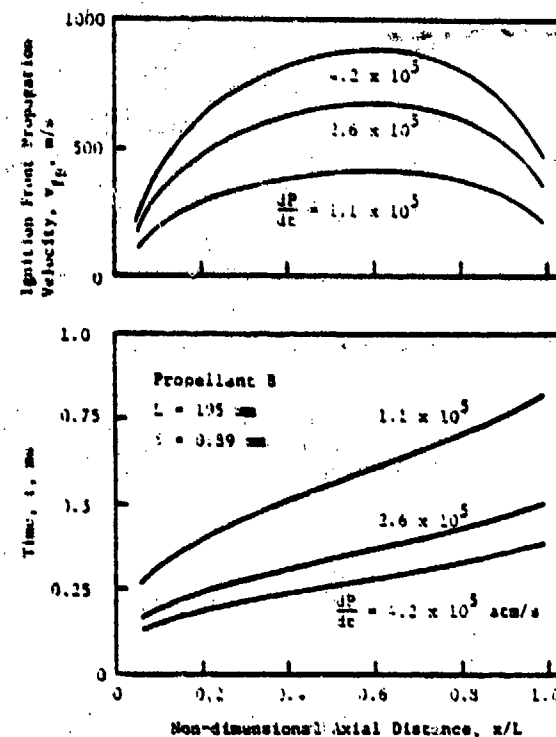


Fig. 9 Effect of pressurization rate on measured ignition front propagation.

The effect of chamber-pressurization rate on location and velocity of the ignition front for propellant B is shown in Fig. 9. The crack specimen was 195 mm long, and the gap width was 0.89 mm. The time for the flame to propagate to a given axial location and the velocity of the ignition front at that location are plotted as a function of the nondimensional axial coordinate for pressurization rates of 1.1×10^3 , 2.6×10^3 , and 4.2×10^3 atm/s. The time required for the flame to reach the crack tip is 836, 511, and 391 μ s, respectively. That is, as the chamber pressurization rate increases, the ignition front propagates much more quickly into the crack because the rapidly increasing pressure in the chamber acts as the driving force for the penetration of hot gases into the crack. This higher pressurization causes an increase in the velocity of the gas flowing into the crack, and results in a higher rate of heat transfer to the crack walls. Faster ignition-front propagation is a net effect of these conditions. It should be noted that because of the presence of bright gases near the crack entrance, it is extremely difficult to identify the time at which the ignition front at the crack opening first appears. This explains why the plots do not show data near $x=0$.

It is interesting to note that the nature of the curves is the same in all three cases. By extrapolating the time vs axial location curve to $x=0$, the time lag between the arrival of hot gases in the chamber and the initiation of the ignition front near the crack entrance is evident. The time lag decreases as the pressurization rate is increased. The ignition-front velocity vs the nondimensional axial coordinate curve shows that after the ignition front is created near the crack entrance, it accelerates, reaches a maximum, and then decelerates. This deceleration near the closed end is more pronounced with a higher pressurization rate. At a low pressurization rate, the velocity remains relatively uniform over the bulk of the crack length. Initial acceleration is caused by the preheating by the hot gases that precede the ignition front. Deceleration is believed to be caused by the end effects. Deceleration of the ignition front is in agreement with the observation made by Taylor¹¹ concerning ignition of granular propellants with a closed-end boundary. Maximum ignition-front propagation velocities are 410, 673, and 886 m/s for the pressurization rates of 1.1×10^3 , 2.6×10^3 , and 4.2×10^3 atm/s, respectively.

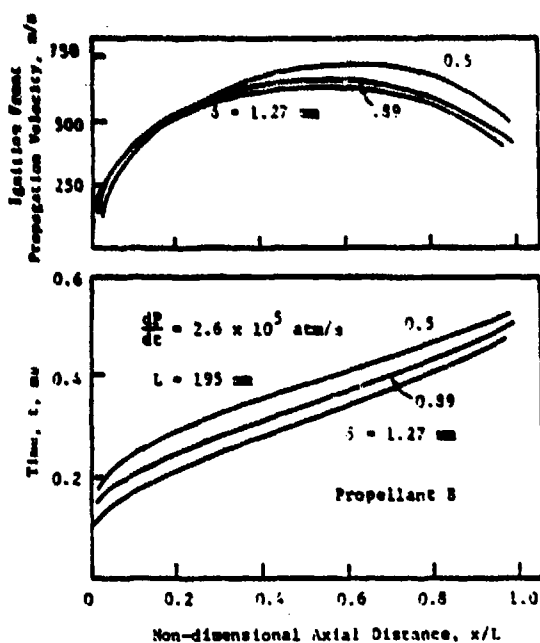


Fig. 10 Effect of gap width on measured ignition front propagation.

tively. It is important to note that the effect of dP/dt , as depicted in Fig. 9, is valid only for the range of values indicated. As observed earlier by the authors,⁶ under very high dP/dt conditions the crack tip may ignite before the ignition front propagates to the tip.

The effect of gap width on instantaneous location and velocity of the ignition front for propellant B is shown in Fig. 10. The length of the crack is 195 mm, and the crack-gap widths are 0.508, 0.889, and 1.27 mm. As the crack-gap width is increased, the ignition front penetrates the crack more quickly and reaches the tip sooner because the larger gap width offers less resistance to the penetration of the flow into the cavity. However, maximum velocity increases as the gap width decreases. This may be explained as follows. Since the time delay required for the ignition front to establish itself near the crack entrance is longer for cracks with smaller gap widths, the preheating effect caused by convective heat transfer is more pronounced. Once gasification begins, pressure behind the ignition front (due to gasification) will also be higher in narrow cracks. It is believed that the combined effect of preheating and higher pressure causes the ignition front to accelerate relatively rapidly in narrow cracks.

Figure 11 shows the effect of gap width on maximum pressure within the crack cavity. It is clear that as the gap width decreases, the maximum pressure in the cavity increases. As discussed earlier, maximum pressure in the crack cavity is determined by ignition and combustion processes inside the crack. Since crack depths are identical for all samples (25.4 mm), burning surface areas will also be identical as long as crack lengths for all samples are the same. As gap width is decreased, the burning surface area remains constant, but the opening area of the crack and volume of the crack gap decrease; therefore, maximum pressure is higher for smaller gap widths.

The effect of the burning rate on ignition-front propagation was studied by comparing results of tests conducted on propellants C and D as shown in Fig. 12. The initial crack length and gap width were 195 and 0.89 mm, respectively; the initial chamber pressurization rate was 3.2×10^3 atm/s. This comparison shows that the ignition-front propagation rate is faster for propellant C with its higher burning rate (AP particle size ~20 μm), than it is for propellant D with its lower burning rate (AP particle size ~200 μm). In these tests the effect of surface roughness was somewhat suppressed during the ignition-front propagation period because of the

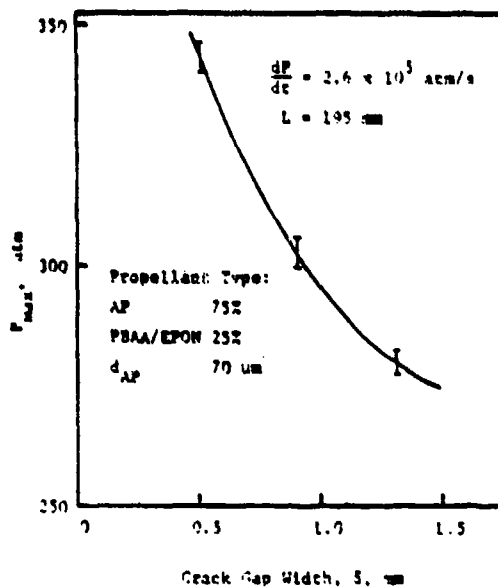


Fig. 11 Effect of gap width on maximum pressure in the crack.

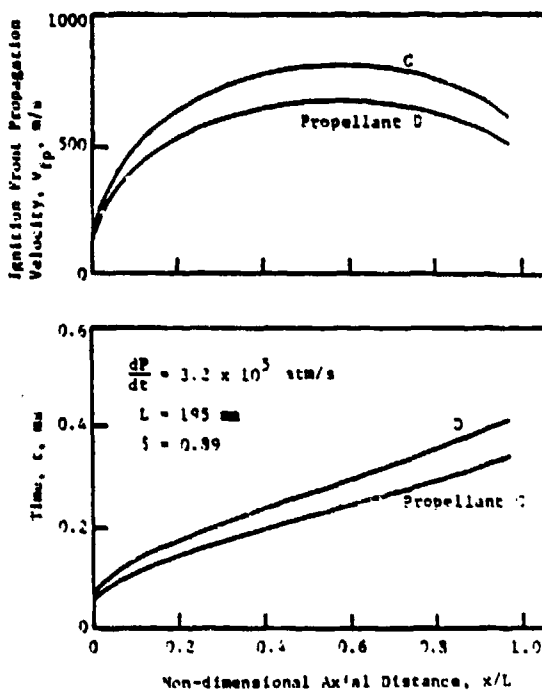


Fig. 12 Effect of burning rate on measured ignition front propagation.

fact that surfaces were machined. The rate of flame propagation for a propellant with a higher burning rate is faster because the high burning rate produces more gases behind the ignition front and causes the local pressure gradient near the front to increase.

The effect of propellant type was investigated further by comparing the results of high-energy propellant A with those of propellant B. Even though both are AP-based propellants, the flame temperature and burning rate of propellant A are much higher than those of propellant B. Figure 13 shows a comparison of the ignition-front propagation rates of the two propellants. The crack samples were 195 mm long, with a gap width of 0.89 mm. The initial chamber pressurization rate was 3.2×10^3 atm/s. The more energetic propellant A has a shorter flame-spreading period and a higher maximum ignition-front velocity. Besides having a higher burning rate,

Table 2 Effect of propellant burning rate on P_{max}

Propellant	Burning rate at 150 atm,	P_{max} atm
	mm/s	atm
B	7.5	322
D	8.9	334
C	12.7	354
A	14.0	371

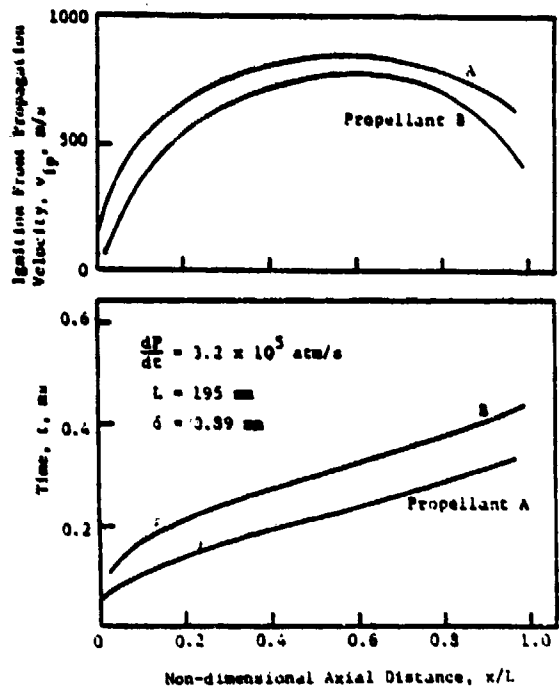


Fig. 13 Effect of propellant type on measured ignition front propagation.

the product gases generated from propellant A also have a higher temperature which further facilitates the ignition-front propagation process. Table 2 shows the effect of propellant burning rate on maximum pressure in the cavity. As the burning rate is increased, the maximum pressure in the crack also increases because higher burning rate propellants generate more gases, and for cracks of identical initial length and width (i.e., same initial volume of the crack cavity), this results in higher pressure.

Figure 14 shows the effect of crack length on ignition-front velocity. Propellant B was used in these tests, and the gap width was kept constant at 0.89 mm. The crack lengths were 65, 130, and 195 mm. As the crack length is increased, the time required for the ignition front to reach the crack tip increases, and the average ignition-front propagation velocity also increases. The times required for reaching the tip are 252, 476, and 511 μ s, and the maximum ignition-front velocities are 435, 530, and 675 m/s for crack lengths of 65, 130, and 195 mm, respectively. Maximum pressure in the crack also increases as the crack length is increased. Higher flame-propagation velocities for longer cracks are the result of the reduced end effects which allows the flame front to accelerate. The ignition delay near the entrance portion of the crack is greater, however, for longer cracks. This may be the result of crack entrance deformation caused by pressure exerted on the front end of the crack sample. In general, these observations are in agreement with the limited data reported by Bobolev et al.¹²

In order to observe hot gas penetration and ignition-front propagation processes in detail, experiments were conducted using the alternate crack configuration (see Fig. 3). Figure 15

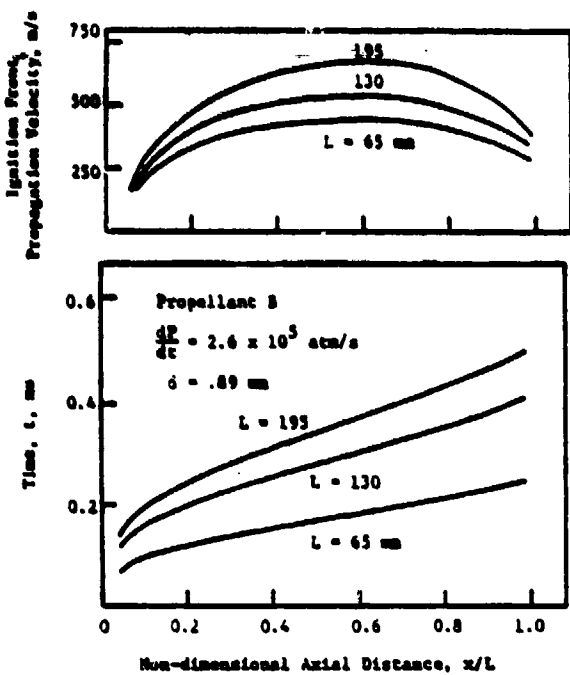


Fig. 14 Effect of crack length on measured ignition front propagation.

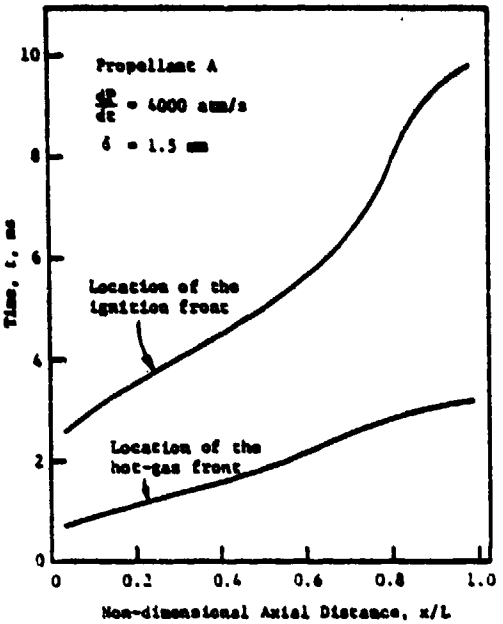


Fig. 15 Time history plot of hot-gas front location and ignition front location.

shows a typical time history plot of the hot gas front location and the ignition front. The pressurization rate for this case was 4000 atm/s, and the crack gap was 1.5 mm. A low pressurization rate was used in this test in order to detect the hot gas front clearly. It was observed that 1) the hot gases precede the ignition front along the crack and reach the tip much earlier than the convective ignition front; 2) the hot gases near the crack tip are luminous for a short period of time, with luminosity disappearing later (this can be attributed to the quenching of the hot gases); and 3) the flame front is nonuniform near the crack entrance, but becomes quite uniform as it propagates along the crack. The nonuniformity of the flame front near the crack entrance region can be attributed to the nonuniform flow at the entrance of a rectangular cross-sectional crack cavity.

Summary and Conclusions

The development of convective burning in an isolated crack has been studied experimentally under a wide range of operating conditions and propellant geometries. Four types of AP-based composite solid propellant were studied. A solid propellant igniter system was developed to closely simulate actual rocket conditions. A high-speed motion picture camera was used to measure the flame propagation rate. Several important observations and conclusions from this study are summarized as follows.

1) The initial pressure distribution in the crack is controlled by the chamber pressurization rate; however, the maximum pressure in the crack cavity is controlled by the initial crack geometry and the ignition and combustion processes in the crack.

2) The hot gases precede and reach the crack tip sooner than the ignition front. The ignition-front propagation speed increases near the crack entrance, reaches a maximum, and then decelerates near the closed end of the crack.

3) As the chamber pressurization rate or burning rate of the propellant is increased, the time required for the ignition front to reach the crack-tip decreases and the maximum flame-front propagation velocity increases.

4) As the gap width of the crack is decreased, the time required for the ignition front to reach the tip increases, but the maximum ignition-front propagation velocity also increases slightly. As the crack length is decreased, both maximum ignition-front propagation velocity and the time required for ignition front to reach the tip decrease.

5) The maximum pressure observed in the crack cavity increases when the gap width is reduced, when the crack length is increased, or when the propellant burning rate is increased.

Acknowledgments

A portion of the results reported in this paper were obtained under the research program sponsored by the Aerothermochemistry Division of the Naval Weapons Center, China Lake, California. The support and advice of Dr. R. L. Derr and Mr. C. F. Price are appreciated. Some of the results reported here were obtained under the project sponsored by the Power Program, Office of Naval Research, Arlington, Virginia, Contract N00014-79-C-0762. The support and advice of Dr. R. S. Miller is acknowledged. The assistance of J. E. Wills and D. Davies of The Pennsylvania State University is also acknowledged.

References

¹Bradley, H. H. Jr. and Boggs, T. L., "Convective Burning in Propellant Defects: A Literature Review," Naval Weapons Center, China Lake, Calif., NWC TP 6007, Feb. 1978.

²Belyaev, A. F., Bobolev, V. K., Korotkov, A. I., Sulimov, A. A., and Chuiko, S. V., *Transition from Deflagration to Detonation in Condensed Phases*, translated from Russian by Israel Program of Scientific Translations, Jerusalem, 1973.

³Kuo, K. K., Chen, A. T., and Davis, T. R., "Convective Burning in Solid-Propellant Cracks," *AIAA Journal*, Vol. 16, June 1978, pp. 600-607.

⁴Kumar, M. and Kuo, K. K., "Ignition of Solid Propellant Crack Tip Under Rapid Pressurization," *AIAA Journal*, Vol. 18, July 1980, pp. 825-833.

⁵Kuo, K. K., Kumar, M., Kovacic, S. M., Wills, J. E., and Chang, T. Y., "Combustion Processes in Solid Propellant Cracks," Annual Report (from The Pennsylvania State University) to the Naval Weapons Center, China Lake, Calif., 1979.

⁶Kuo, K. K., Kovalcin, R. L., and Ackman, S. J., "Convective Burning in Isolated Solid Propellant Cracks," Naval Weapons Center, China Lake, Calif., NWC TP 6049, Feb. 1979.

⁷Kuo, K. K., McClure, D. R., Chen, A. T., and Lucas, F. G., "Transient Combustion in Solid Propellant Cracks," Naval Weapons Center, China Lake, Calif., NWC TP 5943, Oct. 1977.

⁸Prentice, J. L., "Flashdown in Solid Propellants," U. S. Naval Ordnance Test Station, China Lake, Calif., NAVWEPS Rept. 7964, NOTS TP 3009, Dec. 1961.

⁹Prentice, J. L., "Combustion in Solid Propellant Grain Defects: A Study of Burning in Single- and Multi-Pore Charges," Naval Weapons Center, China Lake, Calif., NWC TM 3182, June 1977.

¹⁰Margolin, A. D. and Margulis, V. M., "Penetration of Combustion into an Isolated Pore in an Explosive," *Combustion, Explosion, and Shock Waves*, Vol. 5, No. 1, 1969, pp. 15-16.

¹¹Godai, T., "Flame Propagation into the Crack of Solid Propellant Grain," *AIAA Journal*, Vol. 8, July 1970, pp. 1322-1326.

¹²Bobolev, V. K., Margolin, A. D., and Chuiko, S. V., "The Mechanism by which Combustion Products Penetrate into the Pores of a Charge of Explosive Material," *DokLadY Akademii Nauk USSR*, Vol. 162, May 1965, pp. 388-391.

¹³Payne, C. E., "Flame Propagation in Propellant Cracks," Air Force Rocket Propulsion Laboratory, AFRPL-TR-69-66, 1969.

¹⁴Krasnov, Y. K., Margulis, V. M., Margolin, A. D., and Pokhil, P. F., "Rate of Penetration of Combustion into the Pores of an Explosive Charge," *Combustion, Explosion, and Shock Waves*, Vol. 6, No. 3, 1970, pp. 262-265.

¹⁵Belyaev, A. F., Korotkov, A. I., Sulimov, A. A., Sukyan, M. K., and Obmenin, A. V., "Development of Combustion in an Isolated Pore," *Combustion, Explosion, and Shock Waves*, Vol. 5, Jan.-March 1969, pp. 4-9.

¹⁶Belyaev, A. F., Bobolev, V. K., Korotkov, A. I., Sulimov, A. A., and Chuiko, S. V., "Development of Burning in a Single Pore," *Transition of Combustion of Condensed Systems to Detonation*, Chap. 3, Pt. A, Sec. 22, Science Publisher, 1973, pp. 115-134.

¹⁷Kumar, M., "A Study of Flame Spreading and Combustion Processes in Solid Propellant Cracks," Ph.D. Thesis, The Pennsylvania State University, Aug. 1980.

¹⁸Taylor, J. W., "The Burning of Secondary Explosive Powers by a Convective Mechanism," *Transactions of the Faraday Society*, Vol. 58, 1962, pp. 561-568.

APPENDIX E
(Ref. No. 7)

A COMPREHENSIVE IGNITION MODEL FOR COMPOSITE SOLID PROPELLANTS*

A. K. Kulkarni,[†] M. Kumar,[†] and K. K. Kuo[§]
Department of Mechanical Engineering
The Pennsylvania State University
University Park, PA 16802

May 25, 1981

(Abstract submitted for presentation at the Eighteenth JANNAF
Combustion Meeting, Pasadena, Ca., Oct. 19-23, 1981.)

*This research represents a part of results obtained under Contract No. N00014-79-C-0762, sponsored by the Power Program, Office of Naval Research, Arlington, Va., under the management of Dr. R. S. Miller.

[†]Assistant Professor

[§]Associate Professor

Abstract

Ignition of a solid propellant is a complex physico-chemical phenomenon which involves interaction between various processes such as heat transfer, fluid mechanics, phase change, mass diffusion of chemical species, chemical kinetics, etc. The theoretical modeling of the ignition process is further complicated by such factors as the heterogeneous nature of the propellant (and the overall ignition process), intricate chemical kinetics, determination of the controlling mechanism of the ignition process, and selection of appropriate ignition criterion. A review of the solid propellant ignition was recently conducted by the authors.¹ It was noted that the ignition process under rapidly increasing pressure conditions which is typical of ignition transients in rocket motors and the development of deflagration-to-detonation transition (DDT) process in fractured propellant grains, has not been adequately studied in the past. Furthermore, most ignition models employ a number of simplifying assumptions which may not be valid under actual operating conditions. Nor, has the influence of chemical kinetics on ignition processes been treated in detail to date. All of the previous models, except that of Kumar and Hermance,² have considered the composite propellant to be one-dimensional. Most models make an a priori assumption about the site of ignition, i.e., in the solid-phase, gas-phase, or at the interface. It is apparent that in order to fully understand the ignition process and to accurately predict the ignition delay time, a comprehensive theoretical model is needed. The objective of this study is to develop a generalized ignition model. Specific features of the proposed model are:

1. Two-dimensional (axisymmetric) geometry, allowing a more complete description of the heterogeneous propellant ignition.
2. Inclusion of a pressurization (dP/dt) term in the governing equation for the gases surrounding the propellant in order to simulate actual rocket motor ignition conditions.
3. No a priori assumption of a solid-phase, heterogeneous, or gas-phase reaction mechanism to specify the ignition site. (The current model allows chemical reactions in all regions, including the gas phase, interfaces, and subsurface.)
4. Consideration of detailed chemical kinetics information in the formulation of the model.

The physical model considers an oxidizer particle embedded in a fuel binder matrix; the sizes of the particle and the surrounding binder are determined statistically from the oxidizer particle-size distribution and the fuel/oxidant ratio of the propellant. The shape of the oxidizer particle is approximated by a cylindrical pellet. The mathematical model consists of governing equations for the solid-phase and gas-phase regions. In the solid phase, two energy equations are considered; one for the oxidizer and the other for the fuel. Source terms in these equations include contributions due to indepth radiation absorption, photochemical heat release, and heat absorption due to pyrolysis. The equations are coupled to the gas-phase conservation equations through the heat flux balance at the solid-gas interface. Gas-phase behavior is described by mass, energy, and species conservation equations. The measured pressure-time traces near the propellant sample surface is considered to be an input to the model. For AP-based propellants, five different species (NH_3 , HClO_4 , gaseous fuel, gaseous oxidizer, and products) are considered to be present in the gas phase. Five

chemical reactions are considered for this family of propellants, viz., exothermic degradation of solid AP particle into oxidizer gases, dissociative sublimation of AP into NH₃ and HClO₄, reaction between premixed NH₃ and HClO₄, fuel pyrolysis, and diffusion flame resulting from chemical reaction between oxidizer and fuel gases to form products. The required initial and boundary conditions for the governing equations are specified in detail in the paper.

The proposed model could serve as a framework for the formulation of ignition models for a wide range of conditions and propellants, since portions of this model can be easily simplified and/or replaced for specific applications. It can also aid in the identification of the necessary empirical input required for a given propellant. Numerical solution of this model is in progress; results will be presented at a later date.

References

1. Kulkarni, A. K., Kumar, M., and Kuo, K. K., "Review of Solid Propellant Ignition Studies," AIAA Paper 80-1210, presented at the AIAA/SAB/ASME 16th Joint Propulsion Conference, Hartford, Connecticut, July 1980.
2. Kumar, R. K. and Hermance, C. E., "Gas Phase Ignition Theory of a Heterogeneous Solid Propellant," Combustion Science and Technology, Vol. 4, 1972, pp. 191-196.

APPENDIX F
(Ref. No. 8)

INVESTIGATION OF COMPOSITE PROPELLANT
IGNITION UNDER RAPID PRESSURIZATION*

J. S. Wills,¹ M. Kumar,² A. K. Kulkarni,²
M. Hand,³ and K. K. Kuo⁴

Department of Mechanical Engineering
The Pennsylvania State University
University Park, PA 16802

May 25, 1981

(Abstract submitted for presentation at the Eighteenth JANNF
Combustion Meeting, Pasadena, California, Oct. 19-23, 1981)

*This paper represents a part of the work conducted under Contract No. N00014-79-C-0762 sponsored by the Power Program, Office of Naval Research, Arlington, Virginia, under the management of Dr. R. S. Miller.

¹Graduate Student

²Assistant Professor

³Visiting Research Associate from Fraunhofer Institut fur Treib-und Explosivstoffe, Federal Republic of Germany

⁴Associate Professor

ABSTRACT

Investigation of solid propellant ignition under rapid pressurization is essential to understand fundamentals of ignition mechanism and deflagration-to-detonation transition (DDT) processes. In some of our previous research conducted at The Pennsylvania State University, it was observed that the tip region of a solid propellant crack can be ignited by compression waves generated by rapid chamber pressurization. It was also observed that a propellant sample placed at the tip of an inert crack can be ignited in the same manner. The measured ignition delay under these conditions is in the order of 1 ms or less. This short ignition delay time implies a high rate of energy deposition onto the propellant. The mechanism involved could be used either for interpreting the evolution of DDT in fractured propellant grains or for developing future efficient igniter systems.

The present investigation deals with both experimental and theoretical studies of solid propellant ignition under rapid pressure loading. Specific objectives of this study are:

1. To observe the detailed ignition phenomenon and to measure the ignition delay time and instantaneous heat flux to the propellant sample surface;
2. To study the effect of pressurization rate (dP/dt), igniter gas temperature (T_f), and propellant type on ignition delay; and
3. To predict the ignition delay, using measured values of heat flux to the propellant sample surface and to compare calculated and measured values.

Test firings have been conducted to experimentally determine the ignition delay of solid propellants. The combustion chamber consists of a solid propellant igniter system to generate high-temperature, high-velocity product gases. Product gases flow into the main cavity of the test rig with an exit nozzle at the opposite end. A small sample of propellant is situated at the tip of an inert crack channel, which is perpendicular to the main-flow direction of igniter gases. As a result of chamber pressurization, hot gases penetrate the crack and transfer heat to the propellant sample. The ignition event is observed through a transparent plexiglass window.

The data acquisition system consists of a high-speed (up to 44,000 pictures per second) movie camera and photodiode system to detect ignition, a piezoelectric pressure transducer system to measure pressure-time history, and a thin-film thermocouple located at the crack tip adjacent to the propellant sample to deduce heat flux to the propellant surface. Transient signals are recorded on a multi-channel waveform recorder with a maximum sampling rate of 2 MHz. The digitized output of the waveform recorder is transferred to a minicomputer for data storage and processing.

In the theoretical analysis, the composite propellant is considered to consist of AP oxidizer particles surrounded by the fuel binder. The equivalent particle sizes are determined stochastically. The energy transfer to the propellant is modeled by two coupled transient 2D (axisymmetric) heat conduction equations for a heterogeneous control volume composed of an oxidizer particle and fuel binder. The energy equation includes both surface and subsurface solid-phase reactions, as

well as indepth radiation absorption. The heat flux deduced from temperature measurements is used as a boundary condition for the partial differential equations. The numerical solution is obtained by using an implicit iterative scheme.

Measured ignition delay is found to decrease as pressurization rate increases. Computed heat flux to the propellant surface is in the order of 10^7 W/m^2 ($200 \text{ cal/cm}^2\text{-s}$). Further experiments are in progress to obtain additional data on the influence of other parameters on the ignition process.

DYN

6/81

DISTRIBUTION LIST

<u>No. Copies</u>	<u>No. Copies</u>		
Dr. L.V. Schmidt Assistant Secretary of the Navy (R,E, and S) Room 5E 731 Pentagon Washington, D.C. 20350	1	Dr. F. Roberto Code AFRPL MKPA Edwards AFB, CA 93523	1
Dr. A.L. Slafkosky Scientific Advisor Commandant of the Marine Corps Code RD-1 Washington, D.C. 20380	1	Dr. L.H. Caveny Air Force Office of Scientific Research Directorate of Aerospace Sciences Bolling Air Force Base Washington, D.C. 20332	1
Dr. Richard S. Miller Office of Naval Research Code 413 Arlington, VA 22217	10	Mr. Donald L. Ball Air Force Office of Scientific Research Directorate of Chemical Sciences Bolling Air Force Base Washington, D.C. 20332	1
Mr. David Siegel Office of Naval Research Code 260 Arlington, VA 22217	1	Dr. John S. Wilkes, Jr. FJSRL/NC USAF Academy, CO 80840	1
Dr. R.J. Marcus Office of Naval Research Western Office 1030 East Green Street Pasadena, CA 91106	1	Dr. R.L. Lou Aerojet Strategic Propulsion Co. P.O. Box 15699C Sacramento, CA 95813	1
Dr. Larry Peebles Office of Naval Research East Central Regional Office 666 Summer Street, Bldg. 114-D Boston, MA 02210	1	Dr. V.J. Keenan Anal-Syn Lab Inc. P.O. Box 547 Paoli, PA 19301	1
Dr. Phillip A. Miller Office of Naval Research San Francisco Area Office One Hallidie Plaza, Suite 601 San Francisco, CA 94102	1	Dr. Philip Howe Army Ballistic Research Labs ARRADCOM Code DRDAR-BLT Aberdeen Proving Ground, MD 21005	1
Mr. Otto K. Heiney AFATL - DLDL Elgin AFB, FL 32542	1	Mr. L.A. Watermeier Army Ballistic Research Labs ARRADCOM Code DRDAR-BLI Aberdeen Proving Ground, MD 21005	1
Mr. R. Geisler ATTN: MKP/MS24 AFRPL Edwards AFB, CA 93523	1	Dr. W.W. Wharton Attn: DRSMI-RKL Commander U.S. Army Missile Command Redstone Arsenal, AL 35698	1

DYN

6/81

DISTRIBUTION LIST

	<u>No. Copies</u>		<u>No. Copies</u>
Dr. R.G. Rhoades Commander Army Missile Command DRSMI-R Redstone Arsenal, AL 35898	1	Dr. E.H. Debutts Hercules Inc. Baccus Works P.O. Box 98 Magna, UT 84044	1
Dr. W.D. Stephens Atlantic Research Corp. Pine Ridge Plant 7511 Wellington Rd. Gainesville VA 22065	1	Dr. James H. Thacher Hercules Inc. Magna Baccus Works P.O. Box 98 Magna, UT 84044	1
Dr. A.W. Barrows Ballistic Research Laboratory USA ARRAADCOM DRDAR-BLP Aberdeen Proving Ground, MD 21005	1	Mr. Theodore M. Gilliland Johns Hopkins University APL Chemical Propulsion Info. Agency Johns Hopkins Road Laurel, MD 20810	1
Dr. C.M. Frey Chemical Systems Division P.O. Box 358 Sunnyvale, CA 94086	1	Dr. R. McGuire Lawrence Livermore Laboratory University of California Code L-324 Livermore, CA 94550	1
Professor F. Rodriguez Cornell University School of Chemical Engineering Olin Hall, Ithaca, N.Y. 14853	1	Dr. Jack Linsk Lockheed Missiles & Space Co. P.O. Box 504 Code Org. 83-10, Bldg. 154 Sunnyvale, CA 94088	1
Defense Technical Information Center DTIC-DDA-2 Cameron Station Alexandria, VA 22314	12	Dr. B.G. Craig Los Alamos National Lab P.O. Box 1663 NSP/DOD, MS-245 Los Alamos, NM 87545	1
Dr. Rocco C. Musso Hercules Aerospace Division Hercules Incorporated Alleghany Ballistic Lab P.O. Box 210 Washington, D.C. 21502	1	Dr. R.L. Rabie WX-2, MS-952 Los Alamos National Lab. P.O. Box 1663 Los Alamos NM 37545	1
Dr. Ronald L. Simmons Hercules Inc. Eglin AFATL/DLDL Eglin AFB, FL 32542	1	Dr. R. Rogers WY-2 Los Alamos Scientific Lab. P.O. Box 1663 Los Alamos, NM 87545	1

DYN

6/81

DISTRIBUTION LIST

<u>No. Copies</u>		<u>No. Copies</u>	
	Mr. R. Brown Naval Air Systems Command Code 330 Washington, D.C. 20361	1	Mr. J. Schnur Naval Research Lab. Code 6910 Washington, D.C. 20375
	Dr. H. Rosenwasser Naval Air Systems Command AJR-310C Washington, D.C. 20360	1	Mr. R. Beauregard Naval Sea Systems Command SEA 64E Washington, D.C. 20362
	Mr. B. Sobers Naval Air Systems Command Code 03P25 Washington, D.C. 20360	1	Mr. G. Edwards Naval Sea Systems Command Code 62R3 Washington, D.C. 20362
	Dr. L.R. Rothstein Assistant Director Naval Explosives Dev. Engineering Dept. Naval Weapons Station Yorktown, VA 23691	1	Mr. John Boyle Materials Branch Naval Ship Engineering Center Philadelphia, PA 19112
	Dr. Lionel Dickinson Naval Explosive Ordnance Disposal Tech. Center Code O Indian Head, MD 20640	1	Dr. H.G. Adolph Naval Surface Weapons Center Code R11 White Oak Silver Spring, MD 20910
	Mr. C.L. Adams Naval Ordnance Station Code PM4 Indian Head, MD 20640	1	Dr. T.D. Austin Naval Surface Weapons Center Code R16 Indian Head, MD 20640
	Mr. S. Mitchell Naval Ordnance Station Code 5253 Indian Head, MD 20640	1	Dr. T. Hall Code R-11 Naval Surface Weapons Center White Oak Laboratory Silver Spring, MD 20910
	Dr. William Tolles Dean of Research Naval Postgraduate School Monterey, CA 93940	1	Mr. G.L. Mackenzie Naval Surface Weapons Center Code R101 Indian Head, MD 20640
	Naval Research Lab. Code 6100 Washington, D.C. 20375	1	Dr. K.F. Mueller Naval Surface Weapons Center Code R11 White Oak Silver Spring, MD 20910

DYN

6/81

DISTRIBUTION LIST

<u>No. Copies</u>	<u>No. Copies</u>		
Mr. J. Murrin Naval Sea Systems Command Code 62R2 Washington, D.C. 20362	1	Dr. A. Nielsen Naval Weapons Center Code 385 China Lake, CA 93555	1
Dr. D.J. Pastine Naval Surface Weapons Center Code R04 White Oak Silver Spring, MD 20910	1	Dr. R. Reed, Jr. Naval Weapons Center Code 388 China Lake, CA 93555	1
Mr. L. Roslund Naval Surface Weapons Center Code R122 White Oak, Silver Spring MD 20910	1	Dr. L. Smith Naval Weapons Center Code 3205 China Lake, CA 93555	1
Mr. M. Stosz Naval Surface Weapons Center Code R121 White Oak Silver Spring, MD 20910	1	Dr. B. Douda Naval Weapons Support Center Code 5242 Crane, Indiana 47522	1
Dr. E. Zimmet Naval Surface Weapons Center Code R13 White Oak Silver Spring, MD 20910	1	Dr. A. Faulstich Chief of Naval Technology MAT Code 0716 Washington, D.C. 20360	1
Dr. D. R. Derr Naval Weapons Center Code 388 China Lake, CA 93555	1	LCDR J. Walker Chief of Naval Material Office of Naval Technology MAT, Code 0712 Washington, D.C. 20360	1
Mr. Lee N. Gilbert Naval Weapons Center Code 3205 China Lake, CA 93555	1	Mr. Joe McCartney Naval Ocean Systems Center San Diego, CA 92152	1
Dr. E. Martin Naval Weapons Center Code 3858 China Lake, CA 93555	1	Dr. S. Yamamoto Marine Sciences Division Naval Ocean Systems Center San Diego, CA 91232	1
Mr. R. McCarten Naval Weapons Center Code 3272 China Lake, CA 93555	1	Dr. G. Bosmajian Applied Chemistry Division Naval Ship Research & Development Center Annapolis, MD 21401	1
		Dr. H. Shuey Rohn and Haas Company Huntsville, Alabama 35801	1

CYN

5/81

DISTRIBUTION LIST

No. Copies	No. Copies
Dr. J.F. Kincaid Strategic Systems Project Office Department of the Navy Room 901 Washington, D.C. 20376	1
Strategic Systems Project Office Propulsion Unit Code SU2701 Department of the Navy Washington, D.C. 20376	1
Mr. E.L. Throckmorton Strategic Systems Project Office Department of the Navy Room 10-3 Washington, D.C. 20376	1
Dr. P.A. Flanagan Thiokol Huntsville Division Huntsville, Alabama 35807	1
Mr. G.F. Mangum Thiokol Corporation Huntsville Division Huntsville, Alabama 35807	1
Mr. E.S. Sutton Thiokol Corporation Elkton Division P.O. Box 241 Elkton, MD 21921	1
Dr. G. Thompson Thiokol Wasatch Division MS 240 P.O. Box 524 Brigham City, UT 84302	1
Dr. T.F. Davidson Technical Director Thiokol Corporation Government Systems Group P.O. Box 4262 Edgemont, Utah 84409	1
Dr. C.W. Vriesen Thiokol Elkton Division P.O. Box 241 Elkton, MD 21921	1
Dr. J.C. Hinshaw Thiokol Wasatch Division P.O. Box 524 Brigham City, Utah 84302	1
U.S. Army Research Office Chemical & Biological Sciences Division P.O. Box 12211 Research Triangle Park NC 27709	1
Dr. R.F. Walker USA ARADCOM DRDAR-LCC Dover, NJ 07801	1
Dr. T. Sinden Munitions Directorate Propellants and Explosives Defense Equipment Staff British Embassy 3100 Massachusetts Ave. Washington, D.C. 20008	1
LTC B. Loving AFROL/LK Edwards AFB, CA 93523	1
Professor Alan N. Gent Institute of Polymer Science University of Akron Akron, OH 44325	1
Mr. J. M. Franklin Army Ballistic Research Labs ARRADCOM Code DRDAR-BLI Aberdeen Proving Ground, MD 21005	1

DYN

6/81

DISTRIBUTION LIST

<u>No. Copies</u>		<u>No. Copies</u>
	Dr. Ingo W. May Army Ballistic Research Labs ARRADCOM Code DRDAR-BLI Aberdeen Proving Ground, MD 21005	1
	Professor N.W. Tschoegl California Institute of Tech Dept. of Chemical Engineering Pasadena, CA 91125	1
	Professor M.D. Nicol University of California Dept. of Chemistry 405 Hilgard Avenue Los Angeles, CA 90024	1
	Professor A. G. Evans University of California Berkeley, CA 94720	1
	Professor T. Litovitz Catholic Univ. of America Physics Department 520 Michigan Ave., N.E. Washington, D.C. 20017	1
	Professor W. G. Knauss Graduate Aeronautical Lab California Institute of Tech. Pasadena, CA 91125	1
	Professor Edward Price Georgia Institute of Tech. School of Aerospace Engin. Atlanta, Georgia 30332	1
	Dr. Kenneth O. Hartman Hercules Aerospace Division Hercules Incorporated P.O. Box 210 Cumberland, MD 21502	1
	Dr. Thor L. Smith IBM Research Lab D42.282 San Jose, CA 95193	1
	Dr. J. P. Marshall Dept. 52-35, Bldg. 204/2 Lockheed Missile & Space Co. 3251 Hanover Street Palo Alto, CA 94304	1
	Ms. Joan L. Janney Los Alamos National Lab Mail Stop 920 Los Alamos, NM 87545	1
	Dr. J. M. Walsh Los Alamos Scientific Lab Los Alamos, NM 87545	1
	Professor R. W. Armstrong Univ. of Maryland Department of Mechanical Eng. College Park, MD 20742	1
	Prof. Richard A. Reinhardt Naval Postgraduate School Physics & Chemistry Dept. Monterey, CA 93940	1
	Dr. R. Bernecker Naval Surface Weapons Center Code R13 White Oak, Silver Spring, MD 20910	1
	Dr. M. J. Kamlet Naval Surface Weapons Center Code R11 White Oak, Silver Spring, MD 20910	1
	Professor J. D. Achenbach Northwestern University Dept. of Civil Engineering Evanston, IL 60201	1
	Dr. N. L. Basdekas Office of Naval Research Mechanics Program, Code 432 Arlington, VA 22217	1
	Professor Kenneth Kuo Pennsylvania State Univ. Dept. of Mechanical Engineering University Park, PA 16802	1

DYN

6/81

DISTRIBUTION LIST

	<u>No. Copies</u>	<u>No. Cooies</u>
Dr. S. Sheffield Sandia Laboratories Division 2513 P.O. Box 5800 Albuquerque, NM 87185	1	
Dr. M. Farber Space Sciences, Inc. 135 Maple Avenue Monrovia, CA 91016	1	
Dr. Y. M. Gupta SRI International 333 Ravenswood AVenue Menlo Park, CA 94025	1	
Mr. M. Hill SRI International 333 Ravenswood Avenue Menlo Park, CA 94025	1	
Professor Richard A. Schapery Texas A&M Univ. Dept of Civil Engineering College Station, TX 77843	1	
Dr. Stephen Swanson Univ. of Utah Dept. of Mech. & Industrial Engineering MEB 3008 Salt Lake City, UT 84112	1	
Mr. J. D. Byrd Thiokol Corp. Huntsville Huntsville Div. Huntsville, AL 35807	1	
Professor G. D. Duvall Washington State University Dept. of Physics Pullman, WA 99163	1	
Prof. T. Dickinson Washington State University Dept. of Physics Pullman, WA 99163	1	